Physik-Department

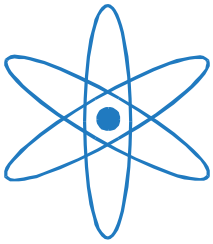

Dose delivery and treatment planning methods for efficient radiation therapy with laser-driven particle beams

Dissertation
von

Stefan Schell

Technische Universität
München

TECHNISCHE UNIVERSITÄT MÜNCHEN
Advanced Technologies in Radiation Therapy

Dose delivery and treatment planning methods for efficient radiation therapy with laser-driven particle beams

Stefan Schell

Vollständiger Abdruck der von der Fakultät für Physik der Technischen Universität München zur Erlangung des akademischen Grades eines

Doktors der Naturwissenschaften (Dr. rer. nat.)

genehmigten Dissertation.

Vorsitzender:	Univ.-Prof. Dr. Martin Zacharias
Prüfer der Dissertation:	
	1. Univ.-Prof. Dr. Jan J. Wilkens
	2. Univ.-Prof. Dr. Franz Pfeiffer

Die Dissertation wurde am 20.07.2011 bei der Technischen Universität München eingereicht und durch die Fakultät für Physik am 18.10.2011 angenommen.

Abstract

Purpose: Laser-driven charged particle acceleration is a promising new technology for radiation therapy with protons or heavy ions that potentially enables reduced treatment costs compared to conventional acceleration systems involving synchrotrons or cyclotrons. However, this method produces beams with different properties compared to the conventional beams. Particles accelerated by a laser based machine typically have a broad energy spectrum. Furthermore, the time structure of the beam is different since each laser shot causes the acceleration of a particle bunch, that contains a certain amount of particles and that cannot be split up into smaller units with active separation technologies such as the ones used for spot scanning. Additionally, the number of these bunches is limited by the repetition rate of the laser. Simply recreating the conditions for the former treatment techniques of conventionally accelerated particle therapy is inefficient and creates secondary radiation. Therefore, new methods of beam delivery and treatment planning for radiation therapy with laser accelerated particles that are adapted to the special properties of these particles are presented.
Methods: First, with the help of an adjustable magnetic energy selection system, suitably wide energy spectra can be chosen from the broad incoming spectrum to treat different areas of the tumor with beams of different energy spreads. The term axial clustering denotes the application of broad energy spectra covering an extended tumor region in different depths simultaneously. If the energy selection system is equipped with an additional scattering device to set the number of transmitted particles per energy bin, spread-out Bragg peaks can be created with one laser shot only. Second, for some tumor areas so called lateral clustering is performed by using a scattering foil and a subsequent multi-leaf collimator to spread a broad beam over a greater lateral extent compared to simple spot scanning. Third, various changes are applied to the optimization routine of the treatment planning process to further reduce the necessary amount of treatment spots and laser shots. Fourth, uncertainties in the energy spectrum of the particles are analyzed and methods for their reduction are discussed. All of these techniques are examined with Monte-Carlo simulations or within the framework of an experimental treatment planning system for laser-driven particles.
Results: By developing and applying this three-dimensional CT-based treatment planning system, it is shown both qualitatively and quantitatively that the proposed methods can make the usage of laser accelerated particles for radiation therapy more efficient. For example, axial clustering and the modification of the optimization routine can increase the amount of used particles, that do not have to be blocked in the beam delivery system, by a factor of 14 without decreasing the treatment plan quality. Additionally, the number of required laser shots to deliver the treatment can be decreased by a factor of 12.
Conclusion: The requirements for future laser accelerators for radiation therapy can be reduced by exploiting the vast amount of idle degrees of freedom in particle therapy. When using laser accelerated particles in an advanced way, that is especially designed for these particles, their clinical application becomes more likely.

Contents

1 Introduction

1.1 Context

1.1.1 Radiation therapy

The concept of using ionizing radiation for the treatment of tumors is almost as old as the basic knowledge concerning this kind of radiation itself. While there is hope to find more biologically oriented modalities in the future, radiation therapy will remain one of the most effective treatments for a wide range of tumors for a long time. Ionizing radiation destroys both malignant and healthy tissues mainly by causing damage to the deoxyribonucleic acid (DNA) of irradiated cells (details in [15, 51]). The great advantage of radiation is that it can be precisely focused on the malignant tissue which enables a good sparing of most of the normal tissue and especially the organs at risk in a patient. This is where physics comes into play. Over the last 100 years the accuracy of radiation delivery to the patient has been optimized further and further.

The vast majority of treatments have been performed with x-rays or gamma rays (for the remainder of this thesis this ionizing electromagnetic radiation will simply be referred to as *photons*). This is because they are relatively easy to create and use. Low energy photons (around 100 keV maximal energy in a broad spectrum) can be produced by simple x-ray tubes and higher energy photons (about 10 MeV) can be generated in compact linear accelerators (linacs). Both methods accelerate electrons first and let them impinge on a target where they produce the desired photon radiation by bremsstrahlung and characteristic radiation. Linacs are available from different vendors for reasonable prices (about EUR 1 million) and are used in every modern radiation therapy clinic. However, despite advancements in previous decades, the fundamental physical properties of the interaction of photons with matter do not allow changing of the exponential attenuation of photon beams traversing matter. Therefore, each treatment beam will always contribute a high amount of damage upstream of (in front of) and a smaller amount downstream of (behind) the malignant tissue.

Since the discovery of particles with a non-zero rest mass as another source of ionizing radiation, other treatment modalities have been analyzed. Before coming to the topic

of this thesis, neutrons and electrons have to be mentioned for completeness. Neutrons have for example been used because of their superior biological properties: their effect is not so significantly deteriorated by a lack of oxygen in the tumor as compared to photons [41]. However, they still have an exponentially decaying depth dose curve (the depth dose curve is a plot of dose deposition against the depth in water). Additionally, they are difficult to produce and handle in practice. Electrons are also used in therapy but are limited to irradiations close to the surface since they deliver most of their dose within a few centimeters after impinging on the tissue [20].

1.1.2 Particle therapy

The topic of this thesis is the use of charged particles like protons or other heavier ions (for example carbon ions) for radiation therapy. They have a fundamentally different depth dose curve which shows a sharp so called *Bragg peak* at a certain depth that is determined by the initial energy of the particle [21]. This allows better sparing of the normal tissue surrounding the tumor. Additionally, charged particles can be steered by electromagnetic fields which enables more advanced delivery techniques [62]. These particles are accelerated in cyclotrons or synchrotrons which makes the production much more complicated and expensive than conventional photon treatment. A treatment facility using protons and carbon ions to irradiate patients from all possible directions costs about EUR 100 millions. These costs are so high for various reasons. First, the acceleration machine itself is usually very big (and does not fit into the treatment room itself). The required (kinetic) energies are 70 to 250 MeV for protons and 70 to 450 $\frac{\mathrm{MeV}}{\mathrm{u}}$ for carbon ions. Second, the particles have to be steered from the required direction to the required position in the patient. The apparatus accomplishing this is called gantry and is a very huge high precision construction. For treatments including carbon ions it has a diameter of about 13 m and a weight of about 670 t. Therefore, there are only about 35 centers in operation worldwide that use protons or carbon ions for treating patients (for an up-to-date list see: `ptcog.web.psi.ch/ptcentres.html`).

As a side remark, this thesis is about particle therapy only and therefore does not elaborate on the medical advantages of charged particles compared to photons. From the physical point of view it is obvious that the dose - which is correlated to the damage in the tissue - can be tailored to the actual treatment target more easily with protons [8]. However, the medical advantage is hard to prove and remains under discussion. Additionally, every concept and technique that is presented is applicable to all charged ions, hence this thesis is also not about the medical differences of protons compared to heavier ions like carbons [48]. However, most of the actual calculations and simulations

are performed for protons. The description of radiation is done with the physical dose only and does not incorporate any biological measure like the *relative biological effectiveness* (RBE) which would - at least for heavier ions - be required for clinical dose prescriptions [60].

1.1.3 Laser accelerated particle therapy

As explained in the last paragraph, the use of charged particles for radiation therapy is limited by the high costs. Therefore, a lot of research is being done to find alternatives to the conventional acceleration and delivery of charged particles. This thesis deals with one out of a few approaches, namely laser accelerated particle therapy (for an overview see [55]). Laser plasma acceleration uses a very high intensity pulsed near-infrared laser focused on a thin target foil to create a plasma within this foil. There are different acceleration regimes whose occurrence depends on the laser beam and the target properties. In a first very simplified picture for one of these regimes (*target normal sheath acceleration* TNSA), electrons are accelerated out of the target foil and create a charge separation (between the electrons and the left behind nuclei) causing a strong electric field. Subsequently, some of the nuclei are accelerated by this field in the forward direction and can reach energies in the range of MeV within a distance comparable to the thickness of a few atom layers. There is a description of laser plasma acceleration in section 2.1, however, it is not within the scope of this thesis to describe the details of these processes. For the purpose of this work the differences within the properties of laser accelerated particles compared to conventionally accelerated particles are of great interest. These differences are analyzed in detail in various later sections.

1.1.4 Further new acceleration methods

For completeness, it must be mentioned that laser acceleration is not the only new approach to create alternatives to the expensive and big synchrotrons or cyclotrons. From the technological viewpoint *dielectric wall acceleration* (DWA) is an interesting competitor of laser accelerated particle acceleration [6]. The goal is to create a linear induction based proton accelerator with a length of about 2 m only. This compact size could be possible because various new technologies like high gradient insulators and fast precise circuit switching have been combined. A company called Compact Particle Accelerator Corporation (CPAC, `www.cpac.pro`) develops a treatment machine whose first somewhat limited version is supposed to be available around 2014. The fact that the final product has been delayed a couple of times shows that this method has its problems

as well. However, in theory it should produce precise particle beams which are very well suited for radiation therapy. Other companies try to develop slightly less challenging products which are advancements of the classical acceleration methods. For example Still River Systems (`www.stillriversystems.com`) has already started to produce a treatment machine, where a compact synchro-cyclotron is mounted on the treatment gantry making the whole system a one-room solutions (with a rather big room). It is estimated to cost around EUR 20 million.

These two examples show what the goal of laser accelerated particle therapy has to be. To become a common application it has to have advantages over all other possibilities. The future will show which technology (or technologies) will turn out to be the most efficient (regarding accuracy, reliability and costs).

1.2 Content

1.2.1 Description of current problems of laser accelerated particle therapy and motivation of thesis

With laser acceleration the maximally achieved proton energy so far is about 60 MeV [40]. However, there is hope to increase this energy by further boosting the laser intensity. Therefore, every application for medical radiation treatment with laser accelerated particles has to wait for the lasers to become more powerful so they can cover the energy range that is necessary for particle treatment. Nevertheless, even in the long run there will be differences between laser accelerated particles and those which are produced by conventional machines like synchrotrons.

First, the energy spectrum is much wider compared to the monoenergetic spectrum of conventionally accelerated particles. This is due to the nature of the acceleration process itself. Creating a plasma usually involves heating up the target making the whole process a statistical one with different particle energies. Irradiating particles of a broad energy spectrum onto a water phantom does not produce the usual sharp pristine Bragg peak of monoenergetic beams but a wider dose distribution that shows high dose regions over a larger extent. To compete with other acceleration technologies the beams cannot be used without being modified first. A so called *energy selection system* is necessary to obtain the useful part of the spectrum only. Details of how this can be done are given in subsection 2.2.1. For now only the following is important: The parts of the spectrum which are not used must be blocked by heavy shielding installations. This will eventually decrease the beam efficiency and create secondary radiation. The former could cause an overall treatment delay and the latter could render the technical realization to be too

expensive.

Second, the time structure of the particle beam is different. The laser beam is pulsed, therefore the particle beam is pulsed as well. This is different to cyclotrons which operate continuously. Synchrotrons are pulsed as well, but for the matter of radiation therapy they can be seen as quasi-continuous. The time structure of laser accelerated beams on the other hand has much more influence on the treatment possibilities. The target of the laser acceleration process has to be replaced (or displaced) after each shot which is a time consuming process. For one of the most advanced particle delivery techniques called *intensity modulated particle therapy* (IMPT), a high amount of independent dose spots within the tumor (up to about 100,000) is used to tailor the dose to the target. Each of these spots is irradiated consecutively and independently from all other spots. When doing this with a laser, each spot has to be irradiated with one or more independent laser shots. The treatment usually has to be finished within about 10 min. With a repetition rate of for example 10 Hz this allows only 6000 shots, which means an absolute maximum of 6000 spots even if each spot is only irradiated with one shot. Therefore, conventional delivery methods like IMPT have to be adapted to laser accelerated particles. Additionally, the number of particles per shot is of importance. On the one hand, if it is too low, many shots will have to be applied to one dose spot which will prolong the treatment. On the other hand, a very high number of particles could result in a dose that is too high for one spot. In this case a certain amount of particles has to be removed from the shot. This procedure can be done in a so called *fluence selection system* and is described in subsection 2.2.2. However, this again decreases the efficiency of the treatment. Furthermore, the duration of one shot is very short (sub-ns range) which rises questions about a possibly altered biological effect caused by the high dose rate [46].

Third, the foils used as targets for the laser acceleration consist of materials that usually contain more than one chemical element (deliberately or because of impurities). Since different ions have different radiation properties this requires a so called *particle selection system* (see subsection 2.2.3).

And last but not least, there is a fourth topic that is important when talking about radiation therapy with laser accelerated particles. It is the handling of uncertainties. Every treatment process has to deal with uncertainties that can arise from various areas. For example patient alignment uncertainties (setup errors) always have to be taken into account. The laser acceleration process itself brings up new specific uncertainties (see subsection 2.2.4). One of them is the energy spectrum uncertainty. Is the laser always able to produce the same amount of particles per energy? And if no, how can treatment

planning incorporate this?

1.2.2 Outline

After giving the short introduction into the general topic above, the organization of this thesis can be described in the following way. The main topic is the use of laser accelerated particles in radiation therapy. These particles can be either protons or other heavier ions like carbons. A lot of research is being done to develop the laser and the target to produce high energy particles. At some point in the future these particles will hopefully be available for treatment. However, from the radiation therapy side not much work has been performed on how in detail this treatment could look like. There are a lot of differences to particles accelerated by conventional means. Hence, this thesis is meant to start at the opposite side: It puts the patient into focus that shall receive radiation treatment and analyzes the modifications of the treatment process that have to be done to cope with these differences. Therefore, it can also help to state requirements for a treatment system. The more the treatment process is adapted to the laser properties, the less restricting these requirements could potentially be. Additionally, a prioritization could be deduced regarding which goals are most important before a realistic treatment scenario could be set up. This thesis elaborates on these questions in the following chapters:

- Chapter 1 (*Introduction*, page 1) leads into the topic of this thesis.
- Chapter 2 (*Radiation therapy with laser accelerated particles*, page 9) informs the reader about the background of the topic. It gives details about the laser acceleration process, a greater look at the properties of laser accelerated particles and describes the basic hardware that is necessary to use these particles for therapy. The chapter summarizes the state of the art of ideas about radiation therapy with laser accelerated particles. The methods presented here try to recreate the particles as they are produced by cyclotrons or synchrotrons. As soon as this goal is reached, they can be used in the 'classical' way of particle therapy. Based on this the later chapter 5 with the same name but the additional word 'advanced' presents new and more efficient ways to use laser accelerated particles by adapting the treatment process to the new properties.
- Chapter 3 (*Dose delivery methods for laser accelerated particles*, page 27) elaborates on the hardware that is located between the laser acceleration and the patient. This hardware is called the *dose delivery system*. The chapter will mention the

adaption of established methods to laser accelerated particles as well as new dose delivery methods specifically designed to suit these particles. As opposed to later chapters this one in part presents ideas and concepts instead of detailed calculations. This is because there are still too many unknown parameters concerning the laser acceleration process and the final particle beam.

- Chapter 4 (*Computational considerations for the simulation of radiation therapy with laser accelerated particles*, page 47) is a detailed technical chapter about all calculations used for later parts of this work. It consists of the description of the implementation of a Monte Carlo simulation used in this work, of an experimental treatment planning system developed to analyze laser accelerated particles and the dose calculation and optimization algorithms used therein.

- One of the main chapters is chapter 5 (*'Advanced' radiation therapy with laser accelerated particles*, page 63) which was already mentioned above. Based on all preceding chapters it elaborates on a more efficient way to do radiation therapy with laser accelerated particles[1]. There is one section about modifying the shape of the energy spectrum (section 5.2) and one about using the particle beam efficiently (section 5.3). It is shown that these methods allow to state much wider constraints on the properties of particles produced by laser acceleration. For example, the treatment beam does not necessarily have to be monoenergetic for all tumor parts. This greatly increases the efficiency in the energy selection system.

- Finally, chapter 6 (*Uncertainties in radiation therapy with laser accelerated particles*, page 101) is about uncertainties in laser accelerated particle therapy and how they can be reduced.

- Chapter 7 (*Summary and outlook*, page 115) summarizes and discusses the whole thesis and offers an outlook.

[1] For readers who are interested in a compact version of some of the most essential parts of this thesis there are two papers published by the author that cover the two main sections of this chapter in a more condensed way [44, 45].

2 Radiation therapy with laser accelerated particles

2.1 Generation of laser accelerated particles

The first step is the generation of the laser light itself. Lasers used for the acceleration of particles are tabletop setups, although the tables are still quite large. Many of the components of the system can already be bought commercially, however, putting them together in the right manner remains a challenging task and is far from off-the-shelf. A typical laser used for such a purpose is the updated version of the ATLAS laser at the Max Planck Institute of Quantum Optics in Munich, Germany [2, 17]. It consists of a commercial seeding laser and several multi-pass amplifiers to reach the final beam properties. To obtain the required intensities the beam has to be stretched in space and time before the amplification can take place and consequentially has to be compressed afterwards. The time stretching and compression technique is called *chirped pulse amplification* [52]. An optimized setup of the ATLAS system reaches up to 2.5 J in as little as 45 fs with a repetition rate of 10 Hz. Its light frequency is centered around about 800 nm with a final band width of about 20 nm.

The second step is the acceleration of particles. Figure 2.1 shows the basic idea. First, the laser produces a plasma within the target foil. To enable the acceleration of particles a minimal intensity of about 10^{18} W/cm^2 is necessary. Spot sizes of the laser focus are usually about 1 μm^2. For these intensities, a hot electron sheath is generated at the front and back side of the foil. These electrons create a strong electric field between them and the ions left behind in the foil. This field subsequently accelerates these ions. This regime is known as the *target normal sheath acceleration* (TNSA) regime and shows a thermal (exponentially decaying) particle spectrum. Besides that, there are other regimes which take place simultaneously, one of them is called *radiation pressure acceleration* (RPA). Here the ions are accelerated directly by the laser itself and not by hot electrons. Therefore, the energy spectrum is much closer to a monoenergetic spectrum and the energy conversion efficiency is much higher. It depends on the in-

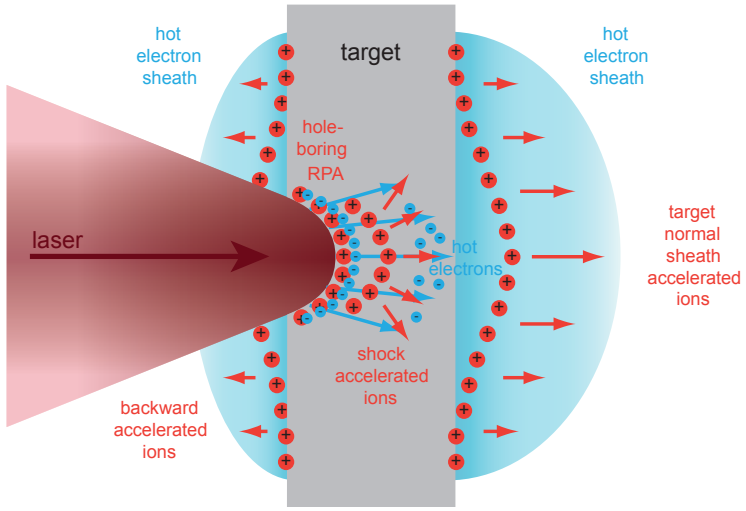

Figure 2.1: The principle of laser plasma acceleration. See text for details. The figure was taken from the PhD thesis of Andreas Henig that deals with laser plasma acceleration [17, figure from page 24].

tensity of the laser and the thickness of the foil which regime is more prevalent in the acceleration process. Early experiments with thick foils (in the range of a few μm) and lower intensities were mainly TNSA dominated. Recent setups on the other hand try to concentrate on the RPA mechanism and use thin foils (down to a few nm). Targets can for example be made out of *diamond-like carbon* (DLC) foils [14]. However, besides carbon and some minor impurities, they will contain a certain amount of hydrogen on their surface as well. This hydrogen either diffuses from the air into the material or can deliberately be added to it. Therefore, the resulting beam is always a mixture of different chemical elements, in this case mainly carbon ions and protons. Additionally, research about different target shapes is performed. Targets which are different from flat foils have the potential to create higher particle energies at the cost of a more complicated target production and alignment process. Furthermore, some groups use gaseous targets which completely eliminates the target alignment problems. Since this thesis does not claim to elaborate on the acceleration process itself more information about the physics of laser acceleration can be found in the literature [61, 26, 32]. Additionally, there are a wide range of papers available about the laser acceleration of particles specifically for radiation therapy [34, 58, 5].

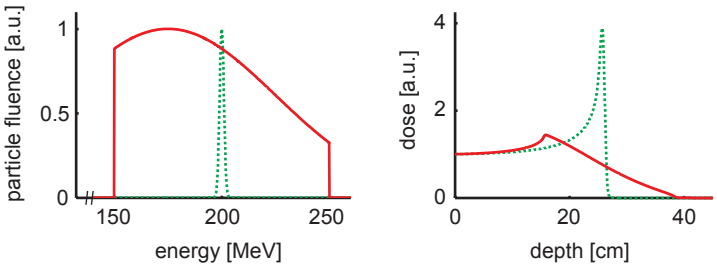

Figure 2.2: Energy spectrum (left) and corresponding depth dose curve (right) of a monoenergetic proton beam from a synchrotron or cyclotron (dashed line) and an exemplary broad energy spectrum of a laser accelerated proton beam (solid line).

2.2 Properties and handling of laser accelerated particles for therapy

As mentioned in the previous chapter laser accelerated particles show different properties compared to particles originating from cyclotrons or synchrotrons. The following subsections give a detailed description of these differences and present solutions to cope with them. Along with this analysis a few basics concepts of particle therapy are mentioned as soon as they become important for the understanding of laser accelerated particle therapy.

2.2.1 Broad energy spectrum and the energy selection system

So far the final energy spectrum of future laser particle accelerators is not fully predictable. The goal is to create a stable and reproducible particle beam with a narrow energy width. However, it is questionable if monoenergetic beams will ever be available. Beams created by the TNSA mechanism have energy spreads from zero to the maximal energy [33] and even the RPA dominated acceleration process still shows a certain range of energies [18]. Regarding radiation therapy this has some implications. Only a monoenergetic beam shows a sharp pristine Bragg peak in the depth dose curve. This sharp peak is the main advantage of charged particles compared to photons which have an exponentially decaying curve. Figure 2.2 shows the energy spectrum (left) and the corresponding depth dose curve (right) of a monoenergetic proton beam from a synchrotron or cyclotron (dashed line) and an exemplary broad energy spectrum of a laser accelerated proton beam (solid line). The monoenergetic beam has a much more localized dose deposition. The depth of its peak can be precisely controlled by the energy

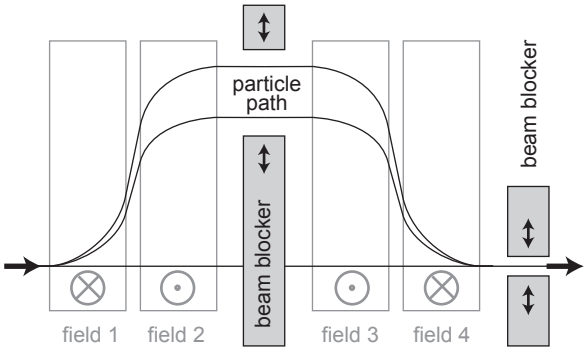

Figure 2.3: The energy selection system consists of four strong magnetic fields and two pairs of beam blocking elements. Charged particles coming from the left hand side are separated in space depending on their energy in the middle of the system. Particles with lower energies are deflected stronger and therefore are further away from the beam axis. High energy particles stay closer to this axis. By adjusting the beam blockers, the required lower and upper energies can be selected. Particles with energies outside of this window of transmitted energies are blocked.

of the beam. For example, the shown 200 MeV produce a Bragg peak at a depth of about 25 cm. For the purpose of this argument, other ions show similar behavior. The broader spectrum consists of protons with various energies which all have their Bragg peak at different depths. Therefore, the high dose region is extended over a certain area. This makes an accurate treatment, sparing the surrounding normal tissue, much harder. Admittedly, compared to photons the depth dose curve is still advantageous. However, to compete with other particle accelerators the energy spectrum can be modified or at least clipped to set limits for the lower and upper beam energy. A machine that can do the clipping is called an *energy selection system*. A system like this that can be used for laser accelerated particle therapy has been proposed by Fourkal et al. (see [11, 12]). Figure 2.3 is a schematic drawing of this system. It consists of four strong magnetic fields of equal absolute values (5 T) but different directions. The required strength can only be achieved with electromagnetic, possibly superconducting, magnets. Additionally, there are two pairs of blocking elements made of a material that is capable of shielding high energy particles (for this purpose for example 10 cm of lead). The length of the magnetic fields in beam direction is 15 cm each, the separation between the first and the second field and between the third and the fourth field is 5 cm each. Particles entering the system from the left hand side are deflected depending on their energy. Particles with low energies are deflected further away from the beam axis and

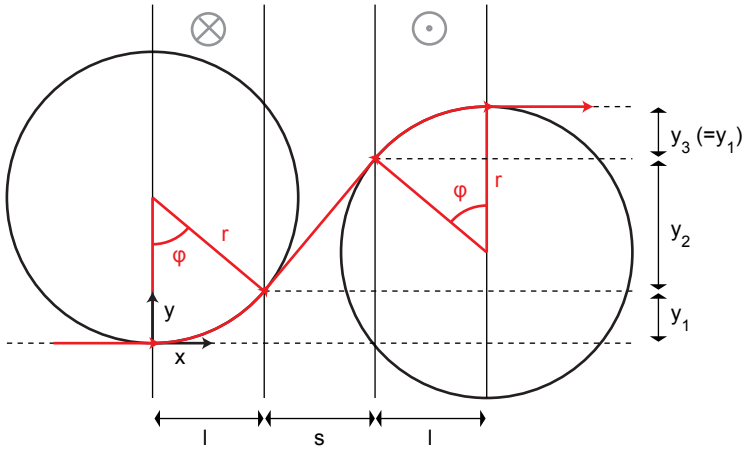

Figure 2.4: Calculation of the deflection in a magnetic energy selection system.

particles with higher energies stay closer to this axis. By adjusting the beam blockers, the required lower and upper energy can be selected. Particles with energies outside of this transmitted window of energies are blocked. Downstream of the blocking element in the middle of the system, the remaining two magnetic fields bring all particles back to the same axis. In theory it is possible to restore monoenergetic beams with this system. However, this comes at the cost of a high amount of secondary radiation generated in the beam blocking elements. Additionally, the number of particles that can actually be used for the irradiation is greatly reduced. To quantify the efficiency of the particle beam behind the energy selection system compared to in front of the system, the number of blocked particles or the amount of blocked energy can be noted. Since particles with different energies show Bragg peaks at different depths (i. e. along the axial direction of the beam) the efficiency of the energy selection system can be called *axial particle efficiency*. In section 5.3 it will be shown that this efficiency can be increased by using wider energy spectra for certain parts of the tumor.

Figure 2.4 illustrates how the deflection in an energy selection system can be calculated. From accelerator physics it is known that the radius r of gyration of a relativistic particle with rest mass m, charge q and momentum p in a magnetic field with magnetic flux density B is $r = \frac{p}{|q|B}$. The cyclotron frequency ω is given by $\omega = \frac{|q|B}{m\gamma}$ with the Lorentz factor γ. Within the first part of the magnetic field (which has the length l) the

following equations for the path of the particle hold true:

$$\begin{aligned} x(t) &= r\sin(\omega t) \\ x(t_1) = l &= r\sin(\omega t_1) \quad \rightarrow \quad t_1 = \frac{1}{\omega}\arcsin\left(\frac{l}{r}\right) \\ y(t) &= r - r\cos(\omega t) \\ y(t_1) = y_1 &= r - r\cos(\omega t_1) = r - r\cos\left(\arcsin\left(\frac{l}{r}\right)\right) \end{aligned}$$

In the drift space of length s in between the two magnetic fields the particle travels along a straight line. With $\varphi = \omega t_1 = \arcsin\left(\frac{l}{r}\right)$ it is:

$$y_2 = s\tan\varphi = s\tan\left(\arcsin\left(\frac{l}{r}\right)\right)$$

With $y_3 = y_1$ it is $y = y_1 + y_2 + y_3 = 2y_1 + y_2$. Therefore, the total deviation y of a charged particle in the energy selection system is given by equation 2.1:

$$y = 2r\left(1 - \cos\left(\arcsin\left(\frac{l}{r}\right)\right)\right) + s\tan\left(\arcsin\left(\frac{l}{r}\right)\right) \tag{2.1}$$

An example is given below. At this point it shall explicitly be noted that in this thesis, when speaking about a certain energy, mostly kinetic energies are meant. However, it should always be clear from the context which energy is needed. For the sake of simplicity, let us temporarily assume the mass of the proton was 1000 $\frac{\text{MeV}}{c^2}$ instead of 938 $\frac{\text{MeV}}{c^2}$. This enables the following easy and memorable set of numbers. In this case a proton with a kinetic energy of $T = 250$ MeV (the maximally required clinical energy) has a total energy of $E = mc^2 + T = 1250$ MeV, a Lorentz factor of $\gamma = \frac{E}{mc^2} = \frac{5}{4}$, a velocity of $\beta = \frac{v}{c} = \sqrt{1-\gamma^{-2}} = \frac{3}{5}$ and a momentum of $p = \gamma m\beta c = 750\ \frac{\text{MeV}}{c}$. This makes simple estimates easy to perform. Coming back to the energy selection system (and the real proton mass), with $B = 5$ T, $l = 15$ cm and $s = 5$ cm the total deviation y for a proton with for example 140 MeV is 9.0 cm and with 182 MeV is 7.7 cm. The dimensions and the field strength of the system have to be chosen similar to the given values to make it both compact and precise. A 1 mm misalignment of the beam blocker for the 140 MeV position results in an energy error of 2.5 MeV.

In the energy selection system, a magnetic field is used to separate charged particles with different energies in space to clip the energy spectrum. It is shown in subsection 3.1.2 that this magnetic property turns out to be a disadvantage for handling beams with broader energy spectra in other parts of the system.

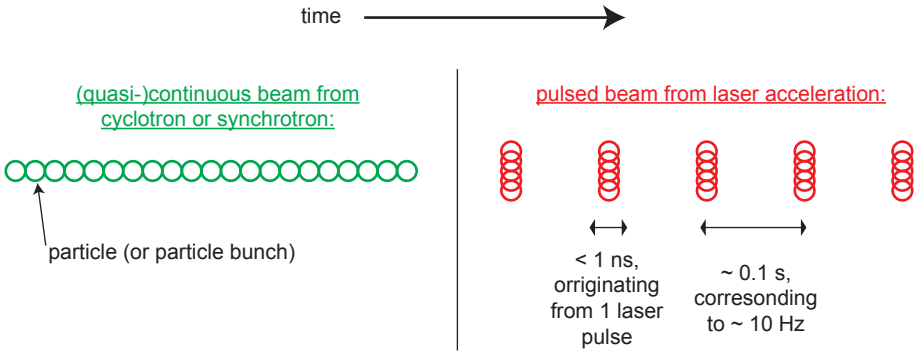

Figure 2.5: Schematic drawing of the time structure of a particle beam from a cyclotron or synchrotron in comparison to a laser accelerated beam. Whereas particles from a conventional acceleration machine arrive at the exit nozzle (quasi-) continuously, the particles of a laser accelerated beam arrive highly pulsed.

2.2.2 Time structure of the beam and the fluence selection system

Figure 2.5 shows the differences in the time structure of a laser accelerated compared to a conventionally accelerated particle beam. As already mentioned above, cyclotrons operate continuously and synchrotrons can - for the purpose of radiation therapy - be seen as quasi-continuous. This is because the time of one complete synchrotron spill is quite long (several s) and the time between individual particle bunches is negligible (in the order of ns). Laser accelerated particle beams show different properties regarding the time structure. The following subsections will elaborate on these differences in more detail.

Repetition rate

Besides the laser repetition rate itself, the most limiting factor for the repetition rate of laser accelerated particle beams is probably the replacement (or displacement) of the acceleration target. At least for thin targets (nm-range) the system can currently only accomplish one shot every few minutes and the mechanical limit is certainly below 1000 Hz. However, it should be mentioned that the approach which uses gaseous targets is only limited by the repetition rate of the laser itself. In this case the repetition rate problem would not be as pronounced as for the case with solid targets. In 'classical' radiation therapy with conventionally accelerated particles the most advanced treatment technique - called intensity modulated particle therapy (IMPT, note: sometimes the *P* stands for *proton* instead of *particle*) - tailors the dose to the tumor by using a three-dimensional dose grid (see figure 2.6). Thereby, the target area is split up into different

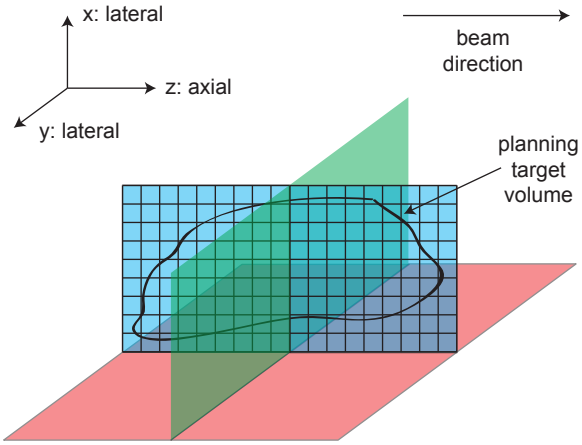

Figure 2.6: Schematic drawing of the dose delivery grid and a *planning target volume* (PTV) for IMPT. The green plane (x-y) pictures one iso-energy layer. For simplicity the grid itself is only shown in the blue plane (x-z), however, it is spread over the whole volume. Each grid point within the PTV is irradiated independently. Note that this drawing assumes a water phantom and a parallel beam geometry.

spots which are irradiated independently. Technically, this is done by creating *layers* spaced in the axial direction (beam direction, also: z-direction) which are irradiated with different beam energies each. In the lateral direction (perpendicular to the beam direction, also: x/y-direction) the beam is scanned magnetically. In modern IMPT a number of up to almost 100,000 independent (thus consecutively irradiated) dose spots in the dose grid is used. The precise number depends on the volume to irradiate and the required accuracy. With a low repetition rate this technique cannot be applied without changes: Because of the clinical (or better: practical) time constraint of about 10 min of active beam time, with low repetition rate laser systems, it is only possible if the number of *shots* per *spot* is close to unity. In this case most of the time most of the particles must be removed from the treatment beam. Therefore, the next subsection is meant to elaborate on the number of particles per shot. However, it is not necessary to use as many as 100,000 independent spots. There are other treatment techniques which use far fewer degrees of freedom (see section 3.2). Later in this thesis new methods will be presented to reduce the number of spots. Moreover, there are methods to reduce the number of shots directly. For now, it shall be noted, that the repetition rate reveals limitations for radiation therapy with laser accelerated particles.

Number of particles per shot and the fluence selection system

As mentioned above, the number of particles per shot is of great importance for radiation therapy with laser accelerated particles. At the moment it is extremely hard to state the fluence per shot of a future laser accelerating system. It depends on the laser itself, the accelerator foil and the beam delivery system. Accelerated particles coming out of the foil show a wide angular spread. A magnetic system to steer them in the right direction has to be developed [16]. However, this is complicated since the particles in one shot might have various energies. Therefore, the further discussion will leave the question of the exact number of particles open. There are three simple possibilities. The first and most unlikely one is that the number of accelerated particles is always exactly the number that is necessary to irradiate a certain spot. The second one is that the number is smaller. This means that more than one shot has to be applied to each spot. If the number of shots per spot becomes bigger, a high total number of shots will be hindered by the repetition rate of the acceleration system. The third possibility is that there are too many particles per shot. Here, without further measures, one spot would receive more than the prescribed dose. The dose rate of a cyclotron or synchrotron is quite low and the beam can be stopped at each requested point in time by blocking it. This allows an irradiation with the required dose. In contrast to this, the dose rate of a laser system within the short time span of one shot is much too high to do this. Therefore, a new system to reduce the number of particles in an already released shot is required. This system is called *fluence selection system*. Every beam stopping system that relies on moving mechanical parts or changing electromagnetic fields is not feasible to accomplish the delivery of for example *half of a shot* because it is simply too slow. However, one possible option is the lateral spreading of the beam with a scattering foil and the subsequent blocking of a certain part of the outer parts of the lateral beam profile. Figure 2.7 shows the fluence selection system that can be used downstream of the energy selection system discussed above. The scattering foil is usually made of lead since this is the (stable) element with the highest scattering to energy-degrading capability. The beam blocker can either be a simple circular collimator or a *multi leaf collimator* (MLC) that can be used to form more complex lateral beam profiles [9]. Independent from the technical realization the fluence selection system reduces the beam efficiency and creates secondary radiation within the collimator. In accordance with the earlier introduced *axial* particle efficiency the efficiency of the fluence selection system can be called *lateral particle efficiency*. It can again be measured in blocked particle numbers or blocked energy. It will be shown later that this efficiency can be increased by grouping neighboring irradiation spots together to distribute the amount of particles

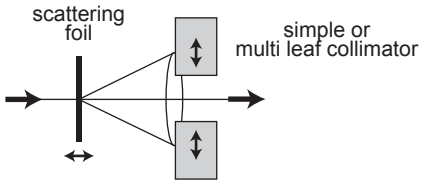

Figure 2.7: Schematic drawing of the fluence selection system. It spreads the beam laterally with a thin foil and subsequently blocks a certain fluence of the outer parts of the lateral beam profile. The blocking element can either be a simple circular collimator or a *multi leaf collimator* (MLC) to shape more complex lateral beam profiles.

over a bigger area.

To calculate the lateral spread of a beam traversing a small distance of a certain material a two-dimensional Gaussian approximation can be made:

$$f\left(\Theta_x, \Theta_y\right)\ \mathrm{d}\Theta_x \mathrm{d}\Theta_y = \frac{1}{2\pi\Theta_0^2}\, e^{-\frac{\Theta_x^2+\Theta_y^2}{2\Theta_0^2}}\ \mathrm{d}\Theta_x \mathrm{d}\Theta_y \tag{2.2}$$

Here, $f\left(\Theta_x, \Theta_y\right)$ is the fraction of particles scattered by the angles Θ_x and Θ_y which describe the scattering in the two lateral dimensions[1]. The value of Θ_0 can be obtained with the following equation [13, 19]:

$$\Theta_0 = \frac{14.1\ \frac{\mathrm{MeV}}{c}\ Z_{inc}}{p\ \beta}\sqrt{\frac{L}{L_R}}\left(1+\frac{1}{9}\log_{10}\left(\frac{L}{L_R}\right)\right)\ \mathrm{rad} \tag{2.3}$$

L is the thickness of the material and L_R its radiation length[2]. Z_{inc} is the charge number of the incident particle, p its momentum and $\beta = \frac{v}{c}$ its velocity. When irradiating a lead foil ($\rho = 11.34\ \frac{\mathrm{g}}{\mathrm{cm}^3}$, $L_R = 6.37\ \frac{\mathrm{g}}{\mathrm{cm}^2}$) of about 1.9 mm thickness with protons of 250 MeV the value of Θ_0 is about 1°. After a drift space of 1 m this produces a Gaussian shaped lateral profile[3] with a σ of about 17 mm. The scattering is energy dependent (p, β), however, this dependency is not as pronounced as compared to using magnets to bend particle tracks. Based on equation 2.3 the scattering behavior is analyzed in more detail

[1] Because of geometrical reasons both Θ_x and Θ_y run from $-\pi$ to π. However, to become unity the integrals over $f\left(\Theta_x, \Theta_y\right)$ have to run from $-\infty$ to ∞. This shows that the distribution is an approximation for small Θ_0.

[2] Both values have to be given in the same units. Since the radiation length usually is given in $\frac{\mathrm{g}}{\mathrm{cm}^2}$ the thickness L has to be converted to this unit as well (by multiplying the actual length with the density of the material).

[3] Saying that because of equation 2.2 the distance of the particles from the beam axis is distributed like a Gaussian is actually only correct when using the small angle approximation.

in subsection 3.1.1.

Duration of a shot

Last not but least, the duration of one shot makes the laser accelerated beam different compared to a beam from a cyclotron or synchrotron. The laser pulse duration can be as little as 45 fs (which are only a few laser light oscillations). Since the accelerated particles have a broad energy spectrum, they also have a broad velocity spectrum. The distance from the acceleration target to the patient is probably at least 2 m, therefore, the duration of the shot is increased by a certain amount. The fastest and the slowest particles in a simultaneously starting bunch of particles with 5% energy spread around 200 MeV will be about 210 ps apart after flying a distance of 2 m. If the particles have a mean energy of 20 MeV only this value is increased to more than 750 ps. However, including this and assuming only a small number of accelerated particles per shot, the peak dose rate is still many orders of magnitude higher than the one from a conventional machine. Hence, research is being done to find out if a biological difference in tissue damage can be found [46]. So far it seems to not matter which of the two dose rates are used and even if it turns out to make a difference, this is most likely to be true for the tumor as well as the healthy tissue. In this case the prescribed doses would have to be modified.

2.2.3 Multiple particle types and the particle selection system

When shielded properly there is no need to worry about the electrons that are accelerated by the laser as well. They bend into the opposite direction in the energy selection system and can be removed by a beam blocker. However, as mentioned before, there is usually a mixture of different chemical elements in the laser accelerated beam. Again, the energy selection system helps, but ions with the same value of $\frac{q}{p}$ are still seen as identical. This is because the radius of gyration is $r = \frac{p}{|q|B}$. The clinically relevant energy range has already been mentioned to be 70 to 250 MeV for protons and 70 to 450 $\frac{\text{MeV}}{\text{u}}$ for carbon ions. A 250 MeV proton is deflected as much as a 820 MeV = 68 $\frac{\text{MeV}}{\text{u}}$ carbon ion. It has to be mentioned that these two particles have completely different penetration depth in matter. The 250 MeV proton is at the very maximum of the clinical range and the 68 $\frac{\text{MeV}}{\text{u}}$ carbon ion is barely powerful enough to be useful.

To determine the impact of the mixing of different chemical elements, the energy-dependent particle fluence produced by the laser accelerator has to be regarded concerning the particle species. The predicted relative energy of protons compared to carbon

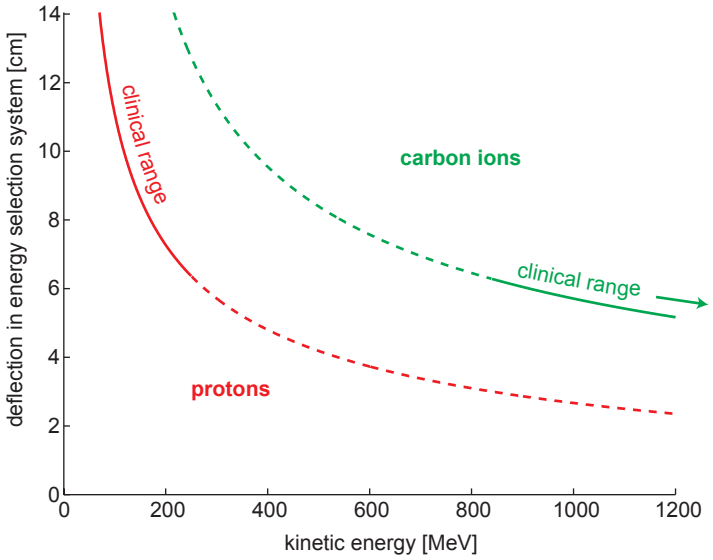

Figure 2.8: Deflection of proton (red) and carbon ion (blue) beams in an energy selection system (dimensions and field strength from subsection 2.2.1). The clinically used energy range is plotted as a solid line, the remaining range is dashed. Each imaginary horizontal line intersects with both the proton and the carbon curve. This means that for each proton energy there is a carbon energy with the same deflection properties in the energy selection system. Note, that the plot does not show the full range of clinically relevant carbon ion energies.

ions depends on the underlying acceleration regime. For TNSA, the static electrical field generated by the hot electron sheath constitutes the same electrical potential for all ion species and therefore predicts $T \sim q$. Thus, the energy *per nucleon* of the carbon ions would be $\frac{6}{12} = \frac{1}{2}$ of the energy of the protons. For RPA, all particles are accelerated to the same velocity [18]. Since $T = (\gamma - 1)mc^2$, the energy *per nucleon* of the carbon ions would be the same than the energy of the protons. Because RPA promises to produce particle beams with a smaller energy width this regime and its predicted particle energies seem to be more realistic for future applications. Therefore, it can be assumed that in beams for proton treatment with a proton energy up to 250 MeV there is a certain amount of carbon ions with energies up to 250 $\frac{\text{MeV}}{\text{u}}$. Conversely, in beams for carbon ion treatment with carbon ion energies up to 450 $\frac{\text{MeV}}{\text{u}}$ there is a certain amount of proton ions with energies up to 450 MeV.

To combine these findings with the particles' magnetic behavior, figure 2.8 shows a plot of the proton and carbon ion deflection in the energy selection system. Assuming a laser system that produces a wide energy spectrum covering the whole clinical range of

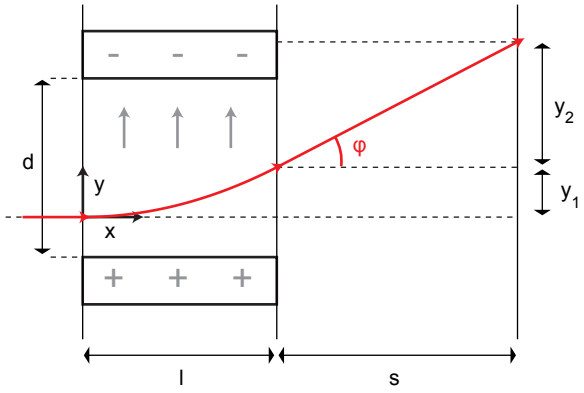

Figure 2.9: Calculation of the deflection in an electric particle selection system.

either protons or carbon ions, the following conclusions are possible: First, for proton treatment, within the whole range of relevant energies, there is a contamination from clinically lower range carbon ions. Second, for carbon ion treatment, for energies up to about 130 $\frac{\text{MeV}}{\text{u}}$ there is a contamination from clinically higher range protons. Carbon ions at this cutoff energy show the same deflection behavior than a 450 MeV proton. For carbon ions with higher energies the protons that are deflected in the same way do not exist in the accelerated spectrum.

To overcome the problem of particle species mixing there needs to be a mechanism that selects the correct particle type before the beam can be used for treatment. Since the magnetic properties of the particles have already been used to select the right energy, an additional characteristic has to be utilized. A possibility is the application of an electric field E' (note: E is the total energy, E' the electrical field) produced by two capacitor plates. For just one particle energy this system can select the right particle type. Therefore, it can be called *particle selection system*. However, since both energy and particle type have to be chosen correctly, only a combination of the simple energy and particle selection systems can be applied. Figure 2.9 is a sketch that illustrates how the deviation in an electrical field can be calculated. First, the velocity v of the particle in x-direction is needed. It stays constant when traversing the electric field and can be used to calculate the time t that the particle spends within the field (in the lab frame). The movement in y-direction is slow and can therefore be described with

classical mechanics.

$$p = \gamma m \beta c, \quad E = \gamma m c^2 \quad \rightarrow \quad v = \beta c = \frac{pc}{E} c$$
$$v = \frac{l}{t} \quad \rightarrow \quad t = \frac{l}{v} = \frac{E}{pc} \frac{l}{c}$$

The next step is to calculate the acceleration a in y-direction. With the electrical voltage U between the capacitor plates at a distance of d and therefore the resulting electrical force F in the gap, the following can be derived.

$$F = qE' = ma, \quad E' = \frac{U}{d} \quad \rightarrow \quad a = \frac{qE'}{m} = \frac{qU}{md}$$

The time within the field t and the acceleration a are plugged into the equations of motion to find the state of the particle at the end of the field. The distance traveled in y-direction y_1 and the velocity in y-direction v_y, both at the end of the field, are of interest.

$$y_1 = \frac{1}{2} a t^2 = \frac{l^2}{2} \frac{qU}{md} \left(\frac{E}{pc} \frac{1}{c} \right)^2$$
$$v_y = at = \frac{qU}{md} \frac{E}{pc} \frac{l}{c}$$

By obtaining the angle φ of the particle when leaving the field, the remaining distance y_2 traveled in y-direction during the drift space of length s can be calculated.

$$\tan \varphi = \frac{v_y}{v} = l \frac{qU}{md} \left(\frac{E}{pc} \frac{1}{c} \right)^2$$
$$y_2 = s \tan \varphi = ls \frac{qU}{md} \left(\frac{E}{pc} \frac{1}{c} \right)^2$$

Therefore, the deviation $y = y_1 + y_2$ of a charged particle in the particle selection system is:

$$y = \left(\frac{l^2}{2} + ls \right) \frac{qU}{md} \left(\frac{E}{pc} \frac{1}{c} \right)^2$$

From this equation it can be seen that particles with the same value of $\frac{q}{m} \left(\frac{E}{pc} \frac{1}{c} \right)^2 = \frac{q}{mv^2}$ are treated in the same way by the field. For classical (non-relativistic) particles this means a selection of $\frac{q}{2T}$. As a reminder: the magnetic field selects by $\frac{q}{p}$. This shows why a combination of magnetic and electric field can choose both energy and particle type.

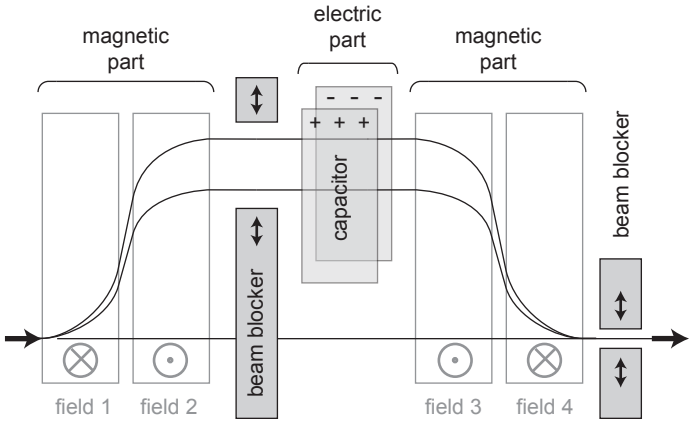

Figure 2.10: Energy and particle selection system. Only a combination of a magnetic field (energy selection system) and an electric field (particle selection system) is able to select the right particle energy and type. The part of the system that is located downstream (on the right hand side) of the capacitor has to be slightly bent into the plane of projection to adjust to the deviation of the required particle by the electric field.

By using $E = mc^2 + T$ and $E^2 = \left(mc^2\right)^2 + (pc)^2$ the final equation reads:

$$y = \left(\frac{l^2}{2} + ls\right) \frac{qU}{mc^2 d} \frac{\left(mc^2 + T\right)^2}{\left(mc^2 + T\right)^2 - \left(mc^2\right)^2} \tag{2.4}$$

According to equation 2.4, a system with the technically already challenging field parameters of $U = 3 \times 10^5$ V and $d = 3$ cm (i. e. $E' = 10\ \frac{\mathrm{MV}}{\mathrm{m}}$) and the further parameters $l = s = 50$ cm shows a deflection of 11 mm for protons with 250 MeV.

Figure 2.10 shows the full system that is able to select particle energy and type. There are various ways to combine the magnetic and electric filters. This is only one possibility. Note, that in this case the part of the system that is located downstream (on the right hand side) of the capacitor has to be slightly bent into the plane of projection to adjust to the deviation of the required particle. Another possibility is to have two electric fields with opposing field directions (the second one for example in front of the first beam blocker). In this case the beam is not bent but shifted into the plane of projection. Yet another modification is to have magnetic and electric fields at the same location. This saves space and does not change the functionality.

2.2.4 New uncertainties

The last difference of laser accelerated particles compared to conventionally accelerated ones that shall be mentioned deals with the topic of uncertainties. In general, uncertainties require attention in high precision radiation therapy. A classical example is the setup uncertainty. The treatment plan of each individual patient is based on an initial *X-ray computed tomography* (CT) image. The treatment itself is usually distributed over multiple (about 30) individual fractions given on successive days (excluding weekends). Therefore, the patient has to be realigned for each of these fractions. Additionally, intra-fraction movements occur which are for example very frequent in lung tumors because of the breathing cycle. Hence, there is always a certain misalignment (of the order of mm) which alters the dose distribution from the planned one. Especially for charged particles with their high precision this has to be taken into account.

Coming back to lasers, there are new uncertainties which have to be considered. Here, the focus is on energy spectrum uncertainties. Experiments carried out so far could not produce a stable particle beam when comparing successive shots. The number of accelerated particles as well as their energy varies considerably from shot to shot. If the goal is to irradiate each tumor spot with just a few shots the system has to become much more stable, otherwise the risk of an overdosage is too high. Certainly, monitoring is required no matter how stable the beam is. It is of advantage that the energy and particle selection system provides an inherent security against completely incorrect energies or particles. It can be argued that even for a monoenergetic acceleration process an energy selection system that does not block the stable beam but possible *accidental* beams is required to provide the necessary security level. With the energy selection system the window of transmitted energies can be set with certainty. For laser accelerated particle accelerators this system is the only active security element in the beam path. Compared to this conventional accelerators consist of many beam elements that cause the beam to be lost when the particles have the wrong properties (e. g. the wrong energy). With the energy selection system, possible uncertainties lay within the window of transmitted energies. The total number of particles as well as their distribution over the energy window has to be monitored *online*. It has to be kept in mind that there is no way to take back the amount of dose delivered by one shot. However, it is highly important to know precisely how many particles with what energies have been delivered by the past shots. Depending on how unstable the beam is this information can used for documentation only (if the uncertainty stays below a threshold) or to alter the future treatment plan (if the uncertainty is outside of an anticipated range). Altering the treatment plan can refer to both an instantaneous change of the current treatment

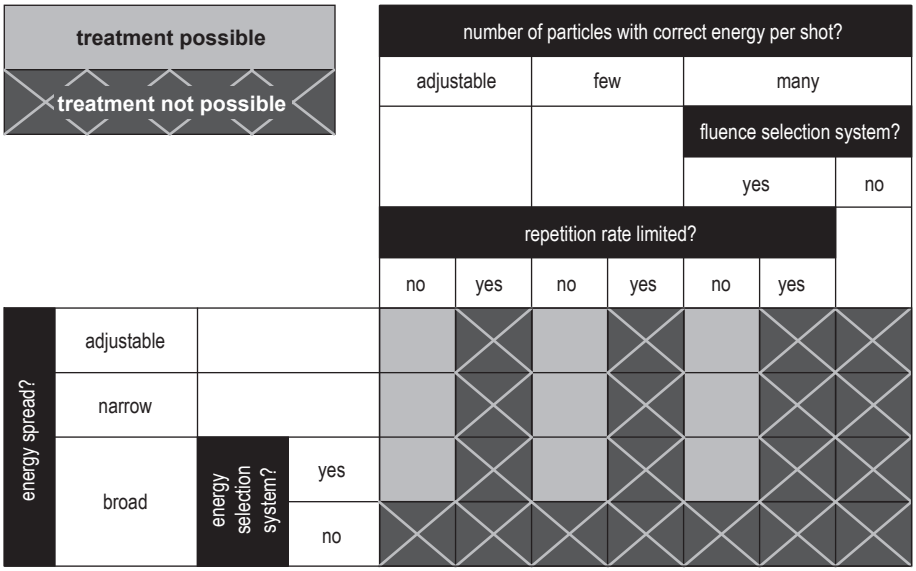

Figure 2.11: Overview of different cases for the properties of a particle beam produced by laser acceleration and their impact on radiation therapy. For simplicity this figure assumes that the particle type is guaranteed.

session (feedback) or a modification of the remaining fractions. The measurement of the number of particles can be done at any point of the beam downstream of the energy selection system. The measurement of the relative energy distribution is only possible if the particles are separated by energy. Therefore, it has to be monitored in the energy selection system. Additional ways to measure the delivered *dose distribution* within the patient (e. g. prompt gamma detection) could be useful tools for radiation therapy with laser accelerated particles. Details about the fluence and energy measurement of the particle beam can be found in section 3.3. Furthermore, in chapter 6 the implications of uncertainties and possible solutions are discussed in detail.

2.3 Limited possibilities with 'classical' methods

The last section showed that there are certain limitations for radiation therapy with laser accelerated particles. Figure 2.11 summarizes the influence of different parameters on the treatment possibilities and demonstrates that some settings might not work for conventional treatment methods such as IMPT. The existence of an energy selection system will be necessary if the laser accelerator cannot produce monoenergetic (or adjustable) energy spectra and the fluence selection system will be necessary if the laser accelerator produces too many particles per shot. In all cases, a low repetition rate can

still prevent the system from being able to deliver high precision particle treatments. The possibilities mentioned so far are referred to as the 'classical' way of performing radiation therapy with laser accelerated particles. Contrary to this, chapter 5 will try to reduce the requirements for a future laser system by adapting the treatment planning and dose delivery process to the properties of laser accelerated particles. For an outlook how things could potentially be different with these 'advanced' treatment methods, have a quick look at figure 5.25 (on page 99). However, before reaching this chapter several basic principles have to be developed and explained in the following chapters.

3 Dose delivery methods for laser accelerated particles

In the previous chapter the *dose delivery* technique called IMPT has been briefly explained. Nowadays it is seen as the most advanced method since it can shape the dose precisely to the tumor outline. However, it is not the only possibility to deliver a treatment. In general, the term *dose delivery* refers to all mechanisms involved in the beam transport and shaping, excluding the particle acceleration itself. This chapter explains the different possibilities and elaborates on their use for laser accelerated particle therapy. Additionally, it introduces new concepts specifically designed for laser accelerated particles and presents the design and usage of a treatment head for these particles.

3.1 Established methods

3.1.1 Passive scattering

Early applications of protons for radiation treatment utilized a simple mechanism called *passive scattering*. The usually narrow beam coming from the accelerator is widened by a scattering system and collimated later to cover the whole lateral tumor extent at once. This can be done with a system similar to the previously mentioned scattering foil or with a more advanced *double scattering system* that uses more than one spreading foil to increase the percentage of the beam that can be used for treatment [42]. Additionally, in the case of the small dose rate of cyclotrons or synchrotrons, the spreading can be done by a magnetic wobbler which distributes the beam with a changing magnetic field and has the advantage that no particle energy is lost and no secondary radiation is generated.

A passive scattering system is usually accompanied by a *range modulator wheel* that is inserted into the beam path. Such a system transforms a monoenergetic beam into a beam with different particle energies. The relative amount of particles with different energies can be chosen in a way that the axial extent of the tumor is irradiated with a flat dose distribution. A beam like this is said to produce a *spread-out Bragg peak* (SOBP). The wheel spins fast and presents the traversing particles different lengths of material to

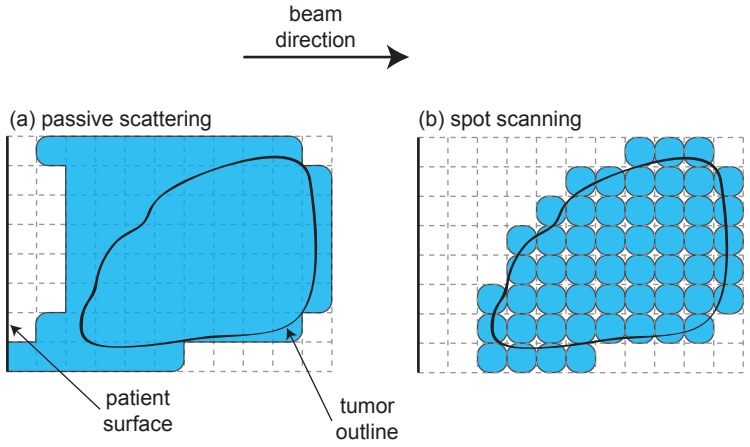

Figure 3.1: Established dose delivery schemes. See section 3.1 for a detailed description. Compare to the blue plane (x-z) in figure 2.6. Each closed blue area is irradiated independently. The figure shows the geometrical dose distribution only. Spot weights are not included. Note that this drawing assumes a parallel incoming beam. If it was coming from a point source the dose delivery grid would have to be adjusted to this geometry. Additionally, this drawing also assumes that a water phantom is irradiated. For real tissues, the grid would have to be adjusted to the radiological depth rather then the geometrical depth.

pass. Therefore, a certain amount of particles looses a certain amount of energy whereas another amount of particles looses another amount of energy. The wheels are usually made of light materials like Lucite to cause maximal energy loss with minimal lateral particle spread. Using the lateral spreading, the range modulator wheel and a patient specific collimation a cylindrical volume with a user-defined base area and a certain depth can be irradiated. By adding an additional so called *compensator* the irradiation volume can be adjusted to the distal edge of the tumor. The compensator presents the beam an additional range shifter depending on the lateral position of the particle. The resulting dose delivery scheme can be seen in part (a) of figure 3.1. There is a detailed review article that describes the use of protons and heavy ions for particle therapy which has an in-depth section dealing with passive scattering [7].

The focus of this subsection is on the lateral spreading of the beam and the dependence on broad energy spectra. Note, that the beam that has to be spread has already passed the energy selection system and is therefore not as wide in energy as the initial beam. However, later chapters will show that it is not necessarily monoenergetic since broader energy spectra can be used as well. To keep things simple a single scattering systems is

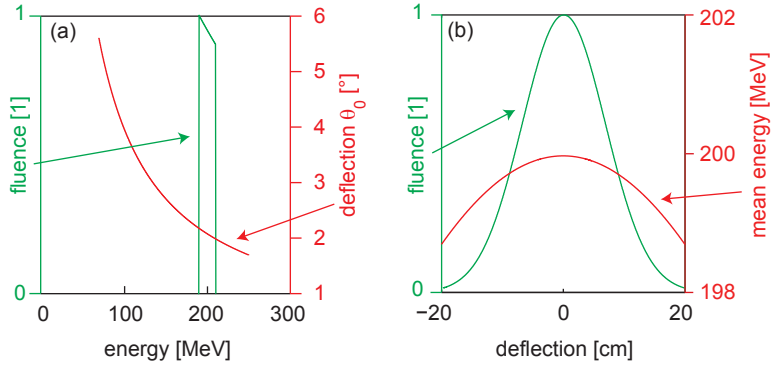

Figure 3.2: Influence of broad energy spectra on passive scattering. A (200 ± 10) MeV proton beam (green curve on the left axis of part (a)) shows a very small location-energy-dependence after traversing 5 mm of lead. The final particle fluence after 2 m of drift space (green curve on the left axis of part (b)) varies much more with location than the mean energy of the beam (red curve on the right axis of part (b)). Note that the energy loss in the scatterer has been neglected for the calculation of the mean energy.

analyzed, however, the findings can easily be extended to double scattering systems. Additionally, only spreading systems with foils are regarded since time dependent magnetic fields to spread the beam are too slow to handle laser accelerated particles.

The fluence selection system mentioned earlier also spreads the beam laterally. In doing so one can select the amount of particles used for irradiation. This is done by blocking superfluous particles in the outer part of the lateral scattering profile. It is obvious that both the fluence selection and the lateral beam shaping for the use of a MLC have to be solved together. The procedure would be the following: First, decide what lateral area should be irradiated, then spread the beam as far as necessary to both cover the whole designated area and reduce the number of particles to the required level. If the number of particles is not too high for the irradiation, the lateral profile will only have to be big enough to cover the irradiation area. However, if the number of particles is too high, the beam will have to be spread further and a greater amount of the outer part will have to be blocked. At this point it has to be mentioned that the lateral beam efficiency includes the *loss* of particles because of both the fluence selection and the lateral shaping of the beam profile within a MLC. This is because the beam can only be spread to a circular profile and the dose falloff at the edge of this profile is not instantaneous. Hence, a certain amount of particles has to be removed.

Equation 2.3 is the basis of the following analysis. Figure 3.2 illustrates the behavior of a proton beam with an energy spectrum ranging from 190 to 210 MeV (green curve on

the left axis of part (a)) after traversing 5 mm of lead. The Gaussian deflection angle Θ_0 (red curve on the right axis of part (a)) is shown for all relevant proton energies from 70 to 250 MeV. After a drift space of 2 m this leads to a certain particle fluence aside from the original beam axis which is a summation of Gaussians with different values for the lateral spread (green curve on the left axis of part (b)). Since all lateral spreads of the incoming energy spectrum are very similar, the result seems to be a Gaussian as well (but is of course not). The interesting point is the energy mixture at different lateral positions (red curve on the right axis of part (b)). The highest mean energy can be found in the center of the beam since high energy particles are deflected the least. However, the difference in the mean energies within the beam profile is very small. Note that the energy loss of particles in the scatterer (about 13 MeV according to the stopping power tables (*PSTAR*) of the NIST, USA, `physics.nist.gov/PhysRefData/Star/Text/PSTAR.html`) is neglected in this simulation. Hence, the mean energy in the very center of the scattered beam profile is 200.0 MeV. At the position where the particle fluence has declined to 10% (15.6 cm off-axis) the mean energy is still 199.3 MeV. This shows that the influence of broad energy spectra (here with a width of 20 MeV or 10%) is very small for the passive scattering mechanism. When using a single scattering setup only the very inner part of the lateral profile can be used. A constraint could be that the fluence is at least above 90% of the maximum. In figure 3.2 this is within a circle of 3.3 cm around the beam axis. Hence, only a very small part of the full number of particles is used. Additionally, the scatterer of 5 mm is quite thick (and causes a lot of energy loss). Therefore, for real applications double scatterers are used. However, the findings from above are still valid. The lateral spreading of the beam does not introduce a relevant location-energy-dependence.

3.1.2 Active scanning

To emphasize its technical realization, the delivery technique for IMPT is usually called *active scanning* or *spot scanning*. As explained earlier, the tumor is not irradiated at once but is split into many sub-volumes called *spots*. The sub-division in the axial direction is based on setting the correct energy for the different depths within the tumor. With a synchrotron, the accelerator energy can be adjusted directly. For cyclotrons, it is done by inserting a degrading material (like Lucite) into the full energy particle path. This system is referred to as *range shifter* or *degrader*. The sub-division in the lateral direction is done by scanning the beam magnetically (this is where the name *scanning* comes from) [24]. The resulting dose delivery scheme can be seen in part (b) of figure 3.1. In the following it is analyzed to what extent scanning is possible with broad energy spectra. Therefore, an equation for the deviation in an magnetic field is necessary. Subsection 2.2.1 dealt

with the very similar problem of the magnetic energy selection system. The geometry of active scanning is essentially the one from the energy selection system, but with the first magnet and the drift space only (compare to figure 2.4). The calculation there, arrived at a total deviation of $y = y_1 + y_2 + y_3$ which (because of $y_1 = y_3$) was $y = 2y_1 + y_2$. Here, the deviation is $y = y_1 + y_2$. Therefore, the final deviation for magnetic scanning is given by equation 3.1:

$$y = r\left(1 - \cos\left(\arcsin\left(\frac{l}{r}\right)\right)\right) + s\tan\left(\arcsin\left(\frac{l}{r}\right)\right) \tag{3.1}$$

The dependence on the particle kinetics is hidden in the radius of gyration which is given by $r = \frac{p}{|q|B}$. In terms of the kinetic energy T this is $r = \frac{\sqrt{(mc^2+T)^2-(mc^2)^2}}{|q|Bc}$. For example, a 200 MeV proton in a system with $B = 1$ T, $l = 10$ cm and $s = 1$ m is deflected to a position with $y = 4.9$ cm. For the limit $l \ll r$ (short field and/or weak field and/or fast particle) a Taylor expansion of equation 3.1 gives:

$$y = sl\frac{|q|Bc}{\sqrt{(mc^2+T)^2 - m^2c^4}} + O\left(\left(\frac{l}{r}\right)^2\right)$$

The relative positioning error of the scanning process when using wider energy spectra is of interest. Hence, let Δ be a small deviation from the kinetic energy T. Keeping $l \ll r$ and using the further approximation $\Delta \ll T$ the Taylor series gives:

$$\frac{y_{T-\frac{\Delta}{2}}}{y_{T+\frac{\Delta}{2}}} = 1 + \underbrace{\frac{mc^2+T}{2mc^2+T}}_{=:\,a}\left(\frac{\Delta}{T}\right) + O\left(\left(\frac{l}{r}\right)^2\right) + O\left(\left(\frac{\Delta}{T}\right)^2\right)$$

The coefficient a for protons (70 to 250 MeV) is between about 0.52 and 0.56 and for carbons (70 to 450 $\frac{\text{MeV}}{\text{u}}$) is between about 0.52 and 0.60. Therefore, keeping all approximations in mind, it can be *roughly* said that:

$$\frac{y_{T-\frac{\Delta}{2}}}{y_{T+\frac{\Delta}{2}}} \approx 1 + 0.5\left(\frac{\Delta}{T}\right)$$

Now it is remarkably easy to estimate the positioning error of a magnetically scanned beam. For example, if the (kinetic) energy spread is 10%, the positioning error will be 5%. This equation also shows that large scanning distances (y) are a problem for non-monoenergetic beams. Let us limit the absolute positioning error to 2.5 mm and the scanning distance to 10 cm (i. e. 20 cm irradiation field length). In this case the

allowed relative positioning error is 2.5%. Therefore, the allowed energy spread is 5%. Smaller field sizes do not show such a great dependence on the energy and could hence be realized even with broader energy spectra. Note again, the scanned beam has already passed the energy selection system and is therefore not necessarily as broad in energy as the initially accelerated beam.

3.2 New combinations of established methods

So far only two extreme cases of a range of dose delivery schemes have been mentioned: In *passive scattering* the whole tumor is irradiated at once with one beam setting. In *spot scanning* the tumor is split into many sub-volumes which are irradiated independently. Figure 3.3 shows these established methods and further possibilities which are intermediate steps between them. Each closed blue area is irradiated separately. For laser accelerated particles this means that each of these areas can be treated with one or more laser shots.

- **(a) passive scattering**: This classical delivery scheme is normally irradiated with passive beam shaping components only, where all parts of the tumor are treated simultaneously. This scheme shows dose in the proximal part of the normal tissue surrounding the tumor and is therefore inferior to all other schemes.
- **(b,d) axial clustering**: As already seen for passive scattering, a range modulator wheel can produce different particle energies to irradiate bigger axial extents of the tumor at once. Laser accelerated particle beams show an intrinsically broad spectrum of energies which entitles them to produce wider axial dose distributions. However, without further measures the amount of particles per energy is not suitable for a flat axial dose distribution (SOBP). Chapter 5 introduces two methods that demonstrate how to get around this constraint: First, by adding an additional scattering material to the energy selection system, the spectrum can be modified in a way that allows the delivery of SOBPs within one laser shot. Second, differently wide energy spectra can be superimposed in a certain way that produces flat depth dose curves while preserving the distal sharp dose falloff of monoenergetic beams. Depending on how broad the used spectrum and the lateral extent of the tumor is, the lateral displacement can either be done with magnetic scanning or with a MLC.
- **(c,e) lateral clustering**: With the help of a collimator in the particle selection system wider lateral extents of the tumor can be irradiated at once. Additionally,

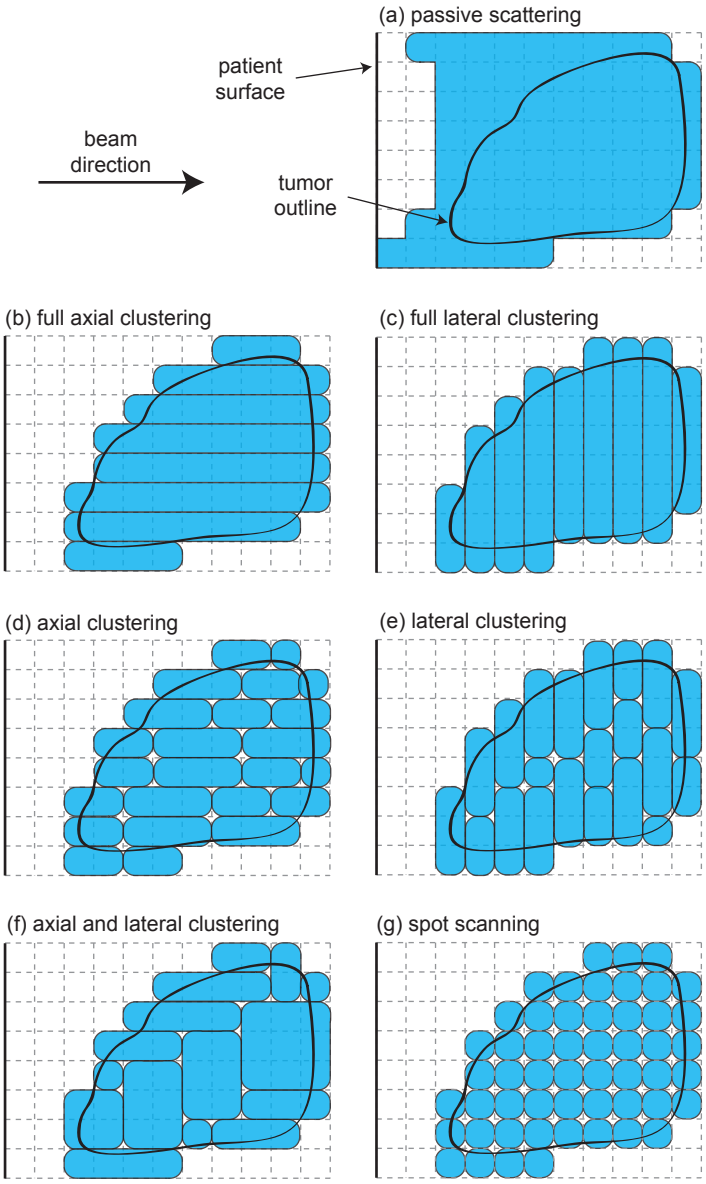

Figure 3.3: Dose delivery schemes. See section 3.2 for a detailed description. Compare to figure 3.1 that only pictures the established dose delivery schemes. Each closed blue area is irradiated independently. The figure shows the geometrical dose distribution only. Spot weights are not included. As before, this drawing assumes a parallel incoming beam and a water phantom.

when using a MLC the shape of these areas can be arbitrary. In the literature, *full* lateral clustering is known as *layer stacking* [23].

- **(f) axial and lateral clustering**: The combination of both methods can be used to irradiate the tumor.
- **(g) spot scanning**: The classical delivery scheme which is normally associated with IMPT. Each spot is irradiated independently. The only practical way to deliver so many independent dose spots is to use magnetic scanning for the lateral direction.

Closed areas being irradiated independently may have different weights (i. e. different doses). Therefore, the number of degrees of freedom in the dose optimization problem increases from case (a) to case (g). Clearly, the final dose distribution is better for case (g) since all other distributions can be achieved with it as well. However, the extra degrees of freedom might not be necessary. It is shown later to what extent the number can be decreased without changing the resulting dose distribution too much.

There is another property of the dose delivery that is of interest for laser accelerated particles. First, let us assume we have a conventional system with spot scanning (case (g)). As mentioned, the energy for the different layers in different depths has to be changed. This procedure is usually much slower than the magnetic scanning in the lateral direction. Therefore, when performing the treatment, the beam is set to a certain energy which is kept constant until the whole layer has been scanned magnetically. Not till then the energy is changed to the next value. Let us call this *layer processing*. If the lateral beam placement was slower than the axial one, the treatment would be performed the other way round. First, one lateral position would be treated with all necessary energies and only after this the lateral position would be changed. Let us call this *depth processing*. In the literature, this procedure is called *depth scanning* [57]. Figure 3.4 illustrates these processing modes. Depending on the dose delivery system of a laser accelerated particle treatment unit, depth processing (case (b)) could be faster than layer processing (case (a)). This would for example happen, if the lateral beam placement had to be done with a slow MLC and the axial position was chosen with a fast range shifter or a fast energy selection system. Note that this technique can be combined with the use of wider energy spectra as well. In this case, a few of the dose spots in each closed red area of figure 3.4 could be combined to one new spot. Additionally, case (c) depicts a combination of layer and depth processing called *volume processing*. Here, the delivery is first performed for small areas that extend laterally and axially. No new volume is started until then. This scenario is likely if small lateral displacements

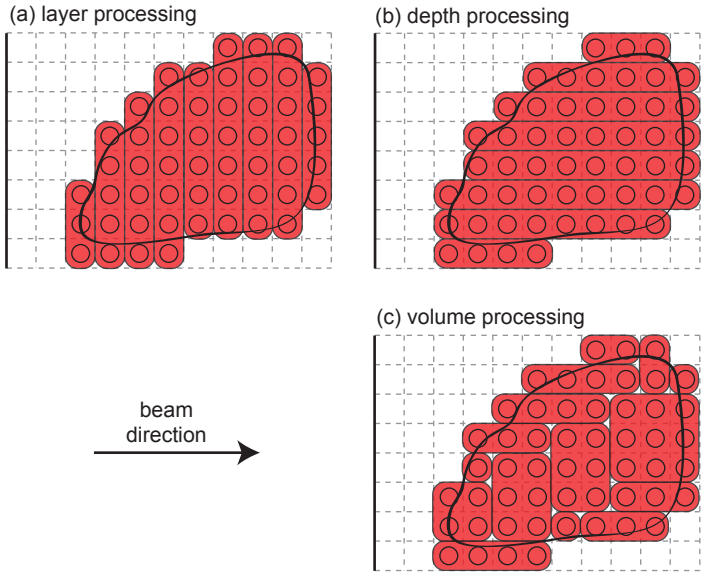

Figure 3.4: Processing modes. See section 3.2 for a detailed description. All independent dose spots (depicted as black circles) *within* each closed red area are irradiated successively. Only after processing one area completely the next one is started. Note the similarities and differences compared to figure 3.3.

can be scanned magnetically and bigger ones have to be achieved in another way (MLC or other techniques which can be found in section 3.4).

3.3 Components of a treatment head

So far various hardware components to handle laser accelerated particles have been introduced (namely the energy, particle and fluence selection systems). Additionally, dose delivery schemes (passive scattering, active scanning and also new methods) have been mentioned. The next step is to put the system together in one piece. Figure 3.5 shows one potential implementation of the complete treatment head of a laser accelerated irradiation facility. In the following each element is explained starting upstream:

- **laser**: The laser generation itself probably takes place in a separate room (not shown). Then, the laser is directed into the treatment room with mirrors.
- **parabola**: An off-axis parabolic mirror is used to focus the broad parallel laser beam to a small spot of about 1 μm^2. Only in this spot the highest laser intensity is reached. If a laser beam arrives parallel to the semiaxis of a parabola, but offset to it, it will be focused to a certain point on the semiaxis itself (see section 3.4).

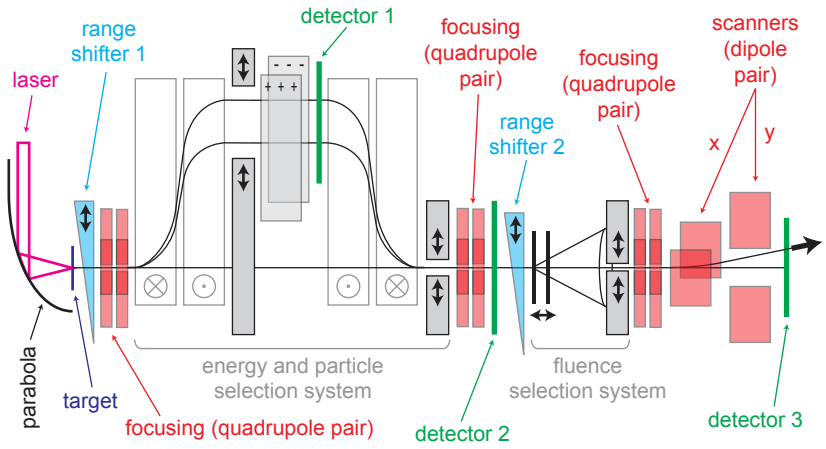

Figure 3.5: Simplified drawing of a potential treatment head of a laser accelerated particle therapy system. See text for details. A setup with an active scanning apparatus is shown. If the collimator of the fluence selection system was a multi leaf collimator, the last (most downstream) focusing element and the *scanners* could be removed. Then, the setup would be a passive scattering one. Note that in this drawing everything downstream of the capacitor has to be bent into the plane of projection to adjust to the particle type selected by the electric field.

- **target**: The target is positioned at the laser focus point on the semiaxis of the parabola. Here, the plasma is generated and the particles are accelerated. Other than depicted, the target is usually not irradiated at an angle of 90° to prevent reflection into the laser system.

- **range shifter 1**: A range shifter reduces the particle energies by a predefined amount. The optimal case would be that it does not introduce any scatter. Therefore, it is usually made of Lucite. It can be moved in and out of the beam to regulate its degrading capability. Range shifter 1 can be used if the energy spectrum produced by the laser is too high for the treatment of the tumor in general. As opposed to range shifter 2, which can be found further downstream, this one can be rather slow since it does not have to be changed very often. Since a range shifter creates secondary radiation it should be as far away from the patient as possible.

- **focusing (quadrupole pair)**: Focusing of the beam is necessary at several points of the system. The drawing does not claim to have the right amount of focusing elements nor does it claim to have them at the optimal positions. However, laser

accelerated particles show a wide angular spread when leaving the acceleration target. Therefore, before entering the energy and particle selection system, they have to be refocused. For this purpose, a pair of small permanent magnetic quadrupoles could be used [47]. Especially for lower energy setups they provide a promising alternative to electromagnetic magnets as used in conventional beamlines. The next focusing position could be behind the energy and particle selection system. And last but not least, if an active scanning system is used, it could prove useful to refocus before scanning as well. It has to be mentioned that the quadrupoles provide an additional energy filter [38] which is independent of the energy selection system.

- **energy and particle selection system**: This system was described in detail in subsections 2.2.1 and 2.2.3. It filters energy and particle type.

- **detector 1**: This detector, placed in the middle of the energy and particle selection system, where particles are unraveled depending on their properties (energy, particle type), measures the fluence of the particles at different locations. The location can be translated into particle energy and particle type. Therefore, it provides information about the spectrum of the beam. This detector may only give relative fluences but it needs to be an *online transmission* measurement. A possible way of handling the high dose rates of laser accelerated particles might be the use of high resolution semiconductors in charge-coupled devices. Because of their small pixel size the amount of particles per pixel would not be too high even for the very high fluences encountered with laser-driven particles. However, also conventional *multiwire systems* (ionization chambers) could be used if they can handle the high fluences. Since the depicted setup is not a constructional drawing it does not include backup or safety elements. In a real treatment head all detectors should exist twice.

- **detector 2**: This detector should measure the fluence of particles independent from their energy and type. It has to provide absolute dosimetric values (with the help of detector 1) in an online transmission measurement.

- **range shifter 2**: In principle, the second range shifter does the same than the first one, but needs a smaller maximal shifting amount. It could be useful to have a *fast* energy degrading possibility in addition to the initial one. Since it is further downstream it does not change many beam parameters. It could be used for intra-fraction or intra-field changes of the energy.

- **fluence selection system**: The system to select the appropriate particle fluence was described in detail in subsection 2.2.2. It is able to reduce the number of particles for certain shots. If a passive scattering system is used instead of the shown active scanning system the fluence selection system also provides a way to irradiate bigger lateral extents. To transform the shown setup into a passive scattering system, the last focusing element and the scanners have to be removed. Additionally, the beam blocker of the fluence selection system should be a multi leaf collimator to produce various lateral beam profiles and to avoid the necessity of patient specific hardware.

- **scanners (dipole pair)**: The scanner for both x and y-directions is used for the active scanning system. This system is composed of a pair of dipole magnets. As described in subsection 3.1.2 active scanning is only possible if the energy spread of the used beam is not too wide. Otherwise the scanning range is limited or passive scattering has to be used.

- **detector 3**: Finally, the third detector is used to measure the lateral beam profile generated by either the active scanning system (shown) or by the MLC of the passive scattering system. This measurement may be a relative measurement, but has to be an online transmission measurement giving spatial information in two dimensions.

To be able to irradiate the patient from all directions, the treatment head as outlined above has to be moved around the patient. Therefore, the whole system needs to be compact and stable. To fit into a treatment room the length of the setup should be minimized. A goal should be to keep it below 2 m plus an additional drift space to the patient that is as small as possible (about 0.5 m). The next section will elaborate on possible irradiation strategies including the movement of the treatment head.

3.4 The advanced method called gantry scanning

Before getting to possible treatment head movements let us first analyze the focusing parabola in more detail. This is necessary to understand the available degrees of freedom for moving the beam around the patient. When looking at the placement of the laser beam inside the parabola and the resulting outgoing beam, there might be shifting and tilting directions of the incoming beam which do not change the focusing capability of the parabola at all and others that destroy the focus completely. Figure 3.6 shows the geometry of the reflection of the laser beam inside of the parabolic mirror. The

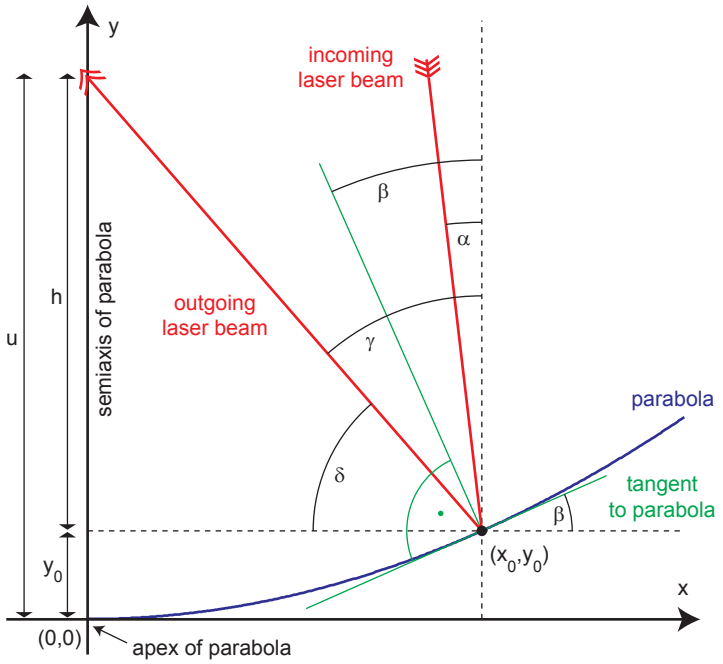

Figure 3.6: Geometry of the laser beam reflection inside of a parabola. See text for details.

functional form of the parabola is given by $f(x) = px^2$ (more accurately, it is a two-dimensional function, however, the extra dimension is not important for the calculation and is therefore suppressed here). Note, that in this section, p is just a parameter, not the momentum of a particle. The apex of the parabola is at the origin of the coordinate system. The laser hits the surface at the point $(x_0, f(x_0) = y_0)$. With the angles defined in the drawing it is:

$$\tan\beta = \frac{\partial f(x)}{\partial x}|_{x=x_0} \quad \rightarrow \quad \beta = \arctan\left(\frac{\partial f(x)}{\partial x}|_{x=x_0}\right)$$

$$\gamma = \beta + (\beta - \alpha) = 2\beta - \alpha$$

$$\delta = 90° - \gamma$$

$$\tan\delta = \frac{h}{x_0} \quad \rightarrow \quad h = x_0 \tan\delta$$

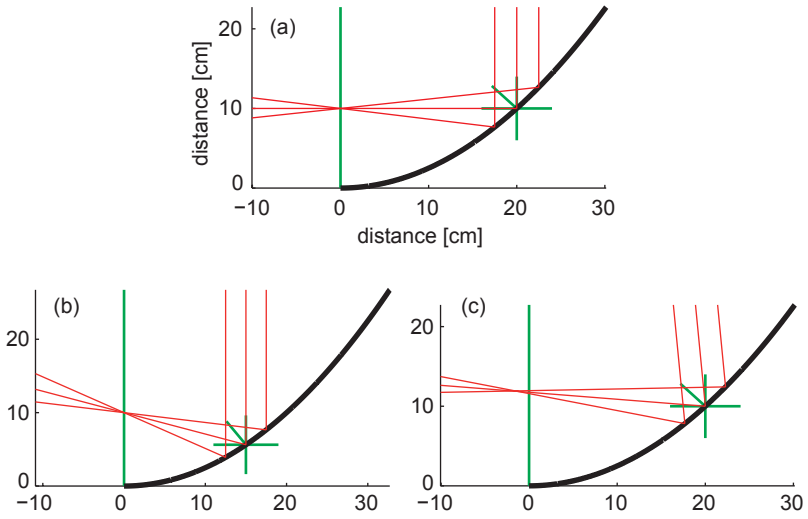

Figure 3.7: Setup stability of the reflection inside a parabola with $f(x) = px^2$ and $p = \frac{1}{40\ \mathrm{cm}}$. Compare to figure 3.6: (a) The incoming laser beam with $\alpha = 0$ and $x_0 = 20$ cm is focused at $u = 10$ cm. (b) For a lateral beam displacement to $x_0 = 15$ cm the beam stays focused. However, the angle δ of the outgoing beam is changed from 0 to 10°. (c) In contrast to this, if $\alpha = 10°$, the beam will not be focused any longer.

Hence, the distance u from the apex of the parabola to the point where the reflected laser light intersects with the semiaxis can be calculated to:

$$\begin{aligned} u &= f(x_0) + h \\ &= f(x_0) + x_0 \tan\left(90° - 2\arctan\left(\frac{\partial f(x)}{\partial x}|_{x=x_0}\right) - \alpha\right) \\ &= px_0^2 + x_0 \tan\left(90° - 2\arctan\left(2px_0\right) - \alpha\right) \end{aligned}$$

As mentioned before, all rays with $\alpha = 0$ (laser beam parallel to the semiaxis) are focused to the same point on the semiaxis. This can be seen by using $\tan(90° - z) = \cot z$, $\cot(2z) = \frac{1}{2}(\cot z - \tan z)$ and $\cot(\arctan z) = \frac{1}{z}$ to simplify the expression for u.

$$\begin{aligned} u &= px_0^2 + x_0 \cot(2\arctan(2px_0)) \\ &= px_0^2 + \frac{x_0}{2}(\cot(\arctan(2px_0)) - \tan(\arctan(2px_0))) \\ &= px_0^2 + \frac{x_0}{2}\left(\frac{1}{2px_0} - 2px_0\right) = \frac{1}{4p} \end{aligned}$$

On the other hand, for $\alpha \neq 0$ the beam is not focused at all. Figure 3.7 illustrates the

stability of the focusing process.

This information proves useful when designing the possible movements of the treatment head around the patient. Regarding the treatment head, there are two differences compared to conventionally accelerated particles. First, the gantry for laser accelerated particles is potentially much lighter and more compact since it is easier to steer the laser beam around the patient than the particle beam. This could enable more gantry movements. Second, as mentioned above, the classical active scanning could be limited by the energy spread of the particles. If passive scattering is not an option, this can lead to smaller irradiation fields. Therefore, as a new approach, a delivery with more gantry movements and less scanning might be possible. Figure 3.8 shows dose delivery scenarios for laser accelerated particles. First, *gantry scanning* is introduced:

- **(a)**: The *normal* gantry movement as known from conventional IMPT which involves both beam guides and both deflection mirrors.
- **(b)**: The treatment head together with beam guide 2 can be tilted. Deflection mirror 2 has to be adjusted. This movement changes both the treatment beam angle and source position.
- **(c)**: Another movement is based on the dislocation of the parabola within the treatment head. If it is moved perpendicular to its semiaxis (i. e. the incoming beam stays parallel to the semiaxis) the beam will stay focused onto the same point and only the outgoing angle is changed. If the rest of the treatment head (including the target) is tilted by the right amount, the treatment beam will be tilted while keeping (roughly) its source position.
- **(d)**: An elongating/shortening of beam guide 2 moves the whole treatment beam (its source position) without introducing any tilt. In addition to this (not shown) the beam could also be shifted in the direction perpendicular to the plane of projection by inserting another pair of mirrors for this movement [31].
- **(e)**: A rotation of the treatment head around the laser beam axis tilts the treatment beam perpendicular to this axis while keeping (roughly) its source position.

In addition to these movements the patient position can be relocated.

- **(f)**: Possible movements of the patient are given by table movements in all three dimensions. Note that rotations around the patient axis are not allowed to prevent organ movements. Additionally, the movements of the patient have to done very slowly.

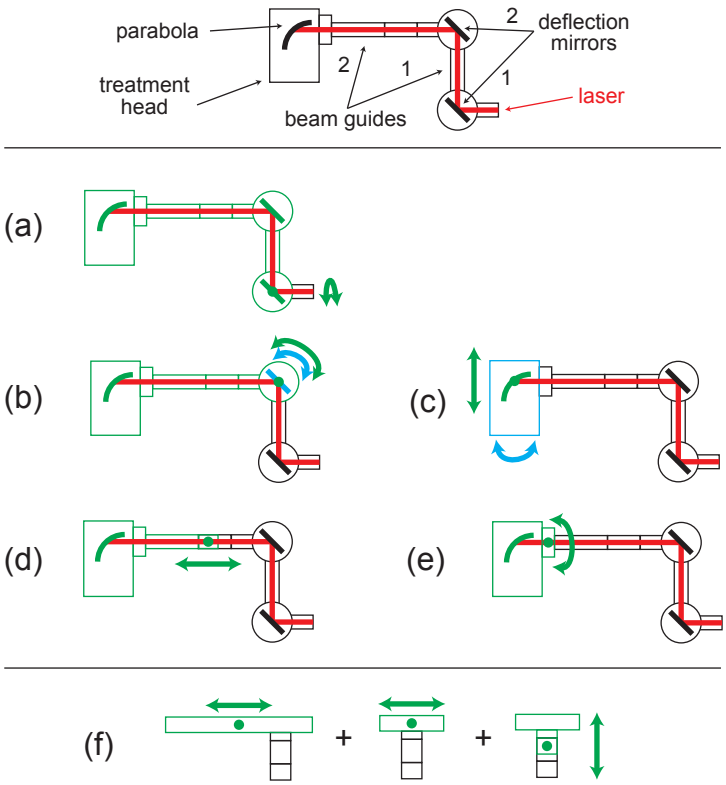

Figure 3.8: Dose delivery scenarios with a gantry for laser accelerated particles. Black parts do not move, green parts move by a certain distance, blue parts by another distance. First, *gantry scanning*: (a) *Normal* gantry movement as used in conventional IMPT. (b) Tilting of the treatment head and beam guide 2. Deflection mirror 2 has to be rotated by half the amount of the rest of the system. (c) Movement of the parabola perpendicular to the semiaxis changes the outgoing beam angle. Therefore, the treatment head has to be adjusted. (d) Elongation/shortening of beam guide 2. (e) Rotation of the treatment head. Second, *patient movement*: (f) Possible table movements accompanying the gantry scanning.

It has to be mentioned that the relative alignment of the laser and the parabola (and therefore all downstream elements as well) remains a challenging task. The accuracy has to be in the range of μm and μrad, respectively. So far even in a fixed setup without any movable parts the system is not very stable. Additionally, all cases but (a) change the *isocenter* of the machine. In radiation therapy the isocenter is the point in the middle of the treated tumor around which the whole treatment machine can rotate. Even if this constraint is not mandatory, in conventional beam delivery the isocenter is usually not changed for the whole treatment (i. e. all beam directions have the same isocenter). This simplification has to be sacrificed here in order to use the additional degrees of freedom of the laser system.

3.5 Possible scenarios

The following section deals with possible future treatment scenarios with laser accelerated particles and is therefore slightly speculative. Nevertheless, it is important to elaborate on the potential of this kind of treatment modality. As mentioned in the introduction, there are competitors to laser accelerated particle therapy that promise to deliver a low-cost high-precision radiation treatment as well. Therefore, amongst more general considerations [29, 31], the usage of laser accelerated particles for the treatment of ocular melanoma has already been proposed as a first clinical application that does not require high particle energies [53]. In the following two scenarios shall be introduced. They can be seen as two steps in the development of a treatment machine. Additionally, depending on the future laser properties it could turn out that perhaps only the first one is possible.

3.5.1 Medium-term solution: the fixed beam

Before the ultimate laser accelerated treatment device can be built the technology has to prove its potential. To do this, a somewhat limited setup could be useful as well. Of course it is of advantage if the particle beam can irradiate the patient from all directions. However, even nowadays a lot of particle facilities have fixed beam setups. For example, only the Heidelberg Ion Therapy (HIT) center has a gantry for carbon ions. Therefore, an intermediate step could be a fixed beam laser accelerated particle device. This has the great advantage that the particle acceleration process can take place in a separate room. In this separate room the potentially wide energy spectrum can be clipped to an almost monoenergetic one without great shielding limitations. The resulting particle beam can then be handled like in every other fixed beam particle

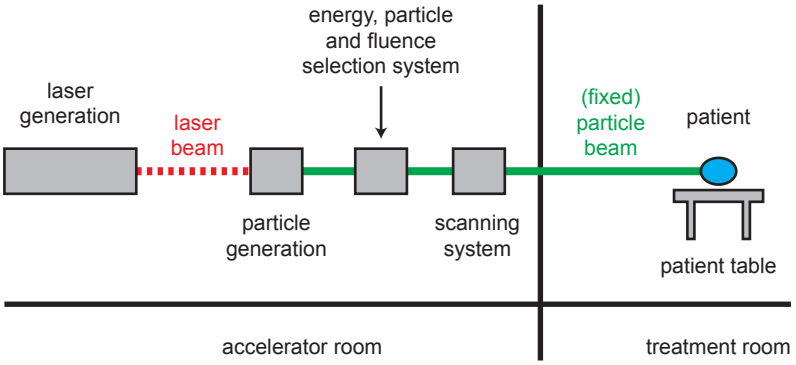

Figure 3.9: Sketch of the fixed beam scenario. For simplicity, some treatment head elements (detectors, focusing magnets, range shifters, ...) are not shown.

facility. Only the conventional accelerator itself is exchanged with a laser acceleration device and an energy and particle selection system. For the delivery itself a scanning system can easily be implemented since the energy spread is small and the drift space can be very long (the scanning magnets can be placed in the acceleration room). This setup would show that laser accelerated particle therapy is feasible and hopefully also less expensive than a conventional accelerator. A schematic drawing can be seen in figure 3.9.

3.5.2 Long-term solution: the movable gantry

Certainly, the goal should be to have a full-featured movable gantry. Only here the full potential of laser acceleration can be utilized. Namely the placement of the whole acceleration and particle preparation system on a gantry. Figure 3.10 shows how the treatment room could look like. Again, the laser beam is produced in a separate room. However, this time the laser beam is brought into the treatment room and steered around the patient by a gantry equipped with mirrors. Only in a distance of 2 to 3 m in front of the required entrance point into the patient the laser acceleration process takes place. The resulting particle beam can then impinge on the patient from the required direction in a straight line. All elements of the treatment head have to be placed in this range of 2 to 3 m. Shielding is more complicated in such a scenario. Therefore, broader energy spectra should be used (see section 3.2 and chapter 5) to utilize as many of the accelerated particles as possible. Consequently, magnetic scanning could be limited by the broad energy spectra. However, *gantry scanning* as introduced in section 3.4 could provide a solution to this problem. Short lateral distances could still be scanned magnetically (or scattered passively) and long distances could be treated with gantry scanning. As

Figure 3.10: Rendering of a possible treatment room with a movable gantry for laser accelerated particle therapy. This screenshot is taken from a video prepared by the author that can be found at `www.youtube.com/watch?v=OGj2ht37TWO`. It shows the laser beam (red) coming from the bottom left which is guided through the gantry to the treatment head (open last part of the gantry displaying the elements of the beam delivery system). The particle beam (yellow) leaves the treatment head to irradiate a patient that would be positioned on the patient table.

mentioned earlier, this scenario is speculative and future developments have to show how laser accelerated particle therapy could look like.

4 Computational considerations for the simulation of radiation therapy with laser accelerated particles

Whereas the previous chapter presented concepts of how to use laser accelerated particles for radiation therapy, the following chapters will analyze some of the presented concepts in more detail. This chapter is a technical chapter about the computational methods that have been used for the further studies.

4.1 Monte Carlo simulations

Some aspects of laser accelerated particles have been analyzed with Monte Carlo methods. For this the Geant4 particle interaction and tracking code has been used in the versions 9.2 and 9.3 (see `geant4.web.cern.ch`, [1]). It was utilized for various purposes. First, the modification of energy spectra by adding additional scattering material into an energy selection system (see section 5.2) has been examined. For this application only the trajectory and energy of the primary particle beam (proton beams have been used for simplicity) were of interest. Therefore, secondary particles could be ignored. The primary particles were simulated with the electromagnetic interactions of the Geant4 class *G4EmStandardPhysics_option3*. Nuclear interactions were not included. However, if they were taken into account, the qualitative results would not be modified. Geant4 was used in version 9.2.

The second application of Geant4 is for dose calculation purposes. This simulation was done by a colleague for proton and carbon beams [22]. The results were transformed into a database used by the experimental treatment planning system described later in this chapter. Here, all particle processes were important since the exact axial and lateral dose distribution of monoenergetic pencil beams in water were acquired. For the electromagnetic interactions the Geant4 class *G4EmStandardPhysics_option3* was used again. Nuclear interactions were simulated with the classes *G4HadronQElasticPhysics* (elastic) and *G4HadronInelasticQBBC* (inelastic). For carbon ions, the nuclear interactions of

G4IonBinaryCascadePhysics (inelastic) were added. Geant4 was used in version 9.3. And last but not least a simulation similar to the latter one has been applied to calculate depth dose curves of beams with wide energy spectra to compare the result to the treatment planning system mentioned below. Neither of the three Monte Carlo simulations claims to be precise enough for clinical applications. They should be seen as proof of principle calculations.

4.2 Experimental treatment planning system

The vast majority of studies have been performed within an experimental treatment planning system that was developed as an extension to the Matlab (`www.mathworks.com/matlab`) based software framework called *Computational Environment for Radiotherapy Research* (CERR, see `www.cerr.info`, [10]). CERR is an open source software and originates from the Washington University in St. Louis, Missouri, USA. It allows loading of CT images, region of interest contouring, dose calculation for photons, basic treatment plan optimization, and treatment plan analysis. The extension developed as a part of this thesis is called *Laser-Accelerated-Particle-CERR* (LAP-CERR). It has the added capability to calculate and optimize dose distributions for charged particles beams of arbitrary energy spectra. With this tool the whole treatment planning process for laser accelerated particles, including the properties of the energy and fluence selection system, can be performed. Later sections in this chapter will elaborate on the details of the implementation. Readers of this thesis are encouraged to request the full source code of LAP-CERR by contacting the author[1] if they are interested in further details.

4.3 Dose calculation

Dose calculation based on patient CTs is one of the most important tasks when analyzing the impact of laser accelerated particles for treatment planning. In general it incorporates every aspect of the analysis of the dose deposition in the patient. More specifically, in this thesis, it refers to the calculation of the dose that a unit amount of certain particles with a certain energy spectrum and a certain initial beam shape coming from a certain beam source location with a certain beam direction causes at a certain location in the patient. Usually a matrix D_{ij} called *influence matrix* giving information about all these possibilities is compiled [37]. It stores all doses caused by a unit amount of particles and lists them regarding different patient voxels along the column of the matrix (numbered

[1] Contact Stefan Schell (stefan.schell@tum.de).

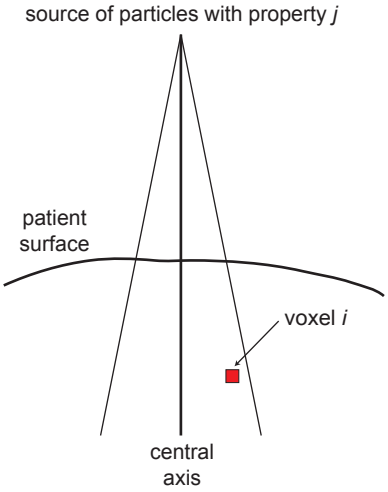

Figure 4.1: The dose calculation geometry. Particles with property j (given by a combination of particle type, energy spectrum, initial beam shape, beam source location and beam direction) cause dose in each voxel i.

with index i) and regarding the different particle properties (combinations of particle type, energy spectrum, initial beam shape, beam source location and beam direction) along the row of the matrix (numbered with index j). The calculation of this matrix is referred to as *dose calculation*. Figure 4.1 illustrates the geometry of this calculation. In the next step this matrix can be used to find the *optimal* dose distribution for the patient. This step, called *dose optimization*, tries to find out how many particles of each property j are optimal to cause a certain dose in the patient. This amount is stored in the vector ω (numbered with index j). When calling the dose in voxel i simply D_i the following equation shows the relation between the variables.

$$D_i = \sum_j D_{ij}\omega_j \tag{4.1}$$

This section deals with the pure dose calculation, the next with the dose optimization.

4.3.1 Axial and lateral dose description

Let us assume the dose $D(x, y, z)$ at every point (x, y, z) in a water phantom shall be calculated. This dose $D(x, y, z)$ corresponds to the value D_i of the last paragraph, however, for simplicity the system is described in a continuous way here. Let us also assume that a monoenergetic charged particle pencil beam with an initial Gaussian lateral profile starts at point $(0, 0, 0)$ and travels along the z-axis. Then, the dose can be

simplified by the product of the depth dose curve $D_0(z)$ and a two-dimensional Gaussian function describing the lateral profile with a depth dependent lateral spread for both the x and y-direction. This functional form is strongly motivated by equation 2.2.

$$D(x,y,z) = \underbrace{D_0(z)}_{\text{depth dose curve}} \cdot \underbrace{\frac{1}{\sqrt{2\pi\sigma_x(z)^2}}\, e^{-\frac{x^2}{2\sigma_x(z)^2}} \cdot \frac{1}{\sqrt{2\pi\sigma_y(z)^2}}\, e^{-\frac{y^2}{2\sigma_y(z)^2}}}_{\text{lateral description}} \tag{4.2}$$

As it can be seen in equation 4.2, the depth dose curve $D_0(z)$ is the dose of a beam integrated over its whole lateral extent. It depends on the particle type and its energy. The depth dependent lateral spreads $\sigma_x(z)$ and $\sigma_y(z)$ are given by the following equation.

$$\sigma_{x/y}(z) = \sqrt{\sigma_{0,x/y}^2 + \sigma(z)^2} \tag{4.3}$$

Here, $\sigma_{0,x/y}$ is the initial width of the beam before entering the water phantom in x and y-direction respectively. $\sigma(z)$ is another function depending on the particle type and its energy and gives the lateral spread at different depths caused by scattering. The reason for modeling the lateral dose with a Gaussian lies in the fact that the scattering of charged particles in matter is mainly given by multiple Coulomb scattering with the nuclei of the traversed material. This happens very often which gives rise to the application of the *law of large numbers*. Therefore, the lateral scattering can be approximated by a Gaussian. However, there are also scattering contributions from other physical effects (Coulomb scattering with electrons and nuclear interactions) which either do not contribute to the scattering very much or do not happen very often. Because of the approximations, the lateral dose distribution is not perfectly Gaussian. One approach to handle this is to use the sum of two Gaussians [22]. In this case two lateral scattering values and two depth dose curves are needed. The latter is necessary to have a value for the relative importance between the two Gaussians. Both dose description models, called 1-σ-model and 2-σ-model, have been implemented. However, it turned out that for the purpose of the analysis of laser accelerated particles for radiation therapy the differences can be neglected, hence the 1-σ-model is usually applied. It is shown in section 4.3.3 how the depth dose curve and lateral spread data can be obtained by either analytical models or Monte Carlo simulations.

4.3.2 Wide energy spectra

The previous subsection showed how to handle monoenergetic particles. For broader energy spectra the description has to be done with a superposition of all involved energies.

Therefore, the initial particle spectrum is approximated with a sum of Gaussians with equally spaced centers. For each of the energies given by the Gaussian centers the depth dose curve and the lateral spread can be obtained independently. When adding up the different contributions in their corresponding weight the full dose delivered by a particle beam can be obtained. Let k denote the different energies of the Gaussian centers of the approximation. Let λ_k be the weight, $D_{0,k}(z)$ the depth dose curve and $\sigma_k(z)$ the lateral spread of a beam with energy k. For simplicity $\sigma_k(z)$ shall already contain the initial lateral spread of the beam (which is assumed to be circular here).

$$D(x,y,z) = \sum_k \lambda_k \cdot D_{0,k}(z) \frac{1}{2\pi\sigma_k(z)^2} e^{-\frac{x^2+y^2}{2\sigma_k(z)^2}} \tag{4.4}$$

This description is correct, however, it is rather slow to compute for a real patient case. Therefore, the following approximation can be made. It is a good approximation if the $\sigma_k(z)$ are all very close to each other. In this case the sum of Gaussians is almost a Gaussian again whose combined σ can be approximated as a dose weighted sum of the original σ's.

$$\begin{aligned} \overline{D}_0(z) &:= \sum_k \lambda_k D_{0,k}(z) \\ \overline{\sigma}(z) &:= \sum_k \nu_k(z)\, \sigma_k(z) \quad \text{with:} \quad \nu_k(z) = \frac{\lambda_k D_{0,k}(z)}{\overline{D}_0(z)} \\ \rightarrow \quad D(x,y,z) &\approx \overline{D}_0(z) \frac{1}{2\pi\overline{\sigma}(z)^2} e^{-\frac{x^2+y^2}{2\overline{\sigma}(z)^2}} \end{aligned}$$

This is the same functional form than equation 4.2 and can be used as a fast, yet accurate enough, approximation for broad energy spectra. Comparisons between the simple superposition and the approximation have been performed and found no relevant difference (below 1% of the prescribed dose) for common energy spreads (up to 20 MeV wide). However, when using very broad energy spectra or when modeling the lateral spread precisely with the 2-σ-model as described in subsection 4.3.1, the correct superposition from equation 4.4 can be applied. The method to handle broad energy spectra can also be used to simulate the small energy spread that conventionally accelerated treatment beams have. Their energy spread is not supposed to be too small since the axial extent of the Bragg peak would be too small as well.

4.3.3 Analytical model and tabulated particle dose data

There are various ways to obtain the functions $D_{0,k}(z)$ and $\sigma_k(z)$. For existing treatment facilities mostly measurements are used. This is the easiest solution to incorporate all machine specific properties of the beam. However, the experimental treatment planning system used in this thesis is not meant to exactly model one specific treatment facility (which furthermore does not exist yet) but to analyze laser accelerated particles for radiation therapy in general. Therefore, analytical models or Monte Carlo simulations can be used to obtain the data.

Analytical model

For protons, an easy to use analytical description for dose calculations exists. Regarding the depth dose curve $D_{0,k}(z)$ there is a model developed by Bortfeld [3]. With this, it is possible to calculate absolute depth dose curves for all required particle energies and depths in water. For the lateral spread $\sigma_k(z)$ the generalization of the multiple Coulomb scattering equation 2.3 for thick targets can be used [13]:

$$\sigma_k(z) = 14.1 \, \frac{\mathrm{MeV}}{c} \, Z_{inc} \left(\int_0^z \left(\frac{z - z'}{p(z') \, \beta(z')} \right)^2 \frac{\rho \, \mathrm{d}z'}{L_R} \right)^{\frac{1}{2}} \left(1 + \frac{1}{9} \log_{10} \left(\frac{\rho \, z}{L_R} \right) \right)$$

Here, ρ is the density of the material, in our case usually water. By applying the analytical approximation of Bortfeld [3] again, the dependence of both the momentum p and the velocity β on the position z' can be resolved and the integral can be evaluated. This deviation can be found in the PhD thesis of Nill [36, on page 32]. The result can be used to obtain the lateral spread of particles with different energies for the dose calculation.

Tabulated particle dose data

Analytical models have their limitations. Additionally, there are no easy to use models for heavier ions like carbons. Therefore, the dose calculation can also be based on tabulated data. This data is obtained by Monte Carlo simulations (see section 4.1). However, in principle it could also be measured at a real particle beam. The disadvantage of tabulated data is that not all potentially necessary curves can be saved. Especially for wide energy spectra a big amount of curves with different energies is required for the dose calculation. As shown in the next two paragraphs, by using a dedicated algorithm only a certain set of curves has to be available. In this thesis the energy spacing in the

data table is 1 $\frac{\text{MeV}}{\text{u}}$ for both protons and carbon ions. For each energy in this table the simulation is performed with a strictly monoenergetic beam.

Note, that for every treatment planning process a mapping of the particle energy to the particle *range* is of importance. The range is usually defined as the penetration depth located behind the Bragg peak where the dose has declined to 80% of the maximum. In principle, the mapping can be deduced by analyzing the depth dose curves. For particles with analytical models there is also a direct functional relation between these variables. For other particles, if all energies are not available, the data has to be interpolated.

The algorithm that enables the generation of all required depth dose curves and lateral spreads from a limited set of tabulated data points works as follows. For the determination of the depth dose curve, the next available higher energy is used. The difference in the ranges of the higher energy curve and the required curve is calculated. Then, the high energy curve is axially shifted by this range difference. This preserves the shape of the depth dose curve at the cost of a slight energy loss. For the determination of the lateral spread, an interpolation between the surrounding available energies is done for each depth. This is possible since the lateral spread is a smooth and slowly varying function of both depth and initial particle energy. Subsection 4.3.5 contains a comparison between the analytical method and the use of tabulated particle data for the dose calculation.

4.3.4 The pencil beam

Dose calculations for treatment planning are based on CT datasets. It is done with a simple pencil beam algorithm [36]. In this thesis, a pencil beam is the particle beam that is defined by its particle type, energy spectrum, initial beam width, beam source location and beam direction and can be delivered by one setting of the beam delivery system. All dose calculations are based on laterally Gaussian shaped pencil beams with an initial beam width $\sigma_{0,x/y} > 0$. It is shown later (subsection 4.3.7) that flat lateral beam profiles can be approximated by the superposition of multiple Gaussian pencil beams. Figure 4.2 shows the geometry of such a pencil beam. For each of them one ray trace is performed along the voxels of the central axis. This means that the actual depth along this axis is transformed into a radiological depth z by scaling the length of each central axis voxel with its relative stopping power compared to water. The stopping power values are obtained via a lookup-table based conversion of the CT values. This enables the usage of water phantom data for dose calculations in the patient. Then the contribution to each voxel of the patient can be evaluated. This is done by using the radiological depth z and the distance from the central axis $r = \sqrt{x^2 + y^2}$ together with

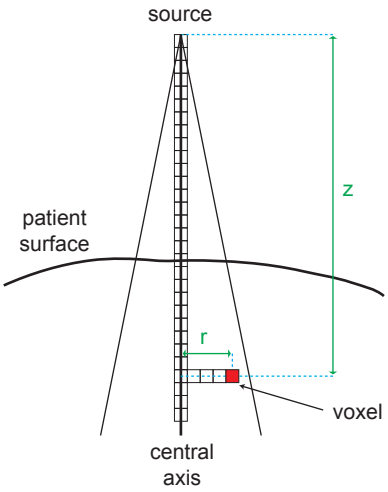

Figure 4.2: The pencil beam geometry. For each pencil beam a ray trace is performed along the central axis to determine the radiological depth. Then, for each voxel the corresponding radiological depth z and the lateral offset to the central beam axis r is used to obtain the dose by applying equation 4.2. Compare to figure 4.1.

equation 4.2. The use of only one ray trace for the full pencil beam could introduce artifacts for lateral inhomogeneities which are, however, not important for the purpose of this work [54].

4.3.5 Verification

So far, in this section the basics for dose calculations in LAP-CERR have been explained. This subsection is dedicated to some verifications for these methods. First, a comparison between the analytical model and the use of tabulated dose data is performed for protons. Figure 4.3 shows the depth dose curves and the lateral spreads for protons with 120 and 200 MeV. A small energy spread in the form of a Gaussian distribution with $\sigma = 0.5\%$ has been assumed and processed according to subsection 4.3.2. The difference between the two approaches becomes bigger for increasing proton energies. It can be attributed to the non-relativistic approximation in Bortfeld's derivation of the analytical model. Especially the ranges of higher energies are not predicted very well. This is due to the p-parameter in Bortfeld's model [3, 4] which has been obtained from measurements and does not fit very well for higher energies. Nevertheless, both methods provide roughly both the same shape and magnitude of the curves.

To examine the approximation of depth dose curves of particles with broad energy

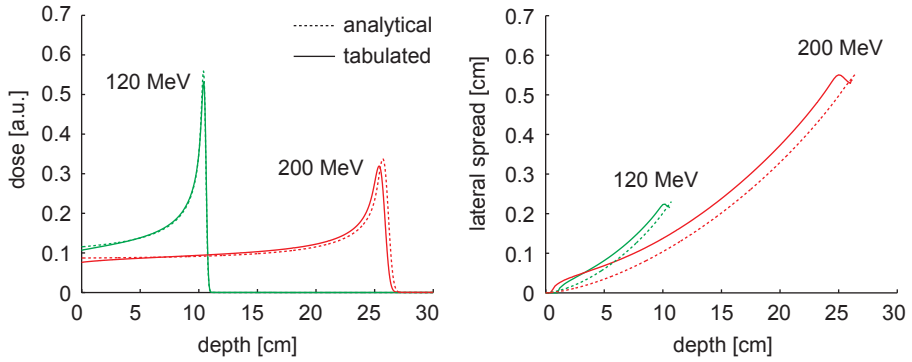

Figure 4.3: Comparison of the analytical model (dashed line) with the tabulated dose data (solid line) for protons. The figure shows the depth dose curves $D_0(z)$ (left) and the lateral spreads $\sigma(z)$ (right) for two different energies.

spectra by a sum of monoenergetic particles an additional comparison has been performed. Here, the depth dose curve of an arbitrary broad energy spectrum has on the one hand been calculated by LAP-CERR using the analytical model for monoenergetic beams and the procedure described in subsection 4.3.2 and on the other hand by a *full* Monte Carlo simulation. *Full* means that in this case the Monte Carlo simulation is not only used to compile the tabulated particle data but to calculate the whole depth dose curve with exactly the same particle energy spectrum that has been used in LAP-CERR. Figure 4.4 shows the energy spectrum and the two depth dose curves. Since in this example relatively low energies are used the deviations are very small and comparable to the findings from figure 4.3.

4.3.6 Range shifter

So far all depth dose curves have been analyzed without any additional range shifter in the beam path. However, since maybe not all required energies are provided by the laser system, a range shifter could become necessary. It can literally be seen as a block of Lucite put in front of the patient. The implementation in LAP-CERR assumes that the range shifter is right in front of the patient surface. Therefore, a possible drift space from the range shifter to the patient is neglected. This makes the calculations much easier but certainly leaves room for improvements. However, for the studies performed in the remainder of the thesis, in the cases when a range shifter was used at all, the additional drift space would not produce any significant difference. With this assumption the dose calculation with a range shifter is done by shifting the depth axis of both the depth dose

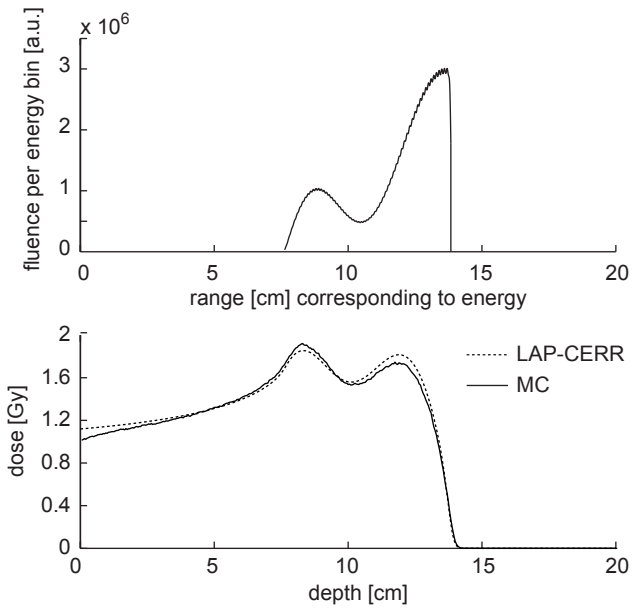

Figure 4.4: Comparison of LAP-CERR with a full Monte Carlo simulation for protons. Top: Arbitrary energy spectrum converted to ranges. Bottom: Corresponding depth dose curves of LAP-CERR using the analytical model (dashed line) and a full Monte Carlo simulation (solid line). Here, the Monte Carlo simulation is not used to compile the tabulated dose data for LAP-CERR but to calculate the whole depth dose curve for the given energy spectrum by sampling the initial particles according to this spectrum.

curve and the lateral spread by the water equivalent thickness of the range shifter.

4.3.7 Gaussian shaped irradiation or field irradiation

The previous subsections described dose calculations for Gaussian shaped lateral beam profiles. However, when using a MLC, calculations of other beam profiles which are composed of square areas are necessary: Such profiles are called *fields*. For simplicity it is assumed that the fluence throughout such a field is homogeneous and the lateral fluence decline is a perfect step function. This neglects the penumbra introduced by the collimator. However, since LAP-CERR does not describe a certain setup but a general laser acceleration machine and is meant to analyze laser specific properties this restriction is not of importance. Additionally, the actual calculation is done with an approximation by a sum of equally weighted Gaussian beams with a common σ which are arranged on an equidistant two-dimensional grid. This introduces an artificial penumbra. The higher the number of used Gaussians, the smaller the created penumbra and the more the approximation describes the lateral dose decline of a step function. To find the optimal grid distance d depending on the σ of the Gaussians the following one-dimensional consideration regarding the sum $f(x)$ of two Gaussians can be made. Note that the coefficients of the Gaussians can be set to one. The optimal distance is found if the second derivative of the sum in the middle between the two peaks is zero (see figure 4.5 for illustration).

$$
\begin{aligned}
f(x) &= e^{-\frac{\left(x-\frac{d}{2}\right)^2}{2\sigma^2}} + e^{-\frac{\left(x+\frac{d}{2}\right)^2}{2\sigma^2}} \\
\rightarrow \quad f''(x=0) &= -\frac{1}{\sigma^2} e^{-\frac{d^2}{8\sigma^2}} \left(2 - \frac{d^2}{2\sigma^2}\right) \equiv 0 \\
\rightarrow \quad 2 - \frac{d^2}{2\sigma^2} &= 0 \quad \rightarrow \quad d = 2\sigma
\end{aligned}
$$

When starting with a big distance and decreasing it little by little, at this distance the dip in the dose profile vanishes for the first time. Therefore, this distance is chosen for the approximation of flat profiles with Gaussian curves. Note that for more than one dimension and more than two Gaussians this is still a good approximation. For example, for a square field with a side length of 0.5 cm a number of $13 \times 13 = 169$ Gaussians is chosen.

When using fields for the dose delivery the concept of the influence matrix D_{ij} has to be reviewed. The j-direction of the matrix cannot contain all possible settings of the MLC. The possibilities have to be limited to a certain set of lateral profiles where each

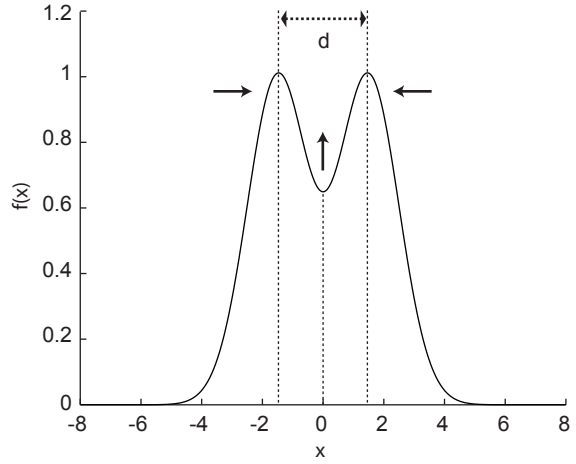

Figure 4.5: The sum $f(x)$ of two Gaussians with $\sigma = 1$ placed in a distance of $d = 3$ (at $x = \pm 1.5$). The dip between the two peaks will vanish and the second derivative $f''(x)$ at $x = 0$ will become zero if the distance between the two Gaussians becomes $d = 2\sigma = 2$. Note that the coefficients of the Gaussians are set to one.

of them can be seen as a sum of small rectangular subfields. Therefore, only the dose contribution of each subfield has to be calculated. Regarding treatment planning there are two options. First, certain subfields are added before the optimization starts. In the influence matrix this is done by adding certain columns. Second, the different subfields are kept independent for the optimization run and in the end another algorithm has to decide how the resulting combination of different subfields can be irradiated with a *smarter* choice of bigger lateral profiles. Both approaches are discussed later. For the dose calculation one has to make sure that, if two subfields next to each other, which have flat lateral profiles which are approximated by a sum of Gaussians each, are combined, the profile will stay flat over the whole lateral extent. This is achieved by placing the Gaussians at the edges at the right distance to the neighboring subfields (i. e. $\frac{d}{2}$ from the edge of the subfield). Figure 4.6 illustrates this in one dimension.

4.4 Dose optimization

As mentioned before dose optimization refers to finding the weights ω_j such that the dose in each voxel $D_i(\omega) = \sum_j D_{ij}\omega_j$ becomes optimal in a clinical sense. In this thesis the following objective function $F_0(\omega)$ is utilized for this optimization process (compare

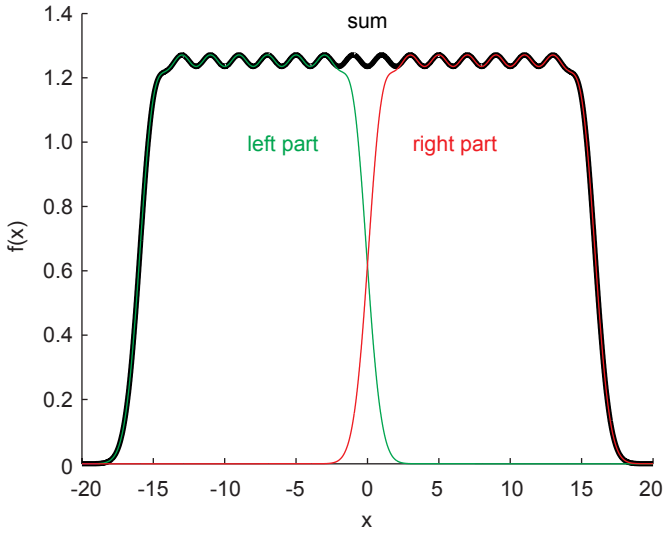

Figure 4.6: The sum of many Gaussians. Both the left and the right part are flat lateral profiles of a subfield each. They are approximated by a sum of 8 Gaussians each. If the Gaussians at the edges are placed correctly (i. e. $\frac{d}{2}$ from the edge of the subfield), the sum of both parts will stay flat over the whole lateral extent.

to [36]):

$$F_0(\omega) = \sum_i p_i \left(D_i(\omega) - D_i^0\right)^2 = \min \quad \text{subject to} \quad \omega_j > 0 \quad \forall j \tag{4.5}$$

D_i^0 are the prescribed doses for each voxel and p_i the corresponding penalty factors. Minimizing $F_0(\omega)$ means reducing the quadratic deviation of the actual from the prescribed doses in all voxels.

Before coming to the details of the optimization process the external solver Mosek (`www.mosek.com`) that was used for the mathematical optimization of the dose distribution shall be described. It solves quadratic problems with n variables and m quadratic constraints by using an interior point method:

$$\begin{aligned} & \frac{1}{2} \cdot (\vec{\omega})^t \cdot \underline{Q_0} \cdot \vec{\omega} + (\vec{c_0})^t \cdot \vec{\omega} = \min \\ \text{subject to} \quad & (l_0)_j \leq \omega_j \leq (u_0)_j \quad \forall j = 1 \ldots n \\ \text{and} \quad & l_s \leq \frac{1}{2} \cdot (\vec{\omega})^t \cdot \underline{Q_s} \cdot \vec{\omega} + (\vec{c_s})^t \cdot \vec{\omega} \leq u_s \quad \forall s = 1 \ldots m \end{aligned} \tag{4.6}$$

Note that $(\vec{x})^t$ is the transpose of $\vec{x}$. $\vec{\omega}$ ($n \times 1$ vector) is the optimization variable. $\underline{Q_0}$ ($n \times$

n matrix) and $\vec{c_0}$ ($n \times 1$ vector) are the quadratic and the linear part of the objective function and $\underline{Q_s}$ ($n \times n$ matrix for each $s = 1 \dots m$) and $\vec{c_s}$ ($n \times 1$ vector for each $s = 1 \dots m$) are the quadratic and the linear part of the constraints. Finally, $\vec{l_0}$ / $\vec{u_0}$ ($n \times 1$ vectors) and l_s / u_s (1×1 scalars for each $s = 1 \dots m$) are the lower / upper corresponding boundaries. The matrices $\underline{Q}$ have to be symmetric, which can be ensured by using only products like $\underline{Q} = \underline{\tilde{D}}^t \cdot \underline{\tilde{D}}$ with an arbitrary real matrix $\underline{\tilde{D}}$. All dose optimizations applied in this thesis have to be brought into the form of equation set 4.6.

For simplicity, let $\tilde{D}_{ij} := \sqrt{p_i} D_{ij}$ and $\tilde{\tilde{D}}_{ij} := p_i D_{ij}$. By resolving the dependency on ω the objective function $F_0(\omega)$ from equation 4.5 can be rewritten in the following way:

$$\begin{aligned}
F_0(\omega) &= \sum_i p_i \left(\sum_j D_{ij}\omega_j - D_i^0 \right) \left(\sum_k D_{ik}\omega_k - D_i^0 \right) \\
&= \sum_i p_i \left(\sum_{j,k} D_{ij}\omega_j D_{ik}\omega_k - 2\sum_j D_{ij}\omega_j D_i^0 \right) + \text{const} \\
&= \sum_{j,k} \omega_j \underbrace{\sum_i \left(\tilde{D}^t\right)_{ji} \left(\tilde{D}\right)_{ik}}_{=:\ \frac{1}{2}\left(\underline{Q_0}\right)_{jk}} \omega_k + \sum_j \underbrace{\sum_i 2 \left(\tilde{\tilde{D}}\right)_{ij} D_i^0}_{=:\ \left(\vec{c_0}\right)_j} \omega_j + \text{const} \\
&= \frac{1}{2} \sum_{j,k} \omega_j \left(\underline{Q_0}\right)_{jk} \omega_k + \sum_j \left(\vec{c_0}\right)_j \omega_j + \text{const}
\end{aligned}$$

Therefore, with $(l_0)_j = 0$, $(u_0)_j = \infty$ and no further constraints ($m = 0$) the dose optimization problem of equation 4.5 is formally equivalent to the problem in equation set 4.6. Note that this implementation does not allow different penalties for overdosage and underdosage separately. Consequently, normal tissue and organs of risk have to have prescribed doses of zero. Making the process more flexible would not be possible with Mosek since this cannot be done with a quadratic objective function. However, additional constraints can be used to help to tailor the dose distribution to the clinical treatment goals. For example, the mean target dose can be set to the prescribed target dose D^0_{target}. This is achieved by using one extra constraint (therefore, here: $m = s = 1$).

$$\begin{aligned}
&\left(\underline{Q_s}\right)_{jk} = 0 \\
&\left(\vec{c_s}\right)_j = \frac{1}{N_{\text{target}}} \sum_{i \in \text{target}} D_{ij} \quad \text{with} \quad N_{\text{target}} = \text{number of voxels in target} \\
&l_s = u_s = D^0_{\text{target}}
\end{aligned}$$

In subsection 5.3 more constraints are applied to adapt the optimization process to the properties of laser accelerated particles.

4.5 Handling of axial and lateral particle efficiency

As mentioned earlier the *axial particle efficiency* is quantified by counting the amount of particles or the amount of energy that is blocked in the energy selection system. The wider the applied energy spectra are, the more particles can be used for the irradiation. However, since this depends on the volume to be treated, the numbers should not be compared between various patients but only between different treatment plans for one individual patient. Additionally, the energy spectrum produced by the laser-driven accelerator influences the efficiency. If a spectrum that is already wider than necessary for the treatment becomes even wider, the additional particles will all be blocked and the efficiency of the system will decrease. Consequentially, since the axial particle efficiency shall describe the efficiency of the treatment plan, it should also not be compared between different incoming particle spectra.

In accordance to this, the *lateral particle efficiency* is quantified by the amount of particles lost in the fluence selection system and in a potential MLC. For a simple circular collimator it is given by the loss in the fluence selection system only. It is assumed that this circular collimator can be used to reduce the fluence to the right amount while keeping the shape of the lateral profile Gaussian. The simulation of the MLC usage is more complicated. For each field to irradiate, it is assumed that the beam can be spread to a perfectly homogeneous circle that either exactly covers all of the field's subfields simultaneously or covers a bigger area according to the required fluence reduction. No particles are scattered into the area outside of this circle which means that the fluence decline at the edge of the circle is instantaneous. Of course this is quite optimistic and completely neglects the technical realization of the spreading system. However, since the details are not known this provides an estimate on the (maximally possible) lateral particle efficiency. Additionally, the notes about different treatment volumes and different laser-driven accelerators hold true for the lateral particle efficiency as well.

5 'Advanced' radiation therapy with laser accelerated particles

5.1 Limited possibilities with the 'classical' methods

As described in section 2.3 and the corresponding figure 2.11 on page 25 the usage of laser accelerated particles together with the methods known from conventional particle accelerators imposes limitations on the treatment options. Especially the repetition rate of the laser is a crucial constraint that could render the treatment impossible. This fact is worsened by two other conditions: First, the wider the energy spectrum of the accelerated particle beam is, the more particles have to be removed from the beam and the higher the number of shots needs to be. Second, if the number of particles per shot is too high for one tumor spot, the number will have to be decreased artificially, thus again requiring a higher number of shots. Additionally, this inefficient usage of the particle beam causes a high amount of secondary radiation that has to be shielded. Therefore, adapted treatment strategies have to be analyzed to increase the efficiency of the system. This chapter elaborates on two possibilities regarding the handling of laser accelerated particles which both reduce the required number of shots and the amount of secondary radiation.

5.2 Modifying the shape of the energy spectrum

Clipping the energy spectrum in the energy selection system, i. e. setting both the lowest and the highest transmitted energy, is certainly necessary for treatment with laser accelerated particles. However, with the system introduced so far, the number of transmitted particles per energy bin cannot be changed. Nevertheless, having different particle energies in one single beam suggests that depth dose curves which are similar to SOBPs could be produced with one laser shot. The spectrum of laser accelerated particles usually decreases with energy. However, for a SOBP the number of necessary particles increases with energy. A method to change the number of particles per energy bin would be of advantage. Note that this section deals with a passive system. Particles can only be

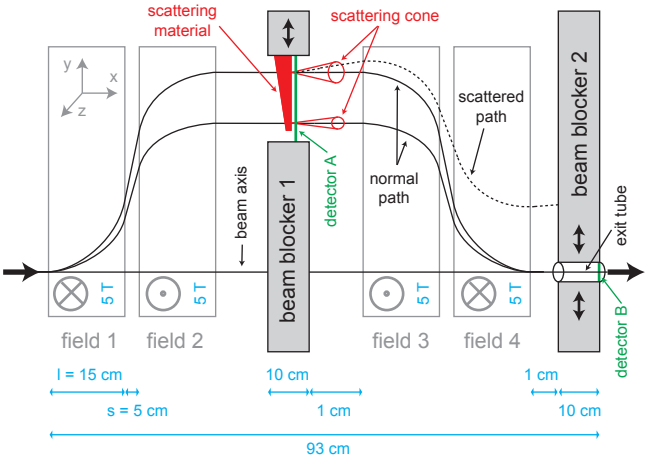

Figure 5.1: The energy selection system with additional scattering material to change the number of particles per energy bin. The beam is presented with different amounts of material thicknesses depending on the particle energy. Particles which are scattered are less likely to find the exit of the system on the right hand side. Therefore, the reduction of the number of particles depends on their energy. The drawing is not to scale.

removed from the system or their energy can be degraded but particles can neither be added to nor accelerated by the system. In the following a modification to the energy section system that is capable to selectively remove particles is introduced and analyzed. It is based on an additional scattering material within the energy selection system that adds different amounts of lateral scattering to particles with different energies. This mechanism is similar to the concepts described in a patent granted to Kraft [27].

Without loss of generality it is assumed that only one particle type is present in the accelerated particle spectrum. Therefore, a particle type selection is not necessary. For simplicity, the analysis is restricted to protons, however, the concept is suitable for carbon ions as well. Parts of this section have been published by the author [44].

5.2.1 The simulation

Figure 5.1 shows the energy selection system with an additional scattering material. Since in the middle of the system the particles are separated in space depending on their energy, their number can be reduced separately. The scattering material inserted at this location varies in thickness. The more scattering is introduced the more the particles are deflected from the normal path in the last two magnetic fields and the less likely they reach the exit on the right hand side. Since the number of particles needs to be

reduced the most for low energies, the upper part of the scattering material is thicker in general. The differently sized scattering cones are to visualize typical scattering angles for different thicknesses of the scattering material. Additionally, there is a certain amount of particles with the highest energies that are not presented with scattering material at all. Monte Carlo simulations with Geant4 are performed to show the effect of the scattering material within the energy selection system.

For this purpose, the quantities of the energy selection system mentioned in subsection 2.2.1 are used again: the absolute value of the magnetic flux density of the four fields $B = 5$ T, the length of each of the four fields $l = 15$ cm and the separation between the first and the second and between the third and the fourth field $s = 5$ cm. Additionally, both beam blockers are made out of lead and have a thickness of 10 cm each. The distance between beam blocker 1 and the third field is 1 cm. The distance between the fourth field and the exit tube, which is a cylinder cut into beam blocker 2, is also 1 cm. This tube parallel to the beam axis has a diameter of 0.5 cm and a length of 10 cm. There are two detectors: Detector A is placed downstream of the scattering material and detector B at the end of the exit tube. The whole system has a length of 93 cm. Note that the coordinate system for this section is the one depicted in the upper left corner of figure 5.1 to match the one used for the Monte Carlo simulation. Therefore, the beam axis is along the x-axis and the particles are separated by energy along the y-axis by the magnetic fields parallel (or antiparallel) to the z-axis. The main interest of the simulation is on the primary protons which are sent into the simulation box along the x-axis with the required initial energy distribution and leave it with different properties. The detection accuracy was 0.25 MeV for energies, 0.02° for angles and 0.1 mm for positions. Interactions of the protons with material change their number and direction and degrade their energy. A proton is counted to successfully exit the system if it completely passes the exit tube (detector B). It is supposed that additional magnets can be applied to collimate the remaining part of the beam behind the tube. Since secondary radiation is not further analyzed the simulation is very fast and robust. The depth dose curves in water corresponding to the transmitted spectra are not part of the Monte Carlo simulation but are calculated with the models described in section 4.3. For the dose calculation purpose the particles are assumed to be in a parallel broad beam.

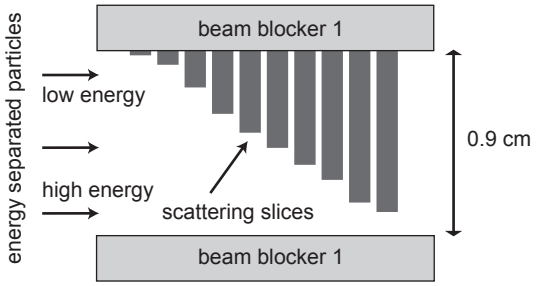

Figure 5.2: The stack of slices used to modify the energy spectrum within the energy selection system. This part replaces the linear wedge as the scattering material in figure 5.1. All protons enter on the left-hand side and fly parallel to the horizontal axis. High energy protons move through the lower part, low energy protons through the upper part of the system where they experience more scattering. The setup is optimized to produce a depth dose curve with a SOBP. The lengths of the slices are to scale, the thicknesses are not. Each slice is made of lead and is 60 μm thick.

5.2.2 Proof of concept setups

Linear wedge

Two different test cases are chosen to demonstrate the capability of the scattering material to produce depth dose curves similar to SOBPs. *Test case 1* uses a flat incoming fluence spectrum. This can in practice be achieved by a Gaussian distribution with a width that is big compared to the range of interest. It applies a *linear wedge* made out of lead as the scattering material. Again, lead is used since it has the highest scattering to degrading capability. This case shall show the potential of the system without making the setup too complicated. The gap between the two parts of beam blocker 1 is adjusted to transmit energies from 132 to 148 MeV. This corresponds to an opening width of 0.6 cm at a center position of 9 cm above the beam axis. The thickness of the lead wedge varies linearly from 340 μm (low energy side, i. e. upper part of the drawing) to 100 μm (high energy side) over 0.55 cm. The remaining 0.05 cm gap is left open to allow the transmission of high energy particles without any scattering.

Stack of slices

Test case 2 uses an exponentially decaying spectrum which decays to $e^{-1} \approx 37\%$ over a range of 40 MeV. The fluence spectrum is shaped with ten lead slices. Here, the transmission window is set to 0.9 cm at a center position of 7.7 cm corresponding to transmitted energies from 165 to 201 MeV. Each of the ten lead slices has a thickness

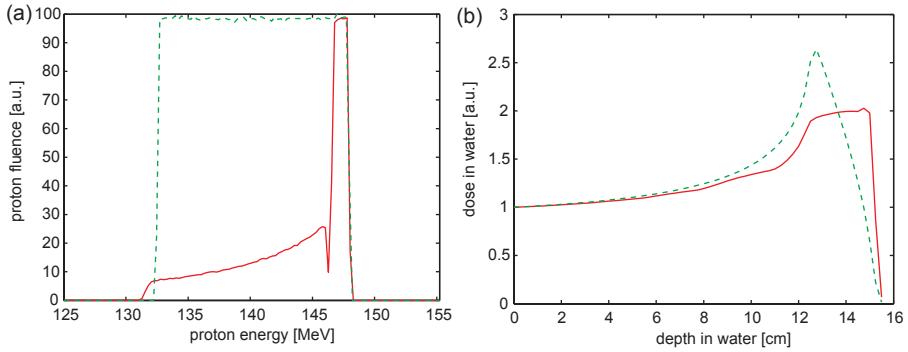

Figure 5.3: Test case 1: spectrum modification with a simple lead wedge. (a) Collimated (dashed) and final (collimated and modified by lead wedge) spectrum (solid). (b) Corresponding depth dose curves. The final spectrum has a depth dose curve that is more suitable for radiation therapy with protons.

of 60 μm. They are arranged as depicted in figure 5.2. This setup allows a better optimization of the resulting depth dose curve and therefore wider SOBPs. Additionally it can be adapted to different initial spectra by moving the individual slices. No analytical method to determine which slice setting has to be used to form a given spectrum into a desired one has been applied. Instead, the results are obtained by manually adjusting the slice parameters. A possible procedure is to determine, for each energy, the protons' position in the separation plane and then put as much material into the beam path as required to reduce the number of transmitted protons of this energy to the desired level.

5.2.3 Results for the proof of concept setups

Linear wedge

Figure 5.3 shows the fluence spectrum and the corresponding depth dose curve in water for test case 1 with the linear wedge. In part (a) the spectrum collimated with beam blocker 1 (dashed line) and the final spectrum (solid line), which has been collimated with the beam blocker and modified with the wedge, is plotted. Part (b) shows the corresponding depth dose curves. They are normalized to a common entrance dose. The shape of the modified curve resembles a SOBP with a range of 15.1 cm (distal 80%) and a modulation width of 2.7 cm (proximal 90% to distal 90%). Furthermore, it has a much sharper dose falloff and is therefore more suitable for therapy. The dint in the final fluence spectrum at about 146 MeV is due to a slight energy loss in the scattering material and is analyzed in subsection 5.2.4.

To illustrate the system's functionality figure 5.4 is a plot of the angular distribution

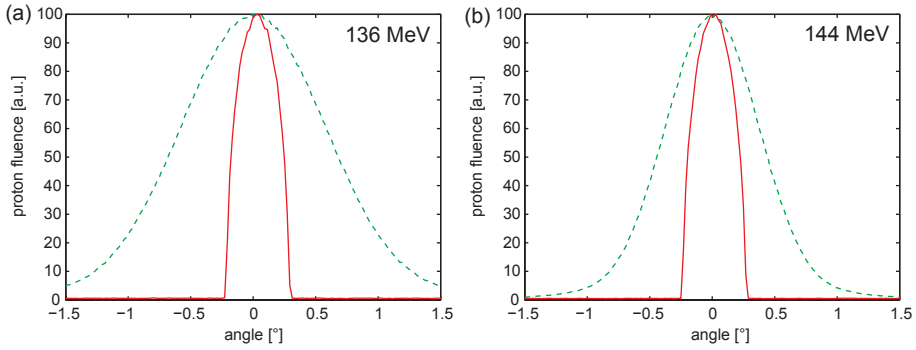

Figure 5.4: Angular distribution in test case 1 for 136 MeV (a) and 144 MeV protons (b): Dashed lines show the distribution behind the scattering material and solid lines the distribution behind the exit tube. The shown angle is the deflection in y-direction. All curves are normalized to their peak value. Whereas the angle dependent final transmission through the exit tube is the same for both energies, the deflection within the scattering system is bigger for low energy protons. Therefore, the transmission is higher for higher energies.

of protons with 136 MeV (a) and 144 MeV (b) for test case 1. Dashed lines show the distribution behind the scattering material (detector A in figure 5.1) and solid lines show the final distribution behind the exit tube (detector B). The plot analyzes the deflection in y-direction which is slightly asymmetric behind the exit tube (shifted towards positive angles) because of a small energy loss in the scattering system (which shifts the center of the beam to $y < 0$ at detector B). The corresponding deflection in z-direction is qualitatively the same but symmetric (not shown). All curves are normalized to their peak value. The angle dependent final transmission through the exit tube is very similar for both energies (full width at half maximum (FWHM) is 0.4°) but within the scattering system low energy protons are scattered more (FWHM is 1.4°) than high energy ones (FWHM is 0.9°). This reduces the relative number of low energy particles compared to high energy particles. At 136 MeV the final transmission is 10.3%, at 144 MeV it is 22.8%, which is in agreement with figure 5.3 (a).

Stack of slices

As a second application, figure 5.5 shows plots for test case 2 with ten lead slices (arranged as depicted in figure 5.2). The final spectrum has characteristic wiggles that are produced by the cascaded slice setup. The corresponding depth dose curve shows a SOBP (range: 25.2 cm, modulation width: 7.4 cm) which has, again, a very sharp dose falloff compared to the depth dose curve of the spectrum that is just collimated.

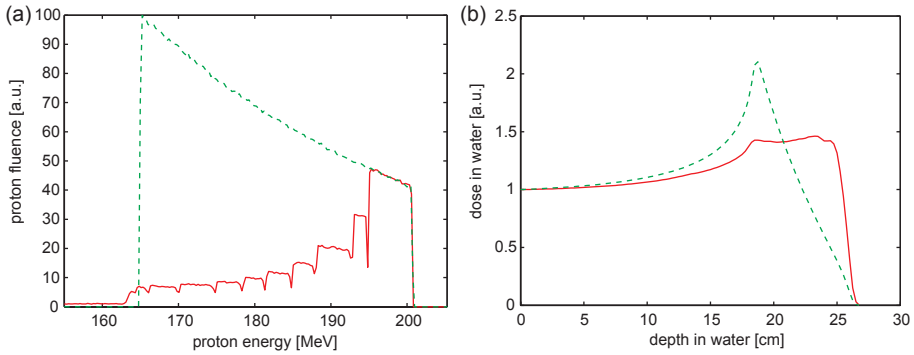

Figure 5.5: Test case 2: spectrum modification with ten lead slices. (a) Collimated (dashed) and final (collimated and modified by lead slices) spectrum (solid). (b) Corresponding depth dose curves. The final spectrum has a depth dose curve with a wide SOBP.

5.2.4 A more detailed analysis

The results presented so far show that the modification of particle fluence spectra with additional material in the energy selection system can provide SOBPs within one laser shot. This subsection illustrates the functionality in more detail and also shows some problems of the setup.

Contribution of the multiple scattering process and the energy loss in the scattering material

Figure 5.6 shows the contribution of multiple scattering to the functionality of the modified energy selection system. The settings from the linear wedge setup (test case 1) have been used. The spectrum collimated with beam blocker 1 together with the final spectrum (collimated and modified with the lead wedge) both with and without the multiple scattering process is plotted. The latter is obtained by switching off the multiple scattering process called *msc* in Geant4. Note that all other (electromagnetic) processes are activated in each of the three cases. The process *msc* is the continuous Geant4 handling of multiple scattering of charged particles traversing matter. However, there are other discrete scattering contributions which have not been deactivated. For the plot it becomes obvious that the energy loss in the scattering material is of minor importance compared to the scattering process. Another interesting feature is the dint in the particle distribution at about 146 MeV for the particles that have been modified by the lead wedge. All particles traversing the scattering material are subject to a small energy loss. Therefore, their spectrum is shifted to the left. However, particles which do

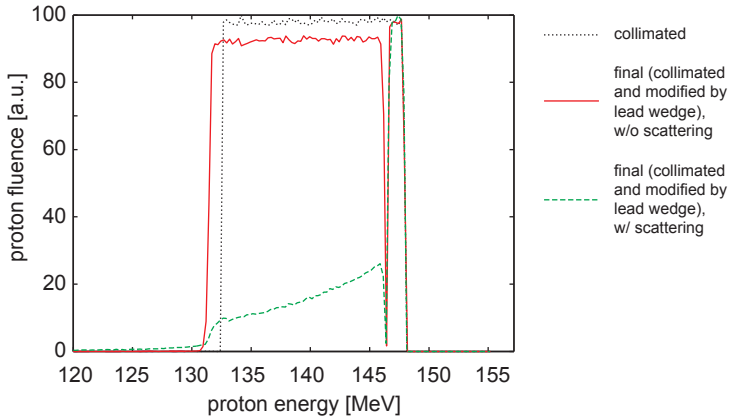

Figure 5.6: The contribution of the multiple scattering process and the energy loss to the functionality of the modified energy selection system. The terms *w/o* and *w/ scattering* refer to the deactivation and activation of the Geant4 process called *msc*. All other processes are activated in each of the three cases (electromagnetic only). See text for details.

not traverse the material are not shifted. The interface between the edge of the linear wedge and the gap where particles can pass through without scattering is at a distance of 8.75 cm above the beam axis. According to equation 2.1 this corresponds to 146.8 MeV. Therefore, particles with a slightly lower energy than 146.8 MeV lose energy and are shifted to the left and particles with a slightly higher energy than 146.8 MeV are not shifted. This causes the dint at about 146 MeV. The phenomenon is also visible in test case 2 (see figure 5.5). Both final curves (with and without the scattering process) show an unmodified amount of particles per energy bin for energies above 146.8 MeV since these particles do not traverse any material. For energies below this value, the curve with the scattering material but without the scattering process (i. e. mostly energy loss in the scatterer) is slightly below the curve that does not have the scattering material. This is because these particles are redistributed over the spectrum down to lower values due to the energy loss and an additional energy broadening. Note that no particles are lost since the energy loss is not big enough to cause a shift of the beam in negative y-direction that would not allow the particles to exit the system (the shift is smaller than the radius of the exit tube).

Particle fluence and mean energy in dependence of the final particle position

Particles which have not traversed the scattering material are steered back to the initial beam axis by the third and fourth magnetic field and leave the system flying along the

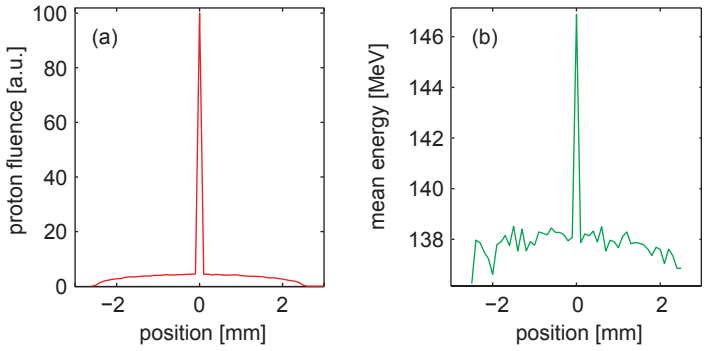

Figure 5.7: Particle fluence (part (a)) and mean energy (part (b)) in dependence of the location within the exit tube (y-axis of detector B). The wiggles in part (b) are due to poor statistics. See text for details.

beam axis (restoring and then keeping $y = 0$, $z = 0$). Scattered particles, however, besides from having a direction which is not perfectly parallel to the beam axis, do not come back to this axis but arrive at a slightly shifted location ($y \neq 0$, $z \neq 0$) because of their energy loss and the scattering process. Figure 5.7 shows, again for test case 1, both the proton fluence (part (a)) and the mean energy (part (b)) in dependence of the location along the y-axis in the exit tube (detector B). Particles which are not deflected ($y = 0$) because of the free transmission gap have the highest mean energy. All other particles have a lower mean energy and can be found at off-axis positions. Note that the slight asymmetry around zero in the angular distribution for the y-direction that is caused by the energy loss in the scatterer (visible in figure 5.4) does not produce a big enough shift of the beam position in y-direction that would be observable here.

Beams with an initial angular divergence

The analysis done so far assumed a parallel incoming beam without any angular divergence. Despite this, the system has to function with *real* beams as well. If the angular divergence of the incoming particles becomes too big the particles will not be able to pass the energy selection system. This behavior is in principle independent from the addition of a scattering material. However, since the selection of particles by adding additional scattering needs a small exit tube, the opportunity to transmit beams with a wide angular divergence through the system and collimate them later is limited. Therefore, figure 5.8 shows the dependence of the transmitted spectrum on the angular divergence of the incoming beam for test case 1. The angular distribution is assumed to be Gaussian and circular in the lateral plane (y-z-plane). First, the absolute number of

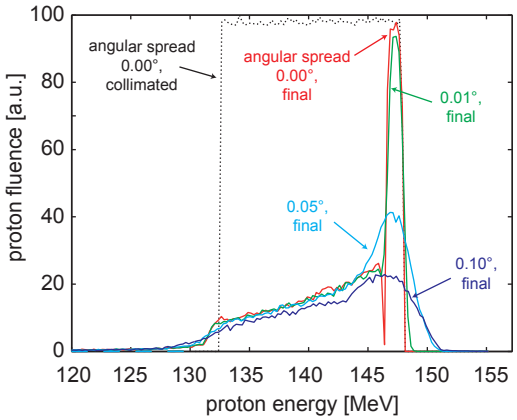

Figure 5.8: Dependence of the transmitted spectrum on the angular divergence of the incoming beam. The numbers refer to the sigma of the assumed Gaussian distribution of the angular divergence. See text for details.

transmitted particles decreases with increased angular divergence. Second, the spectral shape changes and will hence produce a different SOBP. This can be compensated for by changing the shape of the scattering material. However, the efficiency of the system would be decreased. It has to be determined if the increased efficiency caused by using modified energy spectra to produced SOBPs in one laser shot is not undone by the smaller exit tube necessary for this system. This mainly depends on the achievable initial angular divergence.

5.2.5 Discussion

It was shown that at least in theory the use of scattering material in the beam path of an energy selection system can modify the proton fluence spectrum in a way that creates more suitable depth dose curves for therapy with laser accelerated protons. As long as the produced particles do not exhibit a sharp monoenergetic spectrum, this method is an easy and inexpensive step towards making the protons ready for therapy. Especially the width of the dose falloff can be reduced which is one of the most important properties for target conformity in radiation therapy.

The scattering system has to be optimized carefully to use as many of the initial particles as possible. With regard to this a simple wedge might not be sufficient for clinical application. However, the spectral change could be demonstrated even with this simple setup. By using slices of scattering material, the system can be adjusted to various initial energy spectra. It is reasonable to assume smooth spectra which is motivated by both theory and experiments [5, 33]. Gaps in the spectrum are unlikely

but would demand for using only protons with higher or lower energy since the system cannot create protons with energies that have not been in the spectrum before. However, in the most likely cases, for each energy all protons with this specific energy can be guided along a path that contains exactly the required scattering material to make these protons contribute to the desired final energy spectrum with the required number.

One requirement of the complete energy selection system is the ability to collimate the transmitted protons into a well defined therapeutic beam that is mostly parallel to the x-axis with only a small divergence. This is a problematic point since the final divergence will be energy dependent. However, figure 5.4 shows that all transmitted protons are deflected less than approximately 0.3°. This means that the beam spot radius at a distance of 0.5 m behind the exit tube is below 2.6 mm even without any further magnetic collimation. Additionally, the divergence of the initial beam plays an important role. The results shown in subsection 5.2.3 used the idealized situation of an initially parallel beam. However, as demonstrated in subsection 5.2.4, this is more complicated in reality, although the exact properties of laser accelerated protons are still to be determined. Since different energies have to be dealt with simultaneously beam optics are not trivial and a careful consideration of these effects is important before the proposed system can be put into operation [16, 43]. Because of this beam optics problem, smaller modulation widths for the SOBP are easier to realize than wider ones. In addition to this, the wider the SOBP becomes, the more complicated it is to modify the spectrum with the scattering material. However, since high quality radiation treatments should involve intensity modulation with a certain amount of degrees of freedom, SOBPs with shorter modulation widths would be ideal to increase the efficiency of the particle usage while preserving the ability to do IMPT. In terms of the clustering mechanism introduced earlier this means that *axial* clustering (i. e. multiple SOBPs with a small modulation width) but not *full axial* clustering (i. e. one SOBP with a wide modulation width) should be done with the help of the scattering material in the energy selection system.

So far the research is purely based on Monte Carlo simulations and the practicability of this method has to be tested with a real beam. The laser systems that are presently available can produce proton energies of the order of tens of MeVs (e. g. [50]). In this energy range the method should work as well but the practical realization might be harder. This is because the scattering material would have to be much thinner than the slice thickness of 60 μm used in this work for higher energies. As mentioned before, the scattering system has to be optimized carefully. If the structures become too small the reproducibility might be a problem. In the lower clinical range of energies (about 70 MeV

for protons), the scattering material is already thick enough to allow the described setup to work. Therefore, the range of a clinical SOBP is not important regarding the potential realization of the setup.

5.3 Using the particle beam efficiently

Another possibility for advanced radiation therapy with laser accelerated particles is to use the *given* particle spectrum as efficiently as possible by deciding which tumor spots need monoenergetic beams and which can be treated by wider spectra. Since the latter cover wider axial extents this is another realization of the idea of *axial clustering*. It is shown that the contribution from each individual energy spectrum does not have to produce a flat depth dose curve to nevertheless be able to create a homogeneous dose within the tumor. If the spectrum already produces a flat depth dose curve (because it has been modified as explained above or because it has been produced by the laser in this way) the presented methods will work even better. Additionally, the problem of too many particles per shot can be reduced by laterally distributing the particles realizing *lateral clustering*. These methods and further means of adapting radiation therapy to laser accelerated particles are analyzed in this section. Again, all calculations have been performed for pure proton spectra but the concepts are applicable to carbon ions or spectra containing combinations of various particle types as well. This section is an extended version of the work published by the author [45].

5.3.1 Methods

Clustering

Clustering as used in this thesis refers to the grouping of certain dose spots of the conventional dose delivery grid into new bigger spots that can be treated with one laser shot. It can be applied in an axial or lateral direction or in a combination of both. The basic concept is explained in section 3.2.

Axial clustering: Since each individual particle energy corresponds to a certain depth in the irradiated tissue, the dose deposition of a broad energy spectrum is stretched over a wider axial length compared to monoenergetic beams. The high dose area of its depth dose curve is not limited to only one dose spot of the conventional dose delivery grid, instead, multiple spots are treated simultaneously and are therefore grouped into a so called axial cluster. Hence, broad energy spectra are associated with big axial clusters

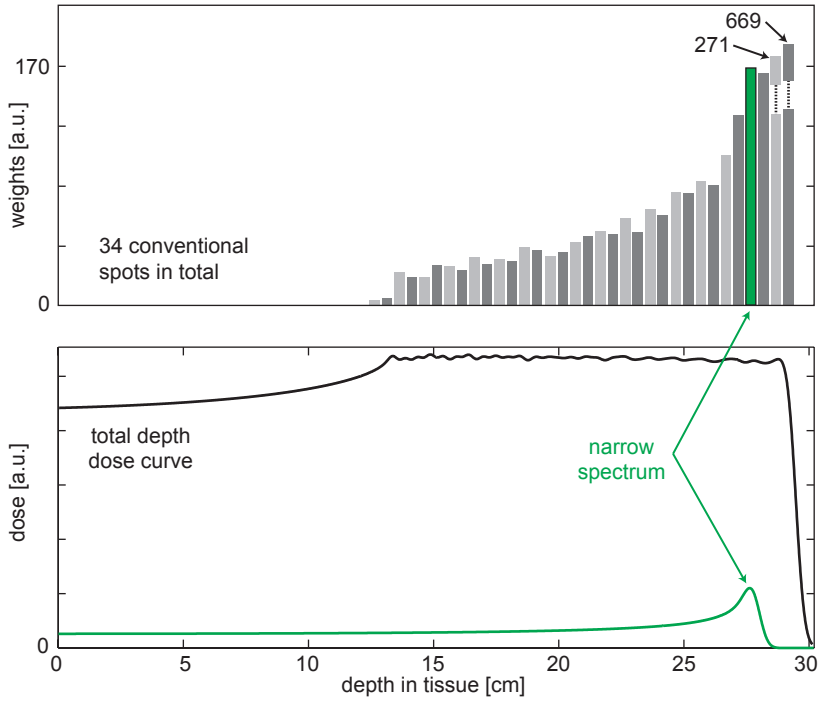

Figure 5.9: Spot weights and depth dose curve for the conventional way of building a SOBP with narrow energy spectra. Each depth is irradiated independently.

and narrow energy spectra are associated with small axial clusters (down to only one dose spot of the conventional dose delivery grid). Figure 5.9 shows an example of how conventional SOBPs are created with many independent spots that are irradiated by narrow energy spectra only; and figure 5.10 shows the same example with axial clustering that uses less independent spots and irradiates them with laser shots of *different spectral widths*. The decision of where to cluster spots (use broad spectra) and where to keep them independent (use narrow spectra) is done before the treatment plan optimization is started. Hence, when optimizing the fluences the clusters are kept constant. The cluster search algorithm can be applied independently of the form of the energy spectrum. It only needs to know the depth dose curves of all available settings of the energy transmission window in the energy selection system. Settings are given by their mean transmitted energies and the widths of the transmitted spectra. For each depth to be irradiated a subset of possible transmission window settings that reach this spot with their Bragg peak is compiled. The algorithm iterates over all target depths of each pencil beam (i. e. each ray from the source passing through the target on a pre-defined lateral grid). The aim is to cover the whole target with laser shots of maximal beam efficiency

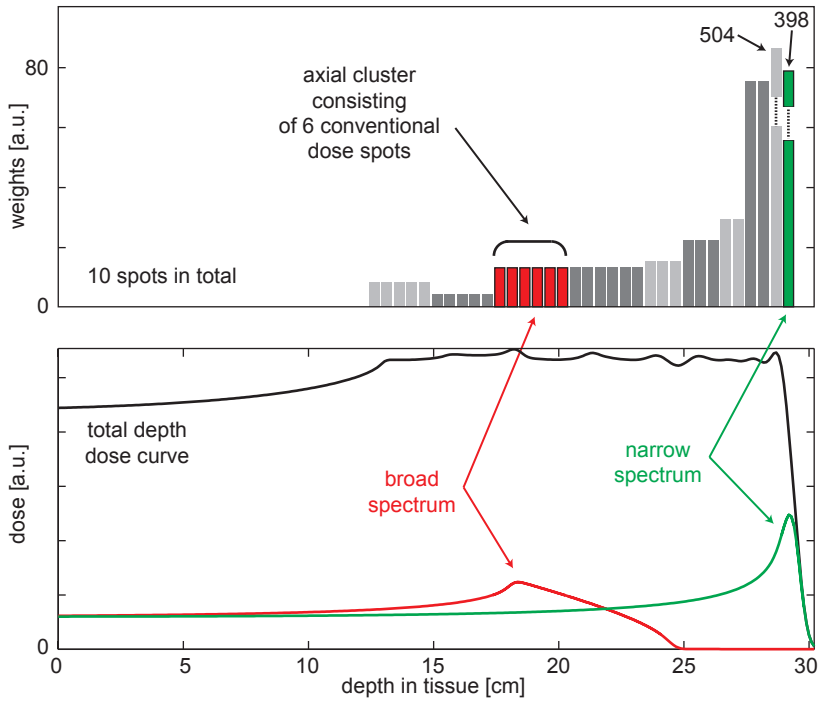

Figure 5.10: Spot weights and depth dose curve for axial clustering. Adding the depth dose curves of various wide energy spectra builds up a SOBP. For the proximal and middle parts of the target, broad energy spectra can be used (high axial particle efficiency, low number of independent dose spots). They cover several conventional dose spots that are clustered into one spot. Only the distal edge requires narrow energy spectra (sharp dose decline). In this example 34 conventional spots are replaced by 10 spots. Compare to figure 5.9.

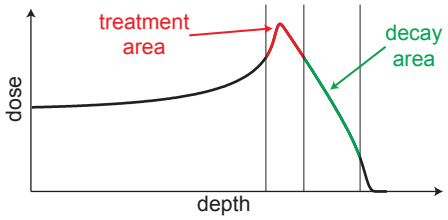

Figure 5.11: Treatment and decay area of a depth dose curve as used by the algorithm to place differently broad energy spectra within the target.

(maximal ion energy spread) with the constraint of no relevant dose behind the distal target edge.

In detail the algorithm identifies two areas within each depth dose curve (see figure 5.11). The first one is the *treatment area* where the dose is high enough for treatment (in the simulation this is set to the area with more than 80% of the maximum). If the target has a sufficient axial extension, all depth spots within the treatment area are clustered into one new spot that is irradiated with one machine setting. If the target extension is smaller than the treatment area, a smaller energy transmission window is applied (i. e. a less efficient setting). If this were the only criterion the distal dose decline would be very long. The algorithm needs another measure to ensure that this does not happen. Therefore, a second area of the depth dose curve is defined. It is called *decay area*, which is the area downstream of the treatment area where the dose is still quite high (the depth from 80% (distal) down to 20% of the maximum is used). Dose spots in this area are not clustered together with the ones in the treatment area but will primarily be irradiated by the neighboring dose spot (with an energy window of higher mean energy). The additional criterion that ensures a steep distal dose decline is that for the use of a specific transmission window the decay area has to be completely located within the target. Otherwise a narrower setting is used. For illustration, figure 5.12 shows an exemplary pencil beam where 8 spots (labeled 1 to 8) are part of the planning target volume (PTV). For this example let us assume that there is only one ion range available in the spectrum but various energy spreads around this range. The beam is shifted in depth with a range shifter. Therefore, the list of available depth dose curves (resulting from various energy spreads) is the same for every dose spot (in general each depth has its own list of possible settings). The depth dose curves can be described by the extent of the treatment area and the extent of the decay area, both lengths given in multiples of the spot spacing. For example $6+3$ means that the treatment area extends over 6 and the decay area over 3 spots. The list of possibilities for each depth shall be: $6+3$, $4+2$,

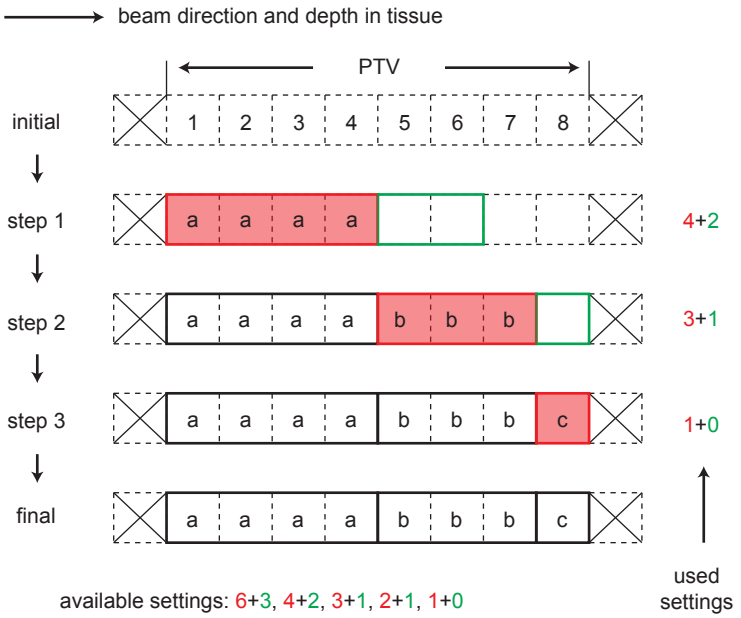

Figure 5.12: Example for the application of the axial clustering algorithm. Starting upstream, several steps (in this case 3) are used to find appropriate clusters. The scheme $x + y$ means that - in multiples of the spot spacing - the treatment area is x units and the decay area is y units wide. Only curves with both treatment and decay area within the tumor are allowed. The available settings are sorted by beam efficiency and sampled according to this sequence. See text for further details.

$3+1$, $2+1$ and $1+0$. This list is sorted by beam efficiency. Initially the 8 spots are not assigned to any cluster. In step one the first cluster is built. There are only 8 PTV spots. Since both treatment and decay area have to be within the PTV, the $6+3$ curve does not fit. The first appropriate option is the $4+2$ curve which is placed in the proximal part of the PTV. Hence, spots 1 to 4 are put into cluster 'a'. The decay area covers the following two spots, however, these are within the tumor and the dose does no harm to surrounding tissue. In the second step the next cluster is formed downstream of cluster 'a'. The most efficient transmission window setting is sought-after that can be used to irradiate spots beginning with number 5. Note that here a spot is placed in the decay area of the spot further upstream. The best choice for this spot is the $3+1$ setting, creating cluster 'b' from depths 5 to 7 with a decay area reaching to depth 8 only. Then, the last step has no other option than to use the smallest available transmission window setting producing depth dose curve $1+0$ to create the last cluster ('c') with just one member (depth 8). For the general case of different depth dose curves for each depth (no range shifter necessary) the algorithm has to apply the actual depth dose curve corresponding to the current spot. Since absolute energy spreads are used for the different transmission window settings this can result in slightly bigger clusters downstream in the beam (the range increases faster than linear with ion energy[3]). This can be seen in figure 5.10 where the first two clusters consist of 5 spots each and the third one extends over 6 spots. Here, all three clusters use the same absolute transmission window width but different mean energies.

As a consequence of the presented clustering strategy, at the proximal edge and in the middle of the target several depths can be combined into one cluster that is irradiated with a broad energy window. This reduces the number of independently irradiated dose spots and increases the axial particle efficiency. For these spots it does not matter that the decay area of broad energy spectra is quite long since there is plenty of target downstream of the spot that needs dose anyway. At the distal edge no clustering is possible and smaller settings of the energy window are used instead. For monoenergetic beams both the treatment and the decay area are very short. As a result, if only narrow energy spectra are available (conventional acceleration method) the algorithm described above will produce dose spots at the positions of a classical dose delivery grid. If the available spectrum already results in a SOBP of a certain length the algorithm recognizes the short decay length and can use the spectrum very efficiently. Therefore, the axial clustering algorithm described above can be used in addition to the mechanism to modify the energy spectra mentioned in section 5.2 (which by itself is another way of axial clustering).

Lateral clustering: Lateral clustering is useful if the number of particles per shot within a relatively narrow energy window is very high. Instead of throwing away a certain percentage of particles they can be spread over a bigger lateral area with the help of a MLC. Multiple neighboring spots in the lateral view of the conventional dose delivery grid (beam's eye view) are grouped and irradiated simultaneously. According to subsection 4.3.7, a MLC requires the use of flat fields instead of Gaussian beam spots for the dose delivery and calculation. These flat fields are composed of flat subfields constructed out of a high number of Gaussian pencil beams. However, for the sake of simplicity, all independently irradiated areas (i. e. Gaussian beam spots or flat fields) are called *spots* throughout this thesis to emphasize their meaning as degrees of freedom. Two different possibilities of lateral clustering are investigated: *prior* lateral clustering and *posterior* lateral clustering. The difference is the time within treatment planning when the clustering is performed.

Prior lateral clustering means that it is done before the treatment plan optimization. It is based on geometrical considerations only. For each iso-energy slice (i. e. for constant radiological depth), neighboring target spots on a predefined lateral grid can be clustered up to a certain cluster size. However, to enable a good treatment plan with sharp lateral gradients, points on the edge of the target should not be clustered. A parameter called *neighborhood sum* is introduced to describe to what extend a spot is an inner point. For a given target spot, each of the four direct neighbors on the grid are assigned a weight of 2 if they are also target spots. Additionally, the next four neighbors on the diagonal edges are assigned a value of 1 if they are target spots. The *neighborhood sum* is the sum of all these values and ranges from 0 to 12. An inner point has a high neighborhood sum and an edge point has a small value. A limit for this value that separates inner points that can be clustered from edge points that cannot be clustered must be chosen. For the clustering itself spot groups of limited size are searched that are as compact as possible (i. e. have a small lateral extension). Figure 5.13 shows an example where spots are only clustered if the neighborhood sum is bigger than 6. The maximal cluster size is 9. In this case the clustering leads to 15 instead of 45 independent dose spots. For prior lateral clustering the influence matrix D_{ij} is modified before the optimization starts: After the clustering algorithm has decided which spots shall be clustered, for each resulting cluster group, all matrix columns of spots that are within this group are summed up to constitute one new column.

As another approach posterior lateral clustering is performed after the optimization has been done (similar to leaf sequencing as a post-processing step in intensity modulated radiotherapy with photons). The spots are kept independent during the (first)

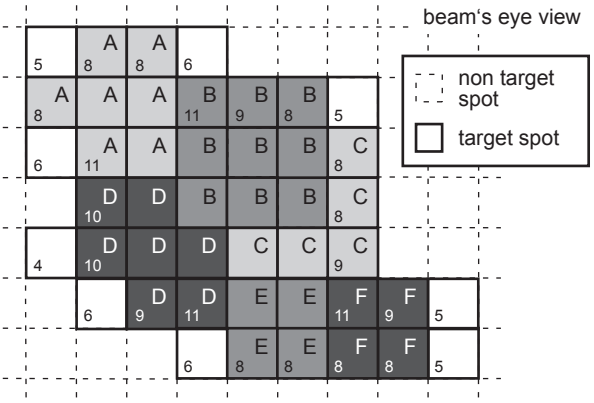

Figure 5.13: Prior lateral clustering. The numbers are the neighborhood sums and denote to what extend each target spot is an inner point (see text). They range from 0 to 12. If a spot has a value of 12 (completely inner point) the value is omitted for better readability. Clustering is performed for all points with a neighborhood sum above 6. The maximal cluster size is 9. Spots within clusters are denoted with capital letters.

optimization to allow the best possible treatment plan. This means that (at first) the influence matrix D_{ij} is not modified but contains the independent flat fields from the dose calculation. After this optimization is finished, the resulting spot weights for each energy setting are compared to each other. A modified version of a standard *k-means clustering algorithm* (for an overview see [25]) is used in combination with a neighborhood clustering algorithm to find lateral neighbors that have similar weights (which for example do not differ by more than 20%). The first requirement for clustering is that the spots are locally connected to each other. This ensures that a MLC can be used to form the cluster. The second requirement is that all spots use the same energy setting. Within each of these possible groups, the k-means algorithm then tries to identify the smallest possible number k of subgroups whose members have similar spot weights. It starts with $k = 1$ (i. e. one subgroup only) and increases k until the similarity criterion (for example at most 20% difference) is fulfilled for all members of all subgroups. The members of each of these resulting subgroups are merged into new non-overlapping dose spots (i. e. now the influence matrix is modified) and the optimization is restarted. The whole procedure is repeated several times (usually 2 cluster searches, each with a consecutive re-optimization). It turns out that posterior lateral clustering makes it easier to conserve the plan quality while increasing the beam usage efficiency. Therefore, the focus in this thesis is on the posterior technique.

However, prior and posterior lateral clustering can be combined depending on the

requirements of the individual treatment plan. Apparently it makes a difference *how much* clustering is done but not *when* it is done. As already mentioned earlier lateral clustering is an intermediate step between layer stacking and spot scanning. Various parameters control how close the result is to either of these methods: For prior lateral clustering it is the limit for the neighborhood sum that determines if a point is an inner point, and the maximal cluster size. For posterior lateral clustering it is the similarity limit that determines if two weights are similar enough to group the corresponding spots. So far it has been assumed that spot groups which are locally connected can be applied with a MLC. Unfortunately, this is not true since only *convex* lateral beam shapes can be applied for sure. Additionally, shapes which could be described as *one-dimensional-convex*[1] along at least one of the two dose delivery grid dimensions are also allowed. Since the clustering algorithm rarely produces shapes which are not possible with a MLC, not much attention has been attributed to this problem. Hence, locally connected spots are assumed to be deliverable by the system. The resulting error in the number of spots and therefore the lateral efficiency of the system is only of minor importance. The problematic cases could easily be resolved by dividing the affected groups.

Clustering in both directions: It has been described how axial and lateral clustering work in detail. In principle, both methods can be applied simultaneously to create a treatment plan. However, they are not independent from each other. The three dimensional dose spots given by axial clustering in the depth direction and lateral clustering in the lateral directions are cuboids. Lateral clustering can only be done if the energy selection system is set to the same transmission window for all participating lateral spots. In general it is not clear how to cover an arbitrary target volume with differently sized cuboids since there must be a priority concerning which clustering direction is more important. A procedure to synchronize both methods in a way that makes clustering in both directions easier has been implemented, however, this problem has not been fully solved yet. The current approach, which is built into the axial clustering algorithm, tries to look at multiple adjacent pencil beams simultaneously to increase the likelihood that neighboring pencil beams use the same energy transmission window setting in as many depths as possible. If in one pencil beam a highly efficient beam spot has been placed in a given depth, the axial cluster search in the neighboring pencil beams is not started at the upstream end of the PTV but at the depth where the efficient spot of its neigh-

[1] While this is not a mathematical definition, a shape could be said to be one-dimensional-convex if it is convex along one dimension only. In mathematical terms: M is *convex*: $x = (x_1\ x_2) \in M,\ y = (y_1\ y_2) \in M \rightarrow x + (y - x)\lambda \in M\ \forall\lambda \in [0, 1]$, M is *one-dimensional-convex* (here: along the first dimension): $x = (x_1\ z) \in M,\ y = (y_1\ z) \in M \rightarrow x + (y - x)\lambda \in M\ \forall\lambda \in [0, 1]$.

bor begins. The remaining upstream spots are processed afterwards. The implemented approach is to start the procedure with the pencil beam that has the widest PTV. This synchronization attempt causes a slightly decreased beam efficiency for axial clustering but increases the efficiency of lateral clustering.

Modification of the optimization routine

So far alternative methods of dose delivery for laser accelerated particle therapy have been analyzed. The focus of the following section is on changes to the optimization algorithm that help to minimize laser specific disadvantages. The starting point of these considerations is the usual quadratic objective function F_0 from equation 4.5 on page 59. The spot weights ω_j determine the dose and are varied to minimize F_0. For laser accelerated particle therapy the weights can be scaled to equal the required number of laser shots (e. g. $\omega_{17} = 2$ would mean that exactly 2 laser shots are necessary with the beam and dose delivery system setting called $j = 17$).

Reduce the number of shots: Since the repetition rate of the laser is certainly a limit for radiation therapy with laser accelerated particles it is desirable to keep the number of required shots as low as possible ($\min \sum_j \omega_j$). This can be achieved with several methods. The first and easiest one is to add an additional term $F_1(\omega)$ to the usual objective function $F_0(\omega)$ from equation 4.5.

$$F(\omega) = F_0(\omega) + \underbrace{p \sum_j \omega_j}_{=:\, F_1(\omega)} \tag{5.1}$$

The penalty factor p can be chosen automatically by doing an intermediate optimization of $F_0(\omega)$ first. The resulting (fixed) weights shall be called ω'. p is then set such that $F_1(\omega')$ has a certain magnitude (0.1% are used) compared to $F_0(\omega')$.

The second method is the use of hard constraints for the minimization of $F_0(\omega)$. This requires a rough estimate of how many shots one needs and how many are allowed. The algorithm will guarantee that not more than a given number N of shots are used but will not try to reduce it further. Within the scheme of Mosek, this is achieved by the

following additional constraint (assuming this is the first constraint it is $m = s = 1$):

$$\begin{aligned}\left(\underline{Q}_s\right)_{jk} &= 0\\ \left(\vec{c}_s\right)_j &= 1\\ l_s &= 0\\ u_s &= N\end{aligned}$$

Last but not least there is a third possibility. In prioritized optimization (compare to [59]) the first step is the minimization of $F^{(1)}(\omega) = F_0(\omega)$. Based on this result certain hard constraints can be deduced for a second optimization step that minimizes the number of shots as the only criterion. Hence, the second step is given by minimizing the objective function $F^{(2)}(\omega)$ that reads:

$$F^{(2)}(\omega) = \sum_j \omega_j$$

A possible constraint for this second step is that the value of $F^{(1)}(\omega)$ does not increase above a certain level compared to the first step. In the following the focus will be on the method introduced first (which uses the additional term $F_1(\omega)$) since it proved to be most practicable.

Reduce the number of spots: To reduce treatment time not only the number of shots but also the number of spots is relevant. When using a MLC to shape the dose laterally, the number of spots must not be much higher than 1000 (if the MLC needs 1 s to align, this would already mean a time of almost 17 min). Even if no MLC is used, the reduction of dose spots will certainly save time. This problem is already approached with clustering of dose spots which reduces the number of independent spots. However, the number can be decreased further by using repeated runs of the optimization. After one run the spots that do not contribute to the integral target dose to more than a certain level compared to the average target dose contribution for all spots are removed completely. Afterwards, the optimization is started again. Spots are removed twice (with a subsequent re-optimization after each removal) and the limit to remove the spots is set to 10% of the average spot contribution to the target. This procedure can remove many redundant dose spots (degrees of freedom) without changing the quality of the treatment plan (see below).

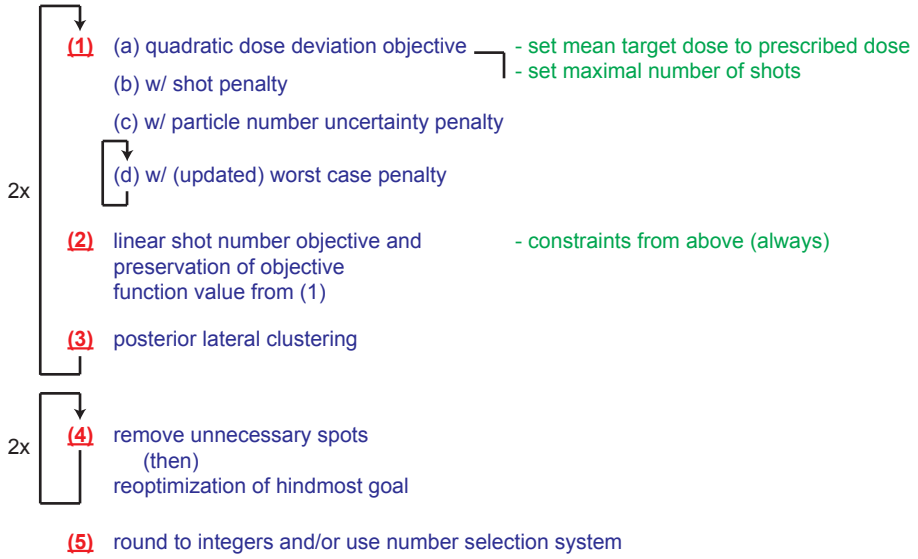

Figure 5.14: The full optimization routine for laser accelerated particles. See text for details.

Shot numbers are integers: The number of laser shots that can be delivered is a natural number. Since integer programming is more complicated and much slower than optimization with real numbers the number of shots is treated as a real number for each optimization run. Nevertheless the quantization of the number of shots is included into the system as much as possible. After the optimization has been performed each spot weight is analyzed. Some can be rounded towards the nearest integer without changing the resulting dose distribution very much (if the relative change of the weight is below 10%). Some other spots can be rounded to zero (below 10^{-3} in the cases that have been analyzed[2]). All others cannot be rounded without changing the plan. The fluence selection system has to be used for the last shot of these spots. As mentioned, this decreases the lateral particle efficiency. At this point integer programming could provide a better solution in some special cases. However, the problematic cases are the ones with only few (or even just one) shots per spot. For these the problem of too many particles per shot persists since the fluence selection system has to be applied eventually.

The full optimization routine for laser accelerated particles: Figure 5.14 shows the full optimization scheme that has been used. In step (1.a) the quadratic dose deviation objective is optimized according to equation 4.5. This is the only mandatory step. During this step optional constraints (fixation of the mean target dose to the prescribed

[2]This threshold is only possible if the number of particles per shot is not too high.

dose, fixation of the maximal number of shots) can be activated. If the number of shots shall be reduced according to equation 5.1 step (1.b) can be applied afterwards. Steps (1.c) and (1.d) are not used here but will be explained in chapter 6 that deals with uncertainties in radiation therapy with laser accelerated particles. If required, in step (2) the number of particles can be reduced with the method of prioritized optimization. If posterior lateral clustering is required, it can be performed in step (3). Afterwards, the optimization has to be restarted from step (1.a). The reduction of the number of spots is done in step (4) and finally, in step (5), the incorporation of shot numbers as integers is processed.

The used patient case example

In the following treatment planning studies that apply the proposed methods are presented. They show that laser accelerated particle plans with increased efficiency compared to the 'classical' methods can be created without sacrificing the plan quality. The impact on treatment planning for each of these methods is described. As an illustration a head and neck case containing a tumor close to the left parotid gland is used. It is treated with two coplanar intensity modulated proton beams. Both the lateral dose spot spacing (in the isocenter) and the axial dose spot spacing (radiological depth) are 5 mm before clustering. This forms the classical dose delivery grid. Because of the dose quantization the plan has to be calculated based on the dose per fraction (2 Gy prescribed dose) and not for the whole course. The most important volumes of interest (VOIs) are the *ipsilateral parotid gland* and the PTV (volume: 285 cm^3). The third VOI (called *PTV shell*) is a volume of 1 cm thickness that surrounds the PTV. The lower the dose in this volume, the steeper are the dose gradients between PTV and normal tissue. The PTV shell is used for both optimization and visualization of these dose gradients around the PTV. Figure 5.15 pictures a transversal slice and figure 5.16 a coronal and a sagittal slice of this patient geometry showing the PTV, the PTV shell and the ipsilateral parotid gland together with a dose distribution for a scenario analyzed below.

5.3.2 Results

Clustering

Axial Clustering: The first example is a study where the laser acceleration device produces energy spectra of great width. Figure 5.17 shows two of these wide energy spectra of different mean energy with 10^8 particles per shot each. Again, these spectra are not from measurements but they are similar to what could be available in the future. A

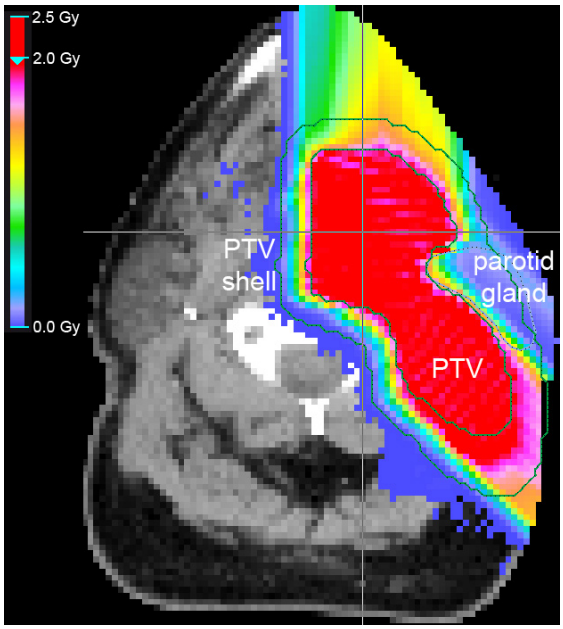

Figure 5.15: Transversal slice of the patient geometry. The figure shows one dose distribution of the axial clustering study discussed below (plan called *classical* in figure 5.18 on page 89).

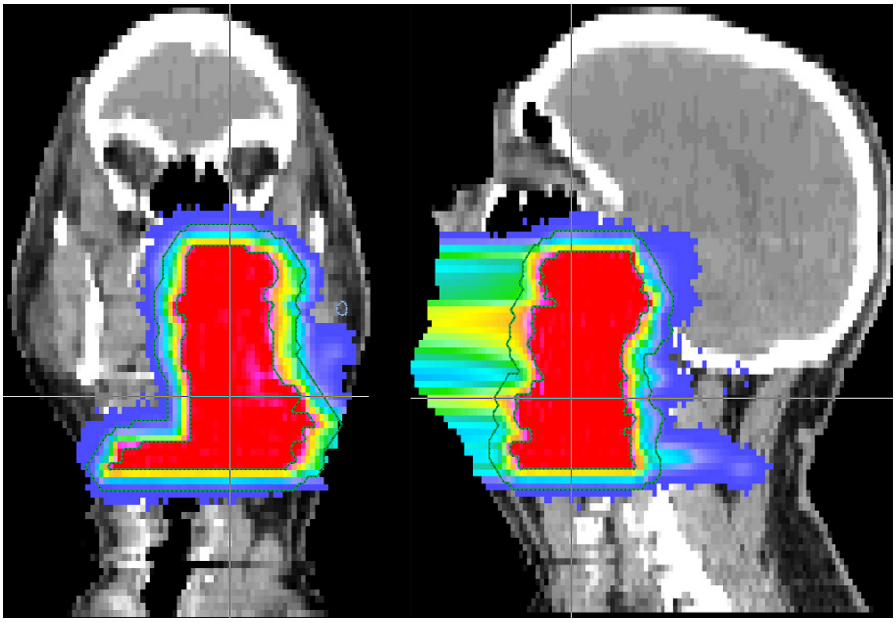

Figure 5.16: Coronal (left) and sagittal (right) slice of the patient geometry. The figure shows one dose distribution of the axial clustering study discussed below (plan called *classical* in figure 5.18 on page 89). The color coding is equivalent to the one in figure 5.15.

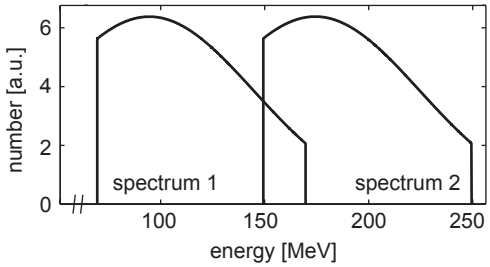

Figure 5.17: The used energy spectrum to illustrate some of the advanced treatment planning studies for a head and neck case.

broad beam from spectrum 1 with a fluence of 10^8 particles per spot (0.25 cm^2) results in a peak dose of 0.68 Gy at a depth of 4.1 cm. For an only 20 MeV wide part around the maximum of the spectrum this value is reduced to 0.32 Gy at a depth of 5.8 cm. In figure 5.18 a patient case which assumes that these two spectra can be produced on demand is simulated. Three plans are calculated: The first one is a standard spot scanning plan where the energy selection system cuts monoenergetic beams (1 MeV wide) out of the total spectrum ('classical': no clustering, no MLC). It uses 3665 spots and 68064 shots. A total energy of 129 J has to be blocked within the energy selection system. The two advanced plans use the spot scanning technique with axial clustering (no lateral clustering, no MLC) and differ in the number of available widths for the energy transmission window. One uses 10 equispaced steps from 1 to 10 MeV and the other uses 20 equispaced steps from 1 to 20 MeV. The modification of the objective function (additive term) to decrease the number of shots is turned on and the removal of unnecessary dose spots is activated as well. These plans only need 1586 (1298) spots (plan with 10 and 20 widths, respectively) which is 43% (35%) compared to the classical plan. The shot number is 8014 (5538) or 12% (8%) of the classical plan and the blocked energy 15 (10) J, which is 11% (7%) of the classical plan. Thus, the efficiency of the system regarding time and secondary radiation is much higher, approximately by a factor of 9 (14). For further information, figure 5.15 on page 87 shows a transversal slice of the three-dimensional dose distribution of the classical case and figure 5.19 the corresponding distributions of the two advanced cases. In the dose volume histograms (DVHs)[3] the ipsilateral parotid gland and the PTV do not show any relevant difference. There is slightly more dose in the PTV shell for the advanced cases. There are two main

[3] A Dose volume histogram (DVH) plots the volume (in percent) of a selected tissue that receives a certain dose or more. It is therefore a plot of volume against dose. Target tissues should have curves which are located in the upper right corner, and normal tissues should have curves which are located in the lower left corner of the plot.

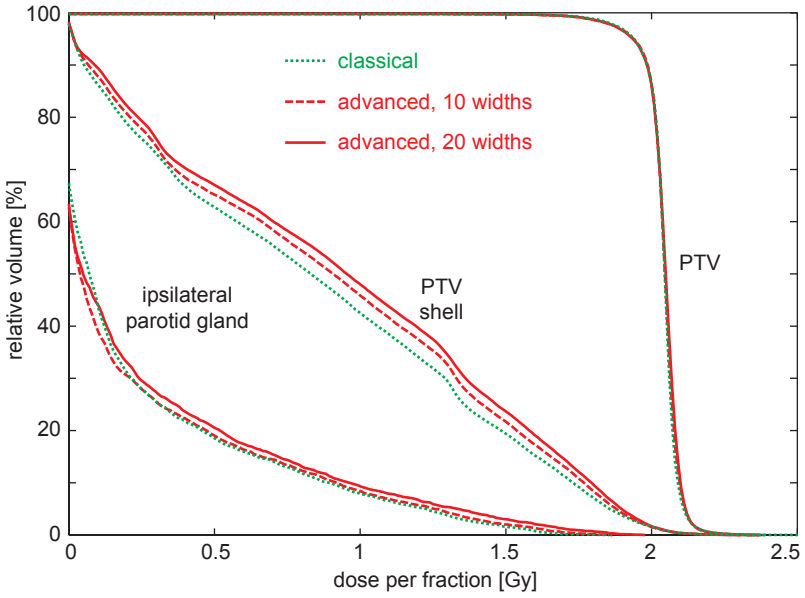

Figure 5.18: Axial clustering for a head and neck case. The energy spectra from figure 5.17 are used to produce the classical plan (spot scanning, no clustering, energy transmission window set to 1 MeV in width, no modification of optimization) and the advanced plans (axial clustering, 10 (20) energy transmission window settings from 1 to 10 (20) MeV in width, modified optimization). The advanced plans need approximately 43% (35%) of the spots and 12% (8%) of the shots while producing 11% (7%) of the amount of secondary radiation compared to the classical plan. Transversal slices of the dose distributions can be seen in figures 5.15 and 5.19.

reasons for the increase in dose. First, there are fewer degrees of freedom and second, the algorithm for placing beams with differently sized energy spectra within the PTV allows spot combinations that have 20% dose behind the distal edge of the PTV (beyond the decay area, see above). This setting could be changed; however, at some point there needs to be a compromise between plan quality and treatment practicability.

The case discussed above uses two beams that are optimized simultaneously. The IMPT technique is favorable for axial clustering since in this case not all PTV spots along a pencil beam have to be irradiated to the same extent to form a flat depth dose curve within the tumor. The distal spots of one pencil beam that cannot be merged very efficiently because of the long decay areas of bigger clusters might easily be clustered when using another beam direction. Therefore, the optimization can use the direction that is most efficient. However, the clustering technique also works when applying single beam optimization. Treatment plans with the same settings as above are created that

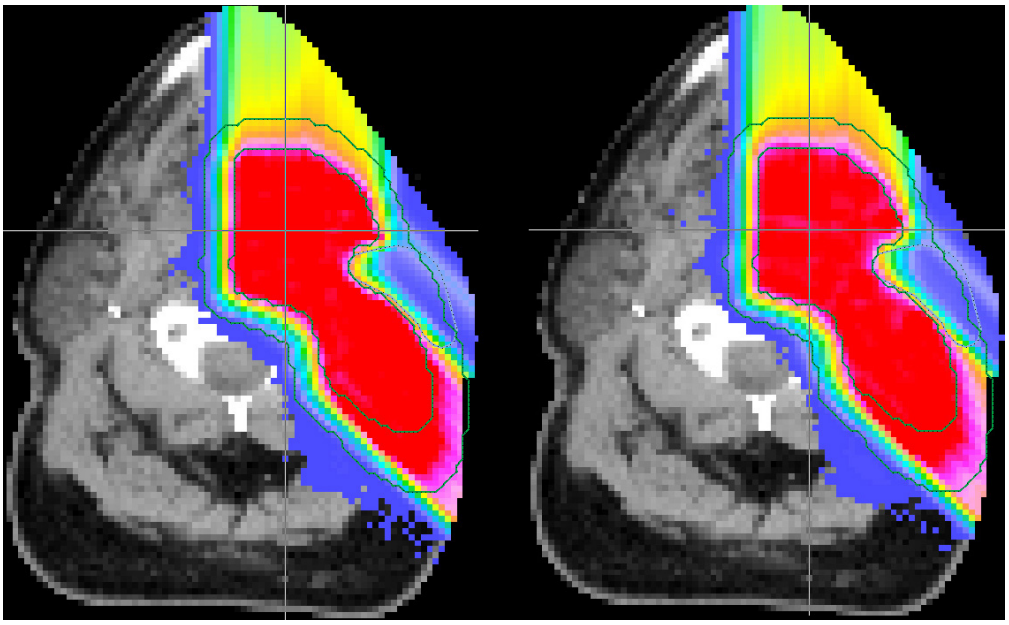

Figure 5.19: Transversal slices of the dose distributions for axial clustering. The figure illustrates two distributions whose DVHs can be seen in figure 5.18: The plan called *advanced, 10 widths* is shown on the left, the plan called *advanced, 20 widths* is shown on the right. The remaining one called *classical* is pictured in figure 5.15. There are no significant differences between these three dose distributions. The color coding is equivalent to the one in figure 5.15.

use only one beam instead of two. The DVHs for the classical and the advanced plan (using 20 different energy widths from 1 to 20 MeV) are again comparable (not shown). Here, the spot number could be reduced to 36% and the shot number to 11% compared to the classical plan. The axially blocked energy is lowered to 13% which is of course not as efficient as the 7% found for the plan with two beams. Figure 5.10 shown above is obtained by irradiating a water phantom with a SOBP. The pencil beams from the patient plan using just one beam are equivalent to this. There is a certain amount of fluence to dose spots at the distal edge that cannot be clustered. In contrast to this the plan with multiple beams avoids dose to the distal edge and irradiates this area from another direction. This is due to the modifications to the objective function which try to minimize the number of shots and therefore increase the usage of highly efficient dose spots. However, this is achieved by using different spot weights only; the cluster pattern itself is not changed since it is performed for each beam independently.

Lateral clustering: Figure 5.20 shows the application of lateral clustering in the same patient case. A broad energy spectrum is assumed in combination with a narrow setting of the energy selection system which transmits 6×10^8 monoenergetic particles per shot for every required energy. For the analysis of lateral clustering this is equivalent to a (tunable) monoenergetic beam. Since more particles per energy than needed are available in every shot some of them have to be removed by the fluence selection system. For example, a broad beam with 200 MeV and a fluence of 6×10^8 particles per spot (0.25 cm^2) would produce a dose of 9 Gy at a depth of 25.8 cm.

The first plan uses a 'classical' spot scanning technique in which the number of particles is reduced with an additional beam spreading foil and a subsequent circular collimator of fixed size. It needs 3422 spots and the same number of shots. A total energy of 35 J has to be removed from the beam within the fluence selection system[4]. The two advanced plans which employ a MLC instead of a simple collimator apply posterior lateral clustering of neighbors which differ up to 20% (80%) in their weights. As already mentioned, this clustering is done twice, leading to a total number of three executions of the optimization routine for each plan. Additionally, the number of spots and shots is reduced as described above. These plans get along with 2740 (1873) spots, which is 80% (55%) compared to the classical plan, and 2741 (1888) shots (80% (55%)). The removed energy amounts to 30 (20) J, or 84% (58%) of the classical plan. In this comparison some differences can be seen in the DVHs. There is less dose in the PTV shell for

[4]Please note the limitations of the algorithm to calculate the lateral particle efficiency of systems with simple collimators and MLCs which are described in section 4.5.

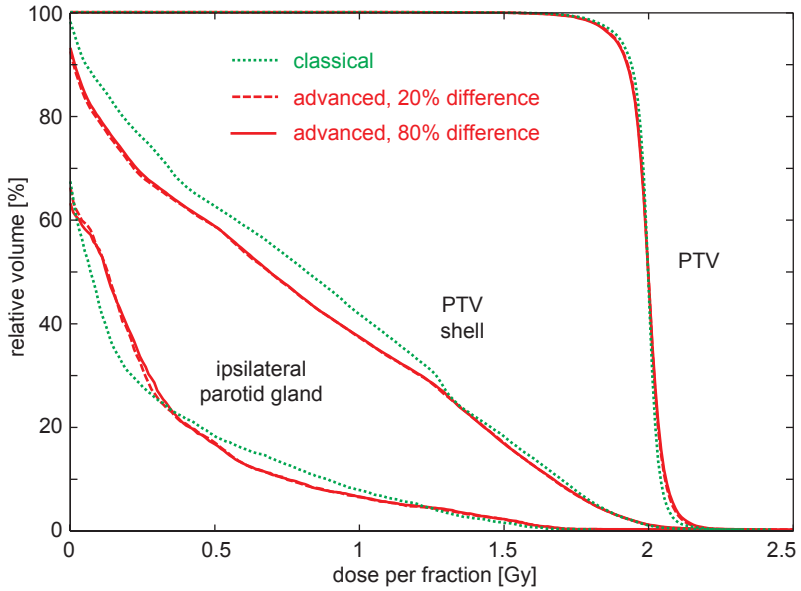

Figure 5.20: Lateral clustering for a head and neck case. Comparison of classical plan (spot scanning, no clustering, no modification of optimization) with two advanced plans (with MLC, modified optimization) using posterior lateral clustering of neighbors that differ up to 20% (80%) in weight. The advanced plans need approximately 80% (55%) of the spots and 80% (55%) of the shots while producing 84% (58%) of the amount of secondary radiation compared to the classical plan.

the advanced plans. This is due to less effects originating from the rounding of spot weights to integers. Instead of rounding, the fluence selection system could be used in more cases, however, this would further decrease the efficiency. The low dose part of the ipsilateral parotid glands receives more dose when using a MLC. As an illustration figure 5.21 shows the cluster pattern of a typical iso-energy slice of the advanced plan where neighboring spots which differ up to 80% are merged.

Clustering in both directions: Last but not least a case with a broad energy spectrum *and* many particles per energy bin is presented. The spectrum is the one from the axial case (see figure 5.17) but now with a total number of 10^9 particles per shot. Figure 5.22 compares a 'classical' plan (no clustering, no modification of optimization) with an advanced plan which uses both axial and (posterior) lateral clustering simultaneously (modified optimization). To increase the flexibility for simultaneous axial and lateral clustering, only three different widths of the energy transmission window are allowed (1, 5, and 10 MeV). Two steps of posterior lateral clustering are performed for neighboring

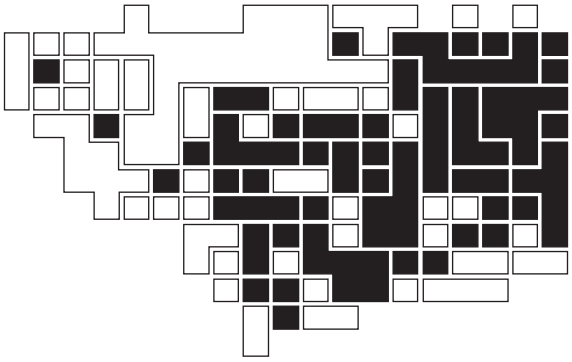

Figure 5.21: Typical iso-energy slice of the advanced treatment plan (called *80% difference* in figure 5.20) illustrating lateral clustering. There are 175 spots in total. 74 of them are independent, the remaining spots are clustered into 30 different groups. Filled boxes are irradiated with a certain dose, empty boxes denote spots whose weights have been set to zero within the optimization. The great amount of spots with zero dose is caused by the modifications to the objective function which try to minimize the number of spots.

spots whose weights differ by up to 20%. The advanced plan uses only 50% of the spots and 31% of the shots while the energy blocked in the energy selection system is reduced to 31%. On the other hand, the energy blocked in the fluence selection system increased to 997% compared to the classical plan. This shows that in some cases axial clustering can *decrease* the lateral efficiency. However, the *total* amount of energy blocked in the energy and fluence selection systems (and hence the amount of secondary radiation) is reduced to 33%. Nevertheless, the total efficiency cannot be increased as much as in the case of axial clustering only.

Modification of the optimization routine

So far the focus of the analysis has been on clustering techniques. In the following the modification of the optimization is illustrated independently from clustering. As described above spots are removed if they do not contribute high enough to the PTV dose and then the optimization is restarted. Furthermore, an additional term in the objective function reduces the total number of shots. Figures 5.23 and 5.24 show that the reduction of both spots and shots can be done with almost no changes in the treatment plan quality. Axial and lateral particle efficiency is increased. In the plan where both methods are applied, the energy deposition in the energy selection system is only 52% and in the fluence selection system 80% compared to the standard case without modification

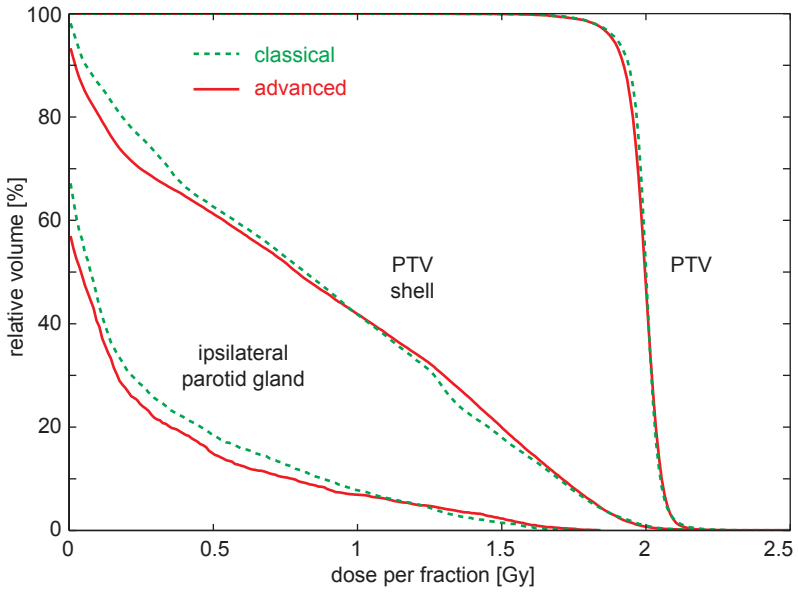

Figure 5.22: Axial and lateral clustering for a head and neck case. Comparison of a classical plan using spot scanning (no clustering, no objective function modification) with an advanced plan using a MLC (axial and lateral clustering, modified objective function). The advanced plan needs 50% of the spots and 31% of the shots while producing 31% of the amount of secondary radiation in the energy selection system and 997% in the fluence selection system compared to the classical plan. Since the number of laterally removed particles is very low compared to the axially removed ones, the total amount of secondary radiation is reduced to 33%.

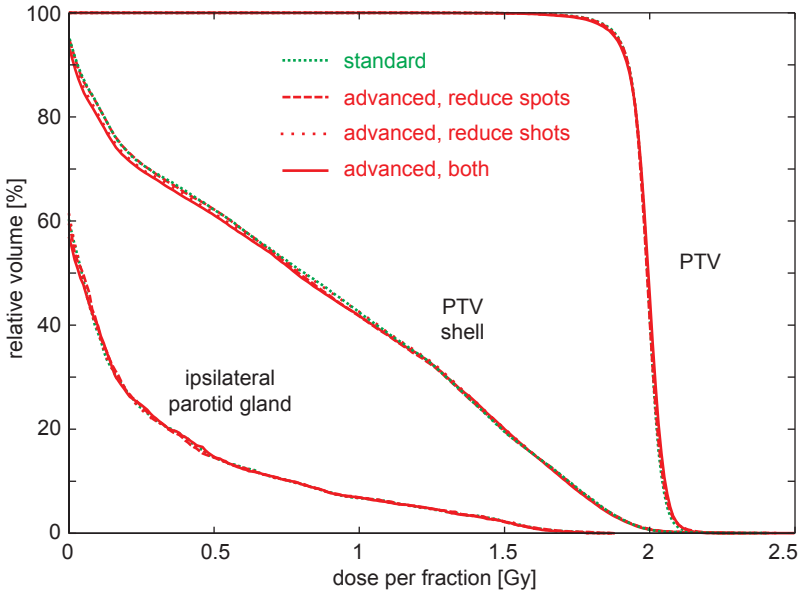

Figure 5.23: Modification of the optimization for a head and neck case. All plans were clustered axially and laterally. They only differ in the additional methods to reduce the number of spots and shots. Standard: 2435 spots with non-zero weight, 4414 shots; advanced, reduce spots: 1874 non-zero spots (77%), 3958 shots; advanced, reduce shots: 2349 non-zero spots, 2907 shots (66%); advanced, both: 1796 non-zero spots (74%), 2365 shots (54%). Coronal slices of two of the dose distributions can be seen in figures 5.24.

of the optimization. Here all plans, including the standard case, use axial and lateral clustering.

5.3.3 Discussion

The developed simulation tool enables the quantitative analysis of treatment planning for various energy spectra and beam quantizations. Based on this it can be argued that broad energy spectra can be used in the therapeutic energy range (e. g. between 70 and 250 MeV for protons) in conjunction with an energy selection system if secondary radiation from blocked particles can be shielded sufficiently. Additionally, the number of particles per energy should not change very much within this range (not more than one order of magnitude) to be able to perform the treatment with high efficiency for all required target depths. Given this, with axial clustering a high number of shots with energy spectra of up to about 20 MeV in width (corresponding to beams with up to 10-20% energy spread) can be placed within large parts of the target. Of course,

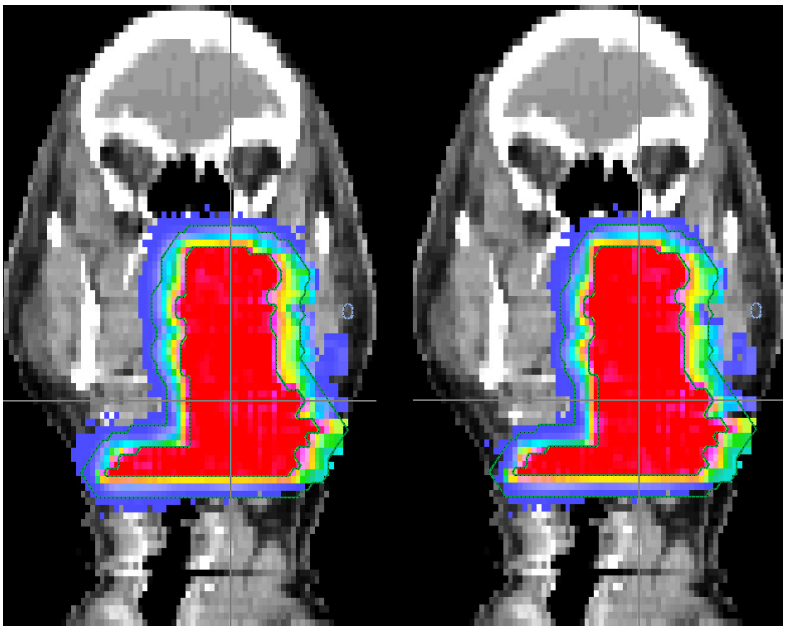

Figure 5.24: Coronal slices of the dose distributions for the study illustrating the modification of the objective function. The figure illustrates two dose distributions whose DVHs can be seen in figure 5.23: The plan called *standard* is shown on the left, the plan called *advanced, both* is shown on the right. There are no significant differences between these two dose distributions. The color coding is equivalent to the one in figure 5.15.

this strongly depends on the depth and extension of the target volume. This can be compared to an earlier publication in this field [58].

Regarding the particle number per energy, lateral clustering can increase the efficiency of the system by a certain amount but is not as efficient as axial clustering since the flexibility of intensity modulation is lost when too much clustering is applied. Results with prior lateral clustering are not presented because posterior lateral clustering leads to better results in most of the IMPT cases studied. Prior clustering should provide better results with multiple beams that each deliver a uniform dose. This is because the geometric considerations that lead to the clustering match the boundaries of the beam in this case. Lateral clustering applies concepts of aperture-based optimization as in photon IMRT (see [49]) and can be classified according to the two subfields of this technique. Whereas prior lateral clustering is purely contour-based (since it is done before the optimization starts), posterior lateral clustering uses basic ideas from direct aperture optimization (since the clusters are changed within (or at least after) the optimization). A full direct aperture optimization approach would certainly yield the best results. It must be pointed out that lateral clustering in general is only of advantage for a limited range of particle numbers per shot (approximately 10^7 to 10^9 if monoenergetic). Below this range no particles need to be blocked and above this range the total number of particles that have to be blocked is so high that even extreme lateral clustering methods would not change the relative number of blocked particles very much. To further increase the efficiency of the system a hybrid dose delivery method could be used. Lateral dose spots that are not clustered can be applied with a circular collimator and the clustered ones with a MLC. This avoids the loss of particles when cutting small rectangular fields out of a circular beam.

If the total number of particles in the whole spectrum (e. g. between 70 and 250 MeV, with not too much variation in fluence (see above)) is around 10^8 a repetition rate of 10 Hz might be enough. However, if the particle number is below this, higher repetition rates are required. Further developments in the field of laser plasma acceleration have to show what kind of energy spectra and particle numbers are feasible before the exact specifications for a laser-based particle therapy unit can be made.

The calculations presented above show that laser-based acceleration devices for radiation therapy with protons and ions have to fulfill certain conditions regarding the energy spectrum, the repetition rate and the number of particles per shot. However, it is not necessary to reproduce the same beam properties as delivered by classical accelerators (e. g. a very sharp energy spectrum and a quasi-continuous beam). Treatment can also be performed under different conditions and methods to increase the efficiency of the

dose delivery system for broad energy spectra and high numbers of particles per shot have been proposed. Axial clustering utilizes different energies simultaneously and still covers the target with a homogeneous dose. Lateral clustering tries to use as many of the available particles per shot as possible by spreading the beam in the lateral direction and shaping the beam with the help of a MLC. Both of these methods can potentially reduce the treatment time and the amount of secondary radiation that has to be shielded. Additionally, changing the optimization routines in treatment planning can reduce both the number of spots and shots that are necessary to provide a good treatment plan by eliminating some unnecessary degrees of freedom. These measures and considerations can potentially simplify radiation therapy with laser accelerated particles and its clinical implementation.

5.4 Extended possibilities with the 'advanced' methods

Figure 2.11 has been shown to illustrate that not all possible combinations of the properties of a future laser setup can lead to a working system for radiation therapy. However, the generation of SOBPs with one laser shot (section 5.2) and the advanced treatment planning methods mentioned above (section 5.3) are meant to minimize problems due to these limitations and to perform laser-based particle therapy as effectively as possible. Figure 5.25 shows the same table as above but now includes the advanced methods that can on the one hand make cases that already worked with classical planning and delivery more efficient (labeled *advanced treatment beneficial*) and on the other hand make some other cases possible at all (labeled *advanced treatment necessary*). For the last group it has to be pointed out that the methods do not provide a *general* solution to the problems with laser accelerated particles. Narrow energy spectra, high repetition rates and a (relatively) low number of particles per laser shot remain advantageous for radiation therapy. However, the proposed methods reduce the need to have the perfect laser setup (which might not be possible). Therefore, the methods can take the system into a region where it is possible to use it for radiation therapy because shielding and treatment time requirements remain feasible.

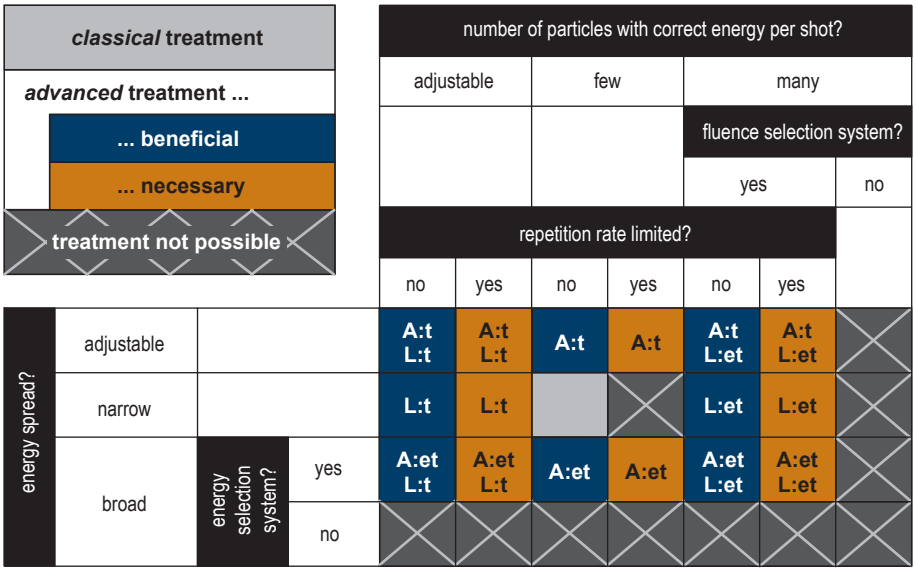

Figure 5.25: Overview of different cases for the properties of a particle beam produced by laser acceleration and the possible application of 'advanced' methods in dose delivery and treatment planning. The applicable methods are axial (A) and lateral (L) clustering. The generation of SOBPs with one laser shot can be seen as a modified version of axial clustering. Additional changes to the objective function can be applied but are not mentioned here. The reasons for using clustering are an increase in the axial and/or lateral particle efficiency (e) and a reduction in treatment time (t). Compare to figure 2.11.

6 Uncertainties in radiation therapy with laser accelerated particles

There are various uncertainties associated with radiation treatment in general [35, 28] and with particle treatment specifically [30, 56]. In addition to this, laser accelerated particle therapy has uncertainties itself. This is partly caused by the much shorter beamline compared to conventional accelerators which does not contain many beam optic elements and hence does not provide many inherent security components. For example, in a synchrotron, particles with wrong energies will not stay inside the accelerator ring because the magnets only function for one specific energy. Therefore, in a conventional accelerator the energy of the particles is constant with a very small uncertainty and only their number has to be monitored. In contrast to this, for laser-driven accelerators, the number of particles per energy bin has to be measured. Additionally, the particle beam cannot be switched off within one laser shot: either the whole amount of particles of one shot or no particle at all can be applied. Hence, as mentioned earlier, the focus of this chapter is on uncertainties in the energy spectrum of the laser accelerated particles, more precisely on the number of particles per energy bin.

6.1 Classification of uncertainties

6.1.1 Number or distribution uncertainty

The energy selection system should ensure that the minimal and the maximal transmitted energies are fixed. However, the alignment of the beam blockers is subject to uncertainties as well. Nevertheless, in the following, the values for the minimal and the maximal transmitted energies are assumed to be free of any uncertainty. Only the total number of transmitted particles and their distribution over the window of transmitted energies is subject to uncertainties. Let $f_0(E)$ be the *anticipated energy spectrum*, i. e. the spectrum that will be transmitted if the system works under perfect conditions, and let $N_0 = \int_{E_{\min}}^{E_{\max}} f_0(E)\ \mathrm{d}E$ be the anticipated number of particles in the transmitted energy range $[E_{\min}; E_{\max}]$. Then, possible uncertainties can be described by equation

set 6.1:

$$\begin{aligned} \text{number uncertainty:} \quad & f_1(E) = \alpha \; f_0(E) \\ \text{distribution uncertainty:} \quad & f_2(E) = g(E) \; f_0(E) \\ \text{general uncertainty:} \quad & f_3(E) = \alpha \; g(E) \; f_0(E) \\ \text{with:} \quad \alpha \in [0, \infty), \quad & g(E) \geq 0 \text{ such that } \int_{E_{\min}}^{E_{\max}} g(E) \; f_0(E) \; \mathrm{d}E = N_0 \end{aligned} \tag{6.1}$$

The *number uncertainty* scales the *total* particle number by a certain amount and therefore scales the dose over the full depth dose curve as well. In contrast to this, the *distribution uncertainty* redistributes a fixed total number of particles over the window of transmitted energies and therefore changes the form of the depth dose curve. The number uncertainty and the distribution uncertainty can be analyzed separately. While the former one is given by the scaling parameter α, there are arbitrarily many ways to construct the latter one. Two possibilities, which are described by their corresponding functions $g^{(\mathrm{a})}(E)$ and $g^{(\mathrm{b})}(E)$, are regarded here:

$$\begin{aligned} g^{(\mathrm{a})}(E) &= c^{(\mathrm{a})} \cdot \left(1 + \beta^{(\mathrm{a})} \cdot \frac{2E - E_{\max} - E_{\min}}{E_{\max} - E_{\min}}\right) \\ g^{(\mathrm{b})}(E) &= c^{(\mathrm{b})} \cdot \left(1 + \beta^{(\mathrm{b})} \cdot \sin\left(-\frac{\pi}{2} + 2\pi \frac{E - E_{\min}}{E_{\max} - E_{\min}}\right)\right) \end{aligned} \tag{6.2}$$

$g^{(\mathrm{a})}(E)$ describes a modification with a *linear ramp* and $g^{(\mathrm{b})}(E)$ a modification with a *periodic oscillation*. The parameters $\beta^{(\mathrm{a/b})} \in [-1; 1]$ set the magnitude of the modification ($\beta^{(\mathrm{a/b})} = 0$ means no modification) and the constants $c^{(\mathrm{a/b})}$ are chosen such that the number of particles is conserved (depending on $\beta^{(\mathrm{a/b})}$).

Figure 6.1 shows the effect of the distribution uncertainties (i. e. $\alpha = 1$) onto the fluence and the depth dose curve. Compared to the anticipated curve there are changes in the depth dose curves, however, they are not as big as the spectral changes might suggest. This is because the minimal and maximal energies are not changed and the total number of particles is preserved. Especially the entrance dose and the maximal particle range is not altered. Note that this is despite the fact that the width of transmitted energies is 40 MeV and hence is even higher than the maximally used 20 MeV of previous chapters.

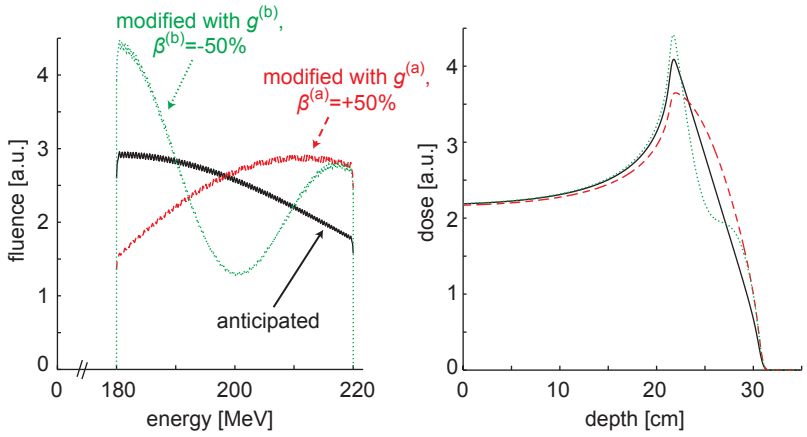

Figure 6.1: Modification of the spectral shape of the energy spectrum (left) while preserving the total number of particles (i. e. $\alpha = 1$) and the effect on the depth dose curve (right). See text for details.

6.1.2 Systematic or statistical uncertainty

Each uncertainty can be grouped into two different cases: They can be either *systematic* or *statistical*. Regarding the spectral uncertainties of laser accelerated particles the first one - the *systematic* uncertainty - means that it persists over a long time period (maybe of the order of days, maybe of the order of the time that is necessary to treat one patient). This would cause a high number of shots to have the same deviation from the anticipated spectrum. The second one - the *statistical* uncertainty - means that the fluctuations are changing on a shot-to-shot basis. Additionally, the deviations in the individual shots are statistically independent from each other.

6.2 One-dimensional considerations

Before analyzing uncertainties in patient plans its influence on SOBPs is examined. A plan with a PTV between the depth of 15 and 20 cm is prepared. This area is treated with a parallel beam using one energy spectrum of a width of 20 MeV. The beam is range-shifted to 7 different depths[1]. The amount of particles per shot is set to a number such that for each of the 7 spots only 1 or 2 shots are needed, i. e. the fluence selection system has to be used extensively. This ensures that possible beam quantization effects are emphasized. The spot weights are optimized assuming no uncertainty. Then, various uncertainties are activated and the resulting depth dose curves are illustrated together

[1]The resulting wide distal dose decline is not important for this analysis.

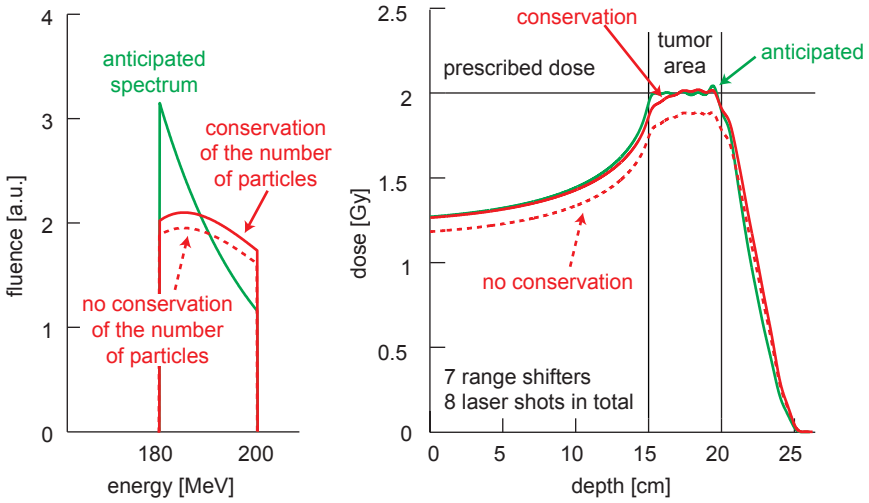

Figure 6.2: Systematic energy spectrum uncertainties (left) and their influence on SOBPs (right). See text for details.

with the anticipated curve. All modified spectra are subject to uncertainties described by the scaling parameter α and the function $g^{(\mathrm{a})}(E)$ (linear ramp) from equation sets 6.1 and 6.2.

6.2.1 Systematic uncertainties

Figure 6.2 shows the influence of systematic uncertainties which persist over the whole treatment delivery. It compares the anticipated result with the results produced by two spectra that are subject to uncertainties. The first modified spectrum preserves the total number of particles, i. e. the spectral modification is a distribution uncertainty ($\alpha = 1$, $g^{(\mathrm{a})}(E) \neq 1$). Here, the SOBP dose is close to the anticipated one. In contrast to this, the second modified spectrum does not preserve the total number of particles, i. e. the spectral modification is a general uncertainty ($\alpha \neq 1$, $g^{(\mathrm{a})}(E) \neq 1$). Therefore, the SOBP dose level is wrong by the same amount than the total particle number in the spectrum is wrong. However, the dose stays almost flat over the whole axial extent of the SOBP. Hence, as already suggested in the previous section, the total number of particles in a spectrum of 20 MeV width is the most important property of the uncertainty.

6.2.2 Statistical uncertainties

Figure 6.3 shows the influence of statistical uncertainties which change from shot to shot. The modified spectrum is modeled with a Gaussian distribution around the anticipated

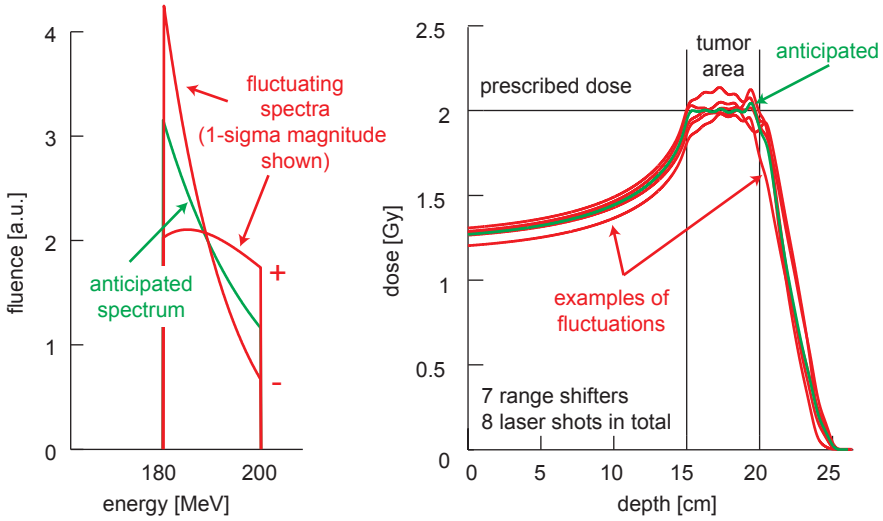

Figure 6.3: Statistical energy spectrum uncertainties (left) and their influence on SOBPs (right). See text for details.

one using the $\beta^{(a)}$ from the function $g^{(a)}(E)$ as the statistical variable. The 1-sigma magnitude of this distribution is shown for both directions in the figure. All modified spectra preserve the number of particles ($\alpha = 1$). The anticipated SOBP is pictured together with multiple examples of the random fluctuation. These fluctuating curves are relatively close to the anticipated depth dose curve because each curve consists of 8 laser shots and deviations already cancel out in successive shots. For a higher number of shots (i. e. less particles per shot) this effect becomes very important.

6.3 Three-dimensional considerations for the statistical number uncertainty

The next step is the analysis of uncertainties for the three-dimensional patient case. In the following only the *statistical number uncertainty* is regarded. Due to their nature *systematic* uncertainties cannot be handled mathematically; the restriction to the *number* uncertainty can be explained by the fact that the one-dimensional considerations showed that the influence of this uncertainty is the most important one[2].

[2] Additionally, the analysis of the distribution uncertainty for the three-dimensional case is much harder.

6.3.1 Error propagation

The *statistical* uncertainties in subsection 6.2.2 are illustrated by *throwing the dice*. However, a correct mathematical treatment of the statistical number uncertainty is possible by applying the method of *error propagation*. In the following, this uncertainty is analyzed in the voxel based model of the influence matrix. It is expressed as a variation of the beam weights ω_j while keeping the influence matrix D_{ij} constant[3]. Each beam weight ω_j is seen as a sum of shots with unit weight $e_m = 1$ where each single shot of each beam setting is subject to the same fluctuation $\delta e_m = \epsilon$. Hence, the last shot whose particle number is reduced with the fluence selection system has to be treated separately[4].

$$\omega_j = \sum_{n=1}^{\lfloor \omega_j \rfloor} e_n + \overbrace{\underbrace{(\omega_j - \lfloor \omega_j \rfloor)}_{=:\ \gamma_j \in [0,1)} e_{\lfloor \omega_j \rfloor + 1}}^{\text{last shot}}$$
$$\text{with} \quad e_m = 1 \pm \delta e_m = 1 \pm \epsilon \quad \forall m = 1 \ldots \lfloor \omega_j \rfloor + 1$$

Therefore, it is:

$$\begin{aligned}(\delta\omega_j)^2 &= \sum_{m=1}^{\lfloor \omega_j \rfloor + 1} \left(\frac{\partial \omega_j}{\partial e_m} \right)^2 (\delta e_m)^2 \\ &= \underbrace{\left(1^2 + \cdots + 1^2\right)}_{= \lfloor \omega_j \rfloor} \epsilon^2 + \gamma_j^2 \epsilon^2 = \left(\lfloor \omega_j \rfloor + \gamma_j^2 \right) \epsilon^2\end{aligned}$$

For the further analysis, the derivative of the dose D_i in voxel i with respect to the weight ω_j is needed:

$$D_i = \sum_k D_{ik} \omega_k \quad \rightarrow \quad \frac{\partial D_i}{\partial \omega_j} = D_{ij}$$

Then, the fluctuations in D_i can be expressed as follows:

$$\begin{aligned}(\delta D_i)^2 &= \sum_j \left(\frac{\partial D_i}{\partial \omega_j} \right)^2 (\delta \omega_j)^2 = \sum_j D_{ij}^2 \, (\delta \omega_j)^2 \\ &= \epsilon^2 \cdot \sum_j D_{ij}^2 \left(\lfloor \omega_j \rfloor + \gamma_j^2 \right)\end{aligned}$$

[3] A description where the ω_j are constant and D_{ij} is varied should be equivalent.
[4] It is assumed that the fluence selection itself does not introduce an additional uncertainty.

Here, ϵ can be seen as the relative shot-to-shot variability. In the formalism of equation set 6.1 it is $\alpha = 1 \pm \epsilon$. The final expression for the statistical dose uncertainty in a voxel caused by fluctuations in the total number of particles is therefore given by equation 6.3:

$$\delta D_i = \epsilon \cdot \sqrt{\sum_j D_{ij}^2 \left(\lfloor \omega_j \rfloor + (\omega_j - \lfloor \omega_j \rfloor)^2 \right)} \tag{6.3}$$

So far the statistical number uncertainty has been described with a constant shot-to-shot variability ϵ that was independent from the beam setting j. However, the laser accelerator could provide beam delivery settings with different uncertainty levels. For example, in addition to the *normal* laser shots it could offer shots with *low efficiency but high stability*. When keeping the shot-to-shot variability constant for all shots of one beam setting but allowing different ϵ_j for different beam settings ($e_m = 1 \pm \delta e_m = 1 \pm \epsilon_j \quad \forall m = 1 \ldots \lfloor \omega_j \rfloor + 1$), the variance in beam weights becomes $(\delta\omega_j)^2 = \left(\lfloor \omega_j \rfloor + \gamma_j^2 \right) \epsilon_j^2$ and therefore the statistical number uncertainty of the dose reads (compare to equation 6.3):

$$\delta D_i = \sqrt{\sum_j D_{ij}^2 \left(\lfloor \omega_j \rfloor + (\omega_j - \lfloor \omega_j \rfloor)^2 \right) \epsilon_j^2}$$

This additional flexibility in the description of the statistical number uncertainty has *not* been implemented into LAP-CERR and is only analyzed indirectly at a later point in this thesis.

6.3.2 Worst case dose distribution

An established way of reducing uncertainties is the concept of worst case optimization. It has previously been used to minimize setup and range uncertainties for proton therapy [39]. The basic idea is to look at a (physically nonexistent) worst case dose distribution that assumes the worst possible case for each voxel. In the case of the statistical number uncertainty this can be interpreted such that for the tumor the anticipated dose is shifted by $-\delta D_i$ (see equation 6.3) and for the normal tissue it is shifted by $+\delta D_i$. Hence, the worst case dose distribution $D_i^{\mathrm{wc}}(\omega)$ that depends on the number of shots

that is necessary to deliver the dose, is given by equation 6.4:

$$D_i^{\mathrm{wc}}(\omega) = \underbrace{\sum_j D_{ij}\omega_j}_{=\,D_i(\omega)} \pm \underbrace{\epsilon \cdot \sqrt{\sum_j D_{ij}^2 \left(\lfloor \omega_j \rfloor + (\omega_j - \lfloor \omega_j \rfloor)^2 \right)}}_{=\,\delta D_i(\omega)} \tag{6.4}$$

$-$ for tumor tissue, i. e. assumed underdose

$+$ for normal tissue (including OARs), i. e. assumed overdose

Note that in this context the worst case dose is a statistical measure, i. e. in certain voxels the actual dose can even be less optimal than predicted by the worst case value. Worst case optimization requires the minimization of the following objective function $F(\omega)$ (compare to equation 4.5):

$$F(\omega) = \underbrace{\sum_i p_i \left(D_i(\omega) - D_i^0 \right)^2}_{=\,F_0(\omega)} + p_{\mathrm{wc}} \left(\sum_i p_i \left(D_i^{\mathrm{wc}}(\omega) - D_i^0 \right)^2 \right)$$

The weighting factor p_{wc} has to be chosen to find a balance between a good physical dose distribution and a good worst case dose distribution. If LAP-CERR had a more flexible optimization algorithm this objective function could be implemented easily into the algorithm (as step (1.d) in figure 5.14 on page 85). However, as mentioned earlier Mosek requires quadratic functions. Therefore, the following procedure has to be applied to solve this problem. First, the following relation is utilized: $\lfloor \omega_j \rfloor + (\omega_j - \lfloor \omega_j \rfloor)^2 \approx \omega_j$. Second, with N being the number of beam settings (length of the vector ω), $\delta D_i(\omega)$ can be written in the following way:

$$\delta D_i(\omega) \approx \epsilon \cdot \sqrt{\sum_k D_{ik}^2 \omega_k} = \sum_j \underbrace{\frac{\epsilon}{\omega_j N} \sqrt{\sum_k D_{ik}^2 \omega_k}}_{=:\,A_{ij}(\omega)} \omega_j = \sum_j A_{ij}(\omega)\omega_j$$

Since $A_{ij}(\omega)$ is a matrix with the same dimensions than D_{ij}, the worst case optimization could be implemented despite the limitations given by Mosek. However, $A_{ij}(\omega)$ depends on ω which requires an *update* of the matrix after a certain amount of iterations. In this case the convergence of the algorithm is not guaranteed. Additionally, numerical problems occurred and rendered this ansatz unfeasible[5].

Nevertheless, the worst case dose distribution itself (equation 6.4) can be used to

[5] $A_{ij}(\omega)$ is - as opposed to D_{ij} - not a sparse matrix.

visualize the impact of the statistical number uncertainty on a dose distribution delivered with laser accelerated particles. This is more practicable than throwing the dice for each applied shot. Note that, as mentioned before, the worst case dose distribution is not a physically existing one and is especially not continuous at the border between tumor and normal tissue.

6.3.3 Reduction of the uncertainty

Another more straight forward approach to reduce the statistical number uncertainty is to minimize its value itself. In this case the square root in equation 6.3 that caused so much trouble before turns out to be useful:

$$\begin{aligned} F(\omega) =& \underbrace{\sum_i p_i \left(D_i(\omega) - D_i^0\right)^2}_{= F_0(\omega)} + p_{\text{uc}} \left(\sum_{i \in R} (\delta D_i)^2 \right) \\ =& F_0(\omega) + p_{\text{uc}} \sum_{i \in R} \epsilon^2 \sum_j D_{ij}^2 \left(\lfloor \omega_j \rfloor + (\omega_j - \lfloor \omega_j \rfloor)^2 \right) \end{aligned}$$

Here, p_{uc} is the penalty factor for uncertainties and R is a risk zone (e. g. one could chose to only include target voxels into the uncertainty minimization term). As before, for numerical reasons $\lfloor \omega_j \rfloor + (\omega_j - \lfloor \omega_j \rfloor)^2 \approx \omega_j$. Therefore:

$$F(\omega) \approx F_0(\omega) + p_{\text{uc}}\ \epsilon^2 \sum_j \underbrace{\sum_{i \in R} D_{ij}^2}_{=:\ y_j} \omega_j = F_0(\omega) + p_{\text{uc}}\ \epsilon^2 \sum_j y_j \omega_j$$

Hence, the uncertainty minimization is an additional linear term in the objective function and can therefore be integrated into the optimization executed by Mosek (as step (1.c) in figure 5.14 on page 85).

6.3.4 Results

One shot-to-shot variability ϵ for all beam settings

The patient case formerly used to explain the results of axial clustering (DVH entitled *advanced, 20 widths* in figure 5.18 on page 89) is reused in order to illustrate the statistical number uncertainty with an assumed shot-to-shot variability of $\epsilon = 0.5$. Before coming to the results of the uncertainty minimization itself, figure 6.4 shows that the worst case dose distribution given by equation 6.4 is a good measure for the statistical number

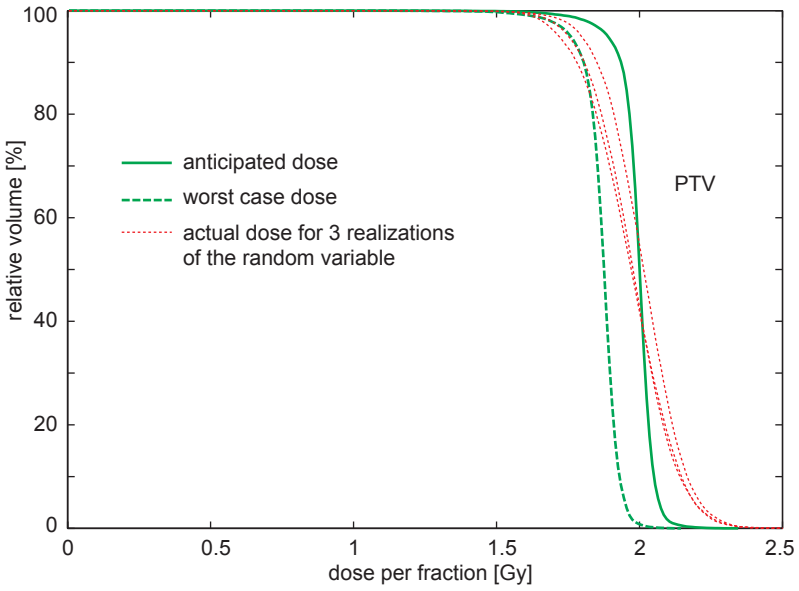

Figure 6.4: The worst case dose distribution for the statistical number uncertainty in comparison to 3 actual dose distributions obtained by evaluating the random variable. It can be seen that the worst case dose distribution is a good measure for possible actual dose distributions.

uncertainty in a three-dimensional patient case. The figure pictures the worst case dose distribution together with three actual dose distributions obtained by evaluating the random variable. Note that for a few voxels the actual dose in the PTV is smaller then the worst case dose. This happens because of the statistical nature of the worst case dose distribution.

Figure 6.5 illustrates the effect of the uncertainty minimization. The risk zone is chosen to be the PTV only, and the uncertainty weighting factor p_{uc} is set in a way that the uncertainty term in the objective function with the weights of a first intermediate optimization run without uncertainty minimization constitutes 0.5% of the objective function value of this intermediate run (comparable to the method to reduce the number of shots). It is clearly visible that the uncertainty in the PTV can be reduced while leaving the anticipated PTV dose unchanged. However, this comes at the cost of higher doses (anticipated and worst case) in both the PTV shell and the ipsilateral parotid gland. With a constant shot-to-shot variability for all beam settings, the only way to reduce the uncertainty is to use a higher shot number. This can be seen in this patient case as well: With the uncertainty minimization activated, the number of required shots increases from 5538 (see subsection 5.3.2 about the axial clustering results above) to 9202.

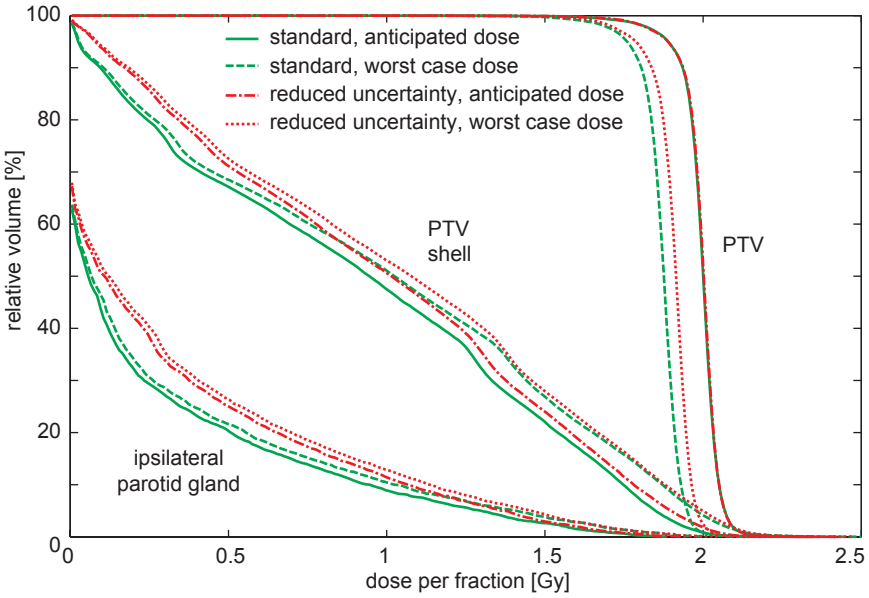

Figure 6.5: The effect of the statistical number uncertainty minimization in a three-dimensional patient plan. While the uncertainty in the PTV can be reduced without changing the anticipated dose, all other tissues show both higher anticipated and higher worst case doses. See text for explanation.

Additionally, the amount of blocked energy in the energy selection system increases from 10 J (see above) to 19 J. In general, both the axial and the lateral efficiency are decreased (by using a higher number of less efficient beam settings instead of a smaller number of efficient ones) and possibly the plan quality is deteriorated by allowing more dose in the normal tissue (regarding the minimization of the uncertainty in the PTV, more dose is always better). It has to be mentioned that the uncertainty minimization works against every single aspect of efficiently using laser accelerated particles discussed so far. Unfortunately, changing the risk zone or the parameter p_{uc} does not change this behavior.

Different shot-to-shot variabilities ϵ_j for different beam settings

As mentioned earlier, the shot-to-shot variability is not necessarily the same for all beam settings. While this cannot be analyzed in LAP-CERR a trick can be applied: Instead of changing ϵ for certain j it is possible to artificially change the amount of particles per shot delivered by the laser-driven accelerator and thus certain columns of the influence matrix D_{ij}. Therefore, if for example the dose of certain beam settings is decreased, these settings will need a higher amount of shots per spot which will automatically

decreases the uncertainty[6].

A patient case was prepared that is again similar to the one used for demonstrating the axial clustering technique. There, for every used beam direction, two spectra with 10^8 particles per laser shot each have been offered to the algorithm. In the case analyzed here, each beam direction is used twice, once with the possibility to use the previously mentioned spectra and once with a copy of these spectra with 10^9 particles per shot. Thus, for all spectra the shot-to-shot-variability ϵ can be set to the same value[7]. When using no uncertainty minimization the resulting plan uses a combination of the spectra with 10^8 and 10^9 particles per shot. Since the optimization tries to minimize the number of shots, the spectrum with 10^9 particles per shot is used more frequently. In contrast, if the uncertainty minimization is activated the use of the spectra with 10^9 particles will diminish depending on the choice of p_{uc}. This illustrates the conflictive optimization goals regarding the increase of the efficiency and the minimization of the uncertainty. Additionally, it shows that the uncertainty minimization works as expected as soon as there are enough degrees of freedom to choose from.

6.4 Discussion

As mentioned before, the fluence per energy in one laser shot is a crucial parameter that can be subject to uncertainties. When using an energy selection system with a relatively small energy spread (up to 20 MeV) in the transmitted beam, the distribution of a fixed amount of particles over a certain window of transmitted energies is of minor importance compared to the total number of particles. Therefore, measurements of the energy spectrum might not be as important (compare to detector 1 in figure 3.5 on page 36) as measurements of the number of particles (compare to detector 2 in the same figure).

Systematic uncertainties have to be minimized by adequate *quality assurance* (QA) systems which are not part of this thesis. However, the statistical number uncertainty was analyzed for three-dimensional patient cases. Unfortunately, a worst case dose optimization could not be implemented due to limitations in the optimization algorithm. However, this kind of optimization would promise a better reduction of the uncertainty compared to the simple uncertainty minimization performed here, which tends to increase the normal tissue doses. Nevertheless, *every* algorithm will try to reduce the

[6] The disadvantage of this method is the loss of absolute dosimetry and therefore the possibility to analyze beam quantization effects.

[7] The resulting DVHs of this study are not presented since they do not provide any additional information. Instead, only the results concerning the uncertainty are stated.

uncertainties by increasing the number of shots. If the number uncertainty of a laser system is too high, the efficiency of the system cannot be increased since this increases the uncertainty even further. However, regarding the very high shot-to-shot variability of $\epsilon = 0.5$ used for the patient case, the efficiency of the system is of minor concern. In this case, it is imaginable to even deliberately decrease the efficiency of the particle beam (e. g. by blocking more particles than necessary in the fluence selection system) to allow a higher amount of shots per spot (assuming that the repetition rate is high enough).

It has to be kept in mind that future studies have to unveil the most important uncertainties for laser accelerated particles. They are determined by both the laser acceleration itself (see section 2.1) and the dose delivery system attached to it (see section 3.3). At the moment, whereas it is already hard to estimate the anticipated properties of these machines, it is even harder to estimate the uncertainties in these values.

7 Summary and outlook

The aim of this thesis is to analyze the potential of laser-plasma accelerated particles like protons or carbon ions for their usage in radiation therapy. The underlying idea is that the potentially smaller and more cost-efficient laser-plasma accelerators could one day supersede conventional accelerators like cyclotrons or synchrotrons, which could result in a more widespread application of particle therapy for the treatment of cancer.

For this purpose a short introduction into laser-plasma acceleration is given (section 2.1). Based on the physics behind this technique the differences of these particles compared to conventionally accelerated ones are explained in detail and solutions to cope with these differences are presented (section 2.2): The particle beam with a generally broad energy spectrum, which causes an inferior distribution in the depth dose curve, can be handled with a magnetic energy selection system to restore a monoenergetic beam with its well-known Bragg peak; the possibly high particle fluence per shot can be handled with a scattering based fluence selection system to remove the surplus particles; and the mixture of particle types within the accelerated beam can be handled with an additional electrical particle selection system to limit the beam to one ion type only. However, these methods are rather inefficient regarding treatment time and a minimization of secondary radiation. This is because the *unwanted* particles are simply blocked out in the three selection systems. Additionally, a high enough repetition rate of the accelerator, which is necessary for spot-scanning, and a proper incorporation of possible uncertainties are not guaranteed (section 2.3). These problems occur in part because the 'classical' ideas for using laser-accelerated particles in radiation therapy try to restore the properties of conventionally accelerated particles to allow an unaltered treatment planning process.

Therefore, the principle mechanisms of 'classical' dose delivery with particle beams like spot-scanning are revised regarding the special case of laser-accelerated particles (section 3.1) in order to find alternatives that are more suitable (section 3.2). Discarding a full spot-scanning approach in favor of a flexible dose clustering technique can resolve a lot of the foremost mentioned restrictions without sacrificing the superior dose distribution achievable by IMPT. This is due to the vast amount of idle degrees of freedom in

particle therapy that can be utilized to make the use of laser accelerated particles more efficient. Instead of irradiating each tumor spot independently, certain tumor areas can be grouped into clusters whose members are irradiated simultaneously: For axially adjacent tumor spots, the wide energy spectrum of laser accelerated particles is of advantage since it allows the irradiation of different tumor depths with one particle beam (axial clustering). This increases the efficiency in the energy selection system. Additionally, a possibly high number of particles per spot can be used when distributing the particles over a greater lateral extent with the help of a scattering foil and a subsequent collimator (lateral clustering). This increases the efficiency in the fluence selection system. The hardware that is necessary to perform the treatment is then summarized by the discussion of the possible design of a treatment head (section 3.3). These theoretical dose delivery concepts are completed by new strategies to steer the particle beam onto the patient (section 3.4). One of the potential advantages of laser-accelerated particles is the usage of a laser-gantry instead of a particle-gantry meaning that not the particle beam itself but the laser beam is steered around the patient. Since the acceleration process is very compact, the laser beam can be guarded around the patient with mirrors and the particle beam can be created in close proximity to the patient allowing a much lighter gantry construction compared to conventional particle accelerators. This provides new flexibility in the usage of possible gantry movements (gantry-scanning) which can solve additional limitations of laser-accelerated particles like for example the limited magnetic scanning range of beams with a wider energy spectrum. At this point a medium-term and a long-term outlook to future clinical applications is given (section 3.5).

To analyze the ideas presented so far in more detail, various computational considerations to simulate a treatment system for laser-accelerated particles are discussed. Monte-Carlo simulations with Geant4 (section 4.1) as well as planning simulations with an experimental treatment planning software, that was developed as an extension to the software tool CERR (section 4.2), are performed. This is completed by an in-depth explanation of the used dose calculation (section 4.3), dose optimization (section 4.4) and efficiency calculation (section 4.5) algorithms.

By application of the foremost mentioned methods it is then shown quantitatively how radiation therapy with laser-accelerated particles can now - instead of using only 'classical' methods (section 5.1) - be performed in an 'advanced' way that is more suitable to the specific properties of these new particle accelerators. Therefore, two different studies are carried out: The first one illustrates that an additional scattering material in the energy selection system can shape the energy spectrum of a beam in a way that the relative amount of particles per energy bin is the one needed for a homogeneous dose

distribution in the target (spread-out Bragg peak, SOBP) (section 5.2). This allows the generation of SOBPs with one laser shot only and increases the efficiency in the energy selection system since less particles have to be blocked compared to a system where monoenergetic beams are restored. The second study applies the clustering techniques and further modifications of the objective function of the dose optimization routine to demonstrate that treatments with an adapted beam delivery and planning process can produce high quality clinical treatment plans with a high(er) particle efficiency and low(er) repetition rates (section 5.3). For example, the usage of wider energy spectra (up to 20 MeV instead of 1 MeV only) for automatically selected tumor regions can increase the efficiency in the energy selection system by a factor of 14. In addition to this, the number of laser shots required to deliver the treatment is decreased by a factor of 12. These studies show that the proposed alteration of the beam delivery and treatment planning process reduces the requirements for future usage of laser-accelerated particles in radiation therapy (section 5.4).

Last but not least uncertainties associated with the properties of laser-accelerated particles are classified (section 6.1) and analyzed. The focus is put on fluctuations in the energy spectrum of the accelerated particles. In one-dimensional studies (section 6.2), it turns out that the uncertainty in the total number of particles passing the energy selection system is one of the key uncertainties. In contrast to this, the energy distribution within the window of transmitted energies is not the primary concern. Therefore, in further three-dimensional studies (section 6.3) the uncertainty in the total number of transmitted particles is analyzed in more detail with the help of a worst case dose distribution and additional modifications in the optimization algorithm. The results (section 6.4) imply, that for this kind of uncertainty a high number of shots per tumor spot is of advantage, hence, a high repetition rate is required. Unfortunately, this is in contrast to the results of other methods to adapt the treatment to laser-accelerated particles. However, this will only be necessary if the uncertainties in the total number of transmitted particles are very high.

One of the next steps for making use of laser-plasma accelerated particles in radiation therapy is the increase of the maximally achievable particle energy and the better characterization of the produced particle beams. Detailed information about the energy spectrum, the angular spectrum and the time structure is of great interest. On the one hand, this information can then be used to design a beam delivery system for a specific machine. Besides the requirements explained in this thesis, this system has to fulfill further purposes such as the shielding of secondary radiation. Additionally, it remains to be proven that the final machine can be produced in a more compact and cost-efficient

way than systems using conventional acceleration methods. On the other hand, the more detailed information about the particle beam can be fed into the experimental treatment planning tool developed within this thesis. This would allow to either set priorities for some of the developed methods or even rule out other methods. For example, if the number of particles per shot stays below a certain threshold, a fluence selection system will not be necessary, and hence the method of lateral clustering will not have to be applied.

Since the energy and stability of the particle beam cannot be increased in one sudden step, intermediate studies can explore the properties of laser-accelerated particles in cell and animal experiments, which - from the point of view of the beam requirements - are not as demanding as clinical studies. Additionally, these studies can also clarify possible biological differences of laser-accelerated particle radiation compared to other modalities.

In summary, this work presents methods and techniques that prepare the conventional particle treatment in radiation therapy for the advent of future laser-accelerated particle accelerators. The promise to use these accelerators for cancer therapy has been one of the main drivers for recent research in the field of laser-plasma acceleration. Therefore, it is necessary to analyze the technological and clinical consequences of this development. It is illustrated on the one hand which improvements in the accelerator technology are still necessary and on the other hand which changes to the conventional treatment delivery and planning process have to be made to fulfill the promise. The future will show if these machines can reach a status where they can be used for clinical application and hence contribute to a more widespread application of particle therapy.

Curriculum Vitae

Stefan Schell
born on: November 12th, 1981
born in: Traben-Trarbach, Germany

10/2008 - 10/2011	Klinikum rechts der Isar der Technischen Universität München, Germany; research fellow and PhD student in physics; *Doktorarbeit* in physics planned for 2011
08/2007 - 09/2008	Deutsches Krebsforschungszentrum, Heidelberg, Germany; research fellow and diploma student in physics; *Diplomarbeit* in physics in 2008 with grade *1.0* and title "The linear quadratic damage model in radiation therapy planning: effect based optimization and automatic fractionation scheme adjustment"
09/2005 - 07/2006	University of Oregon, Eugene, OR, USA; master student in physics; *Master of Science* in physics in 2006 with GPA *3.9*
08/2002 - 09/2008	Universität Heidelberg, Germany; diploma student in physics; *Diplom* in physics in 2008 with grade *sehr gut*; *Vordiplom* in physics in 2004 with grade *sehr gut*
07/1992 - 06/2001	Gymnasium Traben-Trarbach, Germany; high school pupil; *Allgemeine Hochschulreife* with grade *1.5*

List of Publications

Papers in journals

First author

- Schell S. and J.J. Wilkens: "Advanced treatment planning methods for efficient radiation therapy with laser accelerated proton and ion beams", Med Phys 37(10), 5330-5340, 2010.

- Schell S. and J.J. Wilkens: "Modifying proton fluence spectra to generate spread-out Bragg peaks with laser accelerated proton beams", Phys Med Biol 54(19), N459-N466, 2009.

- Schell S., J.J. Wilkens and U. Oelfke: "Radiobiological effect based treatment plan optimization with the linear quadratic model", Z Med Phys 20(3), 188-196, 2010.

Coauthor

- Falkinger M., S. Schell, J. Müller and J.J. Wilkens: "Prioritized optimization in intensity modulated proton therapy", Z Med Phys, in press, 2011.

- Kampfer S., S. Schell, M.N. Duma, J.J. Wilkens and P. Kneschaurek: "Measurements to predict the time of target replacement of a helical tomotherapy", J Appl Clin Med Phys, in press, 2011.

- Greubel C., W. Assmann, C. Burgdorf, G. Dollinger, G. Du, V. Hable, A. Hapfelmeier, R. Hertenberger, P. Kneschaurek, D. Michalski, M. Molls, S. Reinhardt, B. Röper, S. Schell, T.E. Schmid, C. Siebenwirth, T. Wenzl, O. Zlobinskaya and J.J. Wilkens: "Scanning irradiation device for mice in vivo with pulsed and continuous proton beams", Radiat Environ Biophys, in press, 2011.

Papers in books and conference abstracts

First author

- Schell S. and J.J. Wilkens: "Therapieplanung für effiziente Strahlentherapie mit laserbeschleunigten Protonen und Ionen", Strahlenther Onkol 187(Sondernr. 1), p. 61, 2011 (e-poster and oral presentation).

- Schell S. and J.J. Wilkens: "Energy spectrum uncertainties in radiation therapy with laser accelerated particles", Radiother Oncol 99(Suppl. 1), p. S162, 2011 (poster).

- Schell S. and J.J. Wilkens: "Therapieplanungsmethoden für effiziente Strahlentherapie mit laserbeschleunigten Protonen und Ionen", in: Hodapp N., J. Hennig, M. Mix (eds.): Medizinische Physik 2010 (Deutsche Gesellschaft für Medizinische Physik: Freiburg), ISBN 3-925218-88-2, p. 400-403, 2010 (oral presentation).

- Schell S. and J.J. Wilkens: "Efficient treatment planning and dose delivery methods for radiation therapy with laser accelerated proton beams", in: Abstracts of the 49th Meeting of the Particle Therapy Co-Operative Group (PTCOG), 17-22 May 2010, Gunma/Japan, P5-1, p. 149, 2010 (poster).

- Schell S. and J.J. Wilkens: "Modifying proton fluence spectra to generate spread-out Bragg peaks with laser accelerated proton beams", Abstracts of the 48th Meeting of the Particle Therapy Co-Operative Group (PTCOG), Heidelberg 2009 (German Medical Science GMS Publishing House: Düsseldorf), 2009 (poster).

- Schell S. and J.J. Wilkens: "Treatment planning methods for efficient dose delivery in radiation therapy using laser accelerated particle beams", in: O. Dössel and W. Schlegel (eds.): World Congress on Medical Physics and Biomedical Engineering, September 7-12, 2009, Munich, Germany (IFMBE Proceedings Vol. 25/XIII) (Springer: Berlin, Heidelberg, New York), p. 28-31, 2009 (oral presentation).

- Schell S., J.J. Wilkens and U. Oelfke: "Optimierung von Fraktionierungseffekten in der Bestrahlungsplanung", in: E-Verhandlungen 2009. Abstracts der Frühjahrstagung in München. Deutsche Physikalische Gesellschaft (DPG), ST 6.4, 2009 (oral presentation).

- Schell S., J.J. Wilkens and U. Oelfke: "Optimierung von Fraktionierungseffekten in der Bestrahlungsplanung", in: TagungsCD der 39. Jahrestagung (Deutsche Gesellschaft für Medizinische Physik: Oldenburg), 2008 (oral presentation).

Coauthor

- Michalski D., T.E. Schmid, O. Zlobinskaya, C. Siebenwirth, C. Greubel, V. Hable, C. Burgdorf, G. Du, L. Tonelli, T. Wenzl, S. Schell, S. Reinhardt, W. Assmann, B. Röper, G. Multhoff, M. Molls, R. Krücken, G. Dollinger and J.J. Wilkens: "Tumor growth delay experiment with a pulsed nanosecond proton microbeam", Strahlenther Onkol 187(Sondernr. 1), p. 62, 2011.

- Zlobinskaya O., T.E. Schmid, C. Siebenwirth, C. Greubel, V. Hable, C. Burgdorf, G. Du, L. Tonelli, D. Michalski, T. Wenzl, S. Schell, S. Reinhardt, W. Assmann, B. Röper, M. Molls, R. Krücken, G. Dollinger, J.J. Wilkens: "Tumor Growth Delay Experiment with a Pulsed Nanosecond Proton Microbeam", in: M. Baumann,

J. Dahm-Daphi, E. Dikomey, C. Petersen, H. Rodemann, D. Zips (eds.): Experimentelle Strahlentherapie und Klinische Strahlenbiologie, Vol. 20 (Dresden), ISSN 1432-864X, p. 69-72, 2011.

- Falkinger M., S. Schell, J. Müller and J.J. Wilkens: "Sequentielle Optimierung für die intensitätsmodulierte Protonentherapie", in: Hodapp N., J. Hennig, M. Mix (eds.): Medizinische Physik 2010 (Deutsche Gesellschaft für Medizinische Physik: Freiburg), ISBN 3-925218-88-2, p. 78-81, 2010.

- Greubel C., C. Siebenwirth, V. Hable, C. Burgdorf, G. Du, O. Zlobinskaya, T. Schmid, D. Michalski, T. Wenzl, S. Schell, S. Reinhardt, W. Assmann, J. Wilkens, B. Röper, M. Molls, R. Krücken, G. Dollinger: "Tumour Irradiation in Living Mice with a Pulsed Nanosecond Proton Microbeam", in: Abstracts of the 12th International Conference on Nuclear Microprobe Technology and Applications (July 26-30, 2010; Leipzig, Germany), p. 57, 2010.

- Zlobinskaya O., T.E. Schmid, D. Michalski, C. Greubel, V. Hable, C. Siebenwirth, S. Reinhardt, P. Kneschaurek, W. Assmann, C. Burgdorf, G. Du, T. Wenzl, S. Schell, J.J. Wilkens, B. Röper, M. Molls, G. Dollinger: "Scanning device for mice in vivo irradiation with pulsed and continuous proton beams", Strahlenther Onkol 186(Sondernr. 1), p. 52-53, 2010.

- Siebenwirth C., C. Greubel, V. Hable, C. Burgdorf, G. Du, O. Zlobinskaya, T. Schmid, D. Michalski, T. Wenzl, S. Schell, S. Reinhardt, W. Assmann, J. Wilkens, B. Röper, M. Molls, R. Krücken, G. Dollinger: "Tumor irradiation in living mice with a pulsed nanosecond microbeam", in: Abstracts of the 9th International Microbeam Workshop, 15-17 July 2010, Darmstadt/Germany, p. 63, 2010.

List of Figures

Bibliography

[1] Agostinelli, S., Allison, J., Amako, K., Apostolakis, J., Araujo, H., Arce, P., Asai, M., Axen, D., Banerjee, S., Barrand, G., et al. GEANT4 - a simulation toolkit. *Nuclear Instruments and Methods in Physics Research, Section A 506*, 3 (2003), 250–303.

[2] Baumhacker, H., Böswald, A., Haas, H., Fischer, M., Fölsner, W., Keller, G., Andiel, U., Dong, X., Dreher, M., Eidmann, K., Fill, E., Hegelich, M., Kaluza, M., Karsch, S., Pretzler, G., Tsakiris, G. D., and Witte, K. J. Advanced titanium sapphire laser ATLAS MPQ-Report 272. Tech. rep., Max-Planck-Institut für Quantenoptik, 2010.

[3] Bortfeld, T. An analytical approximation of the Bragg curve for therapeutic proton beams. *Medical Physics 24*, 12 (1997), 2024–33.

[4] Bortfeld, T., and Schlegel, W. An analytical approximation of depth-dose distributions for therapeutic proton beams. *Physics in Medicine and Biology 41*, 8 (1996), 1331–9.

[5] Bulanov, S. V., and Khoroshkov, V. S. Feasibility of using laser ion accelerators in proton therapy. *Plasma Physics Reports 28*, 5 (2002), 453–6.

[6] Caporaso, G. J., Mackie, T. R., Sampayan, S., Chen, Y. J., Blackfield, D., Harris, J., Hawkins, S., Holmes, C., Nelson, S., Paul, A., Poole, B., Rhodes, M., Sanders, D., Sullivan, J., Wang, L., Watson, J., Reckwerdt, P. J., Schmidt, R., Pearson, D., Flynn, R. W., Matthews, D., and Purdy, J. A compact linac for intensity modulated proton therapy based on a dielectric wall accelerator. *Physica Medica 24*, 2 (2008), 98–101.

[7] Chu, W. T., Ludewigt, B. A., and Renner, T. R. Instrumentation for treatment of cancer using proton and light-ion beams. *Review of Scientific Instruments 64* (1993), 2055–122.

[8] Cozzi, L., Fogliata, A., Lomax, A. J., and Bolsi, A. A treatment planning comparison of 3D conformal therapy, intensity modulated photon therapy and proton therapy for treatment of advanced head and neck tumours. *Radiotherapy and Oncology 61*, 3 (2001), 287–97.

[9] Daartz, J., Bangert, M., Bussière, M. R., Engelsman, M., and Kooy, H. M. Characterization of a mini-multileaf collimator in a proton beamline. *Medical Physics 36* (2009), 1886–94.

[10] Deasy, J. O., Blanco, A. I., and Clark, V. H. CERR: A computational environment for radiotherapy research. *Medical Physics 30* (2003), 979–85.

[11] Fourkal, E., Li, J. S., Ding, M., Tajima, T., and Ma, C. M. Particle selection for laser-accelerated proton therapy feasibility study. *Medical Physics 30* (2003), 1660–70.

[12] Fourkal, E., Li, J. S., Xiong, W., Nahum, A., and Ma, C. M. Intensity modulated radiation therapy using laser-accelerated protons: a Monte Carlo dosimetric study. *Physics in Medicine and Biology 48*, 24 (2003), 3977–4000.

[13] Gottschalk, B., Koehler, A. M., Schneider, R. J., Sisterson, J. M., and Wagner, M. S. Multiple Coulomb scattering of 160 MeV protons. *Nuclear Instruments and Methods in Physics Research, Section B 74* (1993), 467–90.

[14] Habs, D., Henig, A., Jung, D., Kiefer, D., Hörlein, R., Gross, M., Schreiber, J., Kh., L. V., M., H. B., Karsch, S., Yan, X. Q., Meyer-ter Vehn, J., and Tajima, T. Laser-driven particle acceleration utilizing nm-thin diamond foils: Improved ion acceleration for cancer therapy, improved electron acceleration and potentially ultra-brilliant x-ray beams for medical diagnostics. In *World Congress on Medical Physics and Biomedical Engineering, September 7 - 12, 2009, Munich, Germany* (2009), O. Dössel and W. C. Schlegel, Eds., vol. 25/II of *IFMBE Proceedings*, Springer, pp. 304–7.

[15] Hall, E. J., and Giaccia, A. J. *Radiobiology for the radiobiologist*, 6 ed. Lippincott Williams and Wilkins, 2006.

[16] Harres, K., Alber, I., Tauschwitz, A., Bagnoud, V., Daido, H., Günther, M., Nürnberg, F., Otten, A., Schollmeier, M., Schütrumpf, J., et al. Beam collimation and transport of quasineutral laser-accelerated protons by a solenoid field. *Physics of Plasmas 17*, 2 (2010), 023107.

[17] Henig, A. *Advanced Approaches to High Intensity Laser-Driven Ion Acceleration.* PhD thesis, Ludwig-Maximilians-Universität München, 2010.

[18] Henig, A., Steinke, S., Schnürer, M., Sokollik, T., Hörlein, R., Kiefer, D., Jung, D., Schreiber, J., Hegelich, B. M., Yan, X. Q., Meyer-ter Vehn, J., Tajima, T., Nickles, P. V., Sandner, W., and Habs, D. Radiation-pressure acceleration of ion beams driven by circularly polarized laser pulses. *Physical Review Letters 103*, 24 (2009), 245003.

[19] Highland, V. L. Some practical remarks on multiple scattering. *Nuclear Instruments and Methods 129*, 2 (1975), 497–9.

[20] Hogstrom, K. R., Mills, M. D., and Almond, P. R. Electron beam dose calculations. *Physics in Medicine and Biology 26*, 3 (1981), 445–59.

[21] Hong, L., Goitein, M., Bucciolini, M., Comiskey, R., Gottschalk, B., Rosenthal, S., Serago, C., and Urie, M. A pencil beam algorithm for proton dose calculations. *Physics in Medicine and Biology 41* (1996), 1305–30.

[22] Kamp, F. Comparison of the lateral dose fall-off for proton and ion beams in radiation therapy. Master's thesis, Technische Universität München, 2011.

[23] Kanai, T., Kanematsu, N., Minohara, S., Komori, M., Torikoshi, M., Asakura, H., Ikeda, N., Uno, T., and Takei, Y. Commissioning of a conformal irradiation system for heavy-ion radiotherapy using a layer-stacking method. *Medical Physics 33* (2006), 2989–97.

[24] Kanai, T., Kawachi, K., Kumamoto, Y., Ogawa, H., Yamada, T., Matsuzawa, H., and Inada, T. Spot scanning system for proton radiotherapy. *Medical Physics 7*, 4 (1980), 365–9.

[25] Kaufman, L., and Rousseeuw, P. J. *Finding groups in data: An introduction to cluster analysis (Wiley Series in Probability and Mathematical Statistics)*. Wiley, New York, 1990.

[26] Klimo, O., Psikal, J., and Limpouch, J. Monoenergetic ion beams from ultrathin foils irradiated by ultrahigh-contrast circularly polarized laser pulses. *Physical Review Special Topics - Accelerators and Beams 11* (2008), 031301.

[27] Kraft, G., Weber, U., Kraft, S., and Kraft, S. Energy filter device, 2009.

[28] Lian, J., and Xing, L. Incorporating model parameter uncertainty into inverse treatment planning. *Medical Physics 31*, 9 (2004), 2711–20.

[29] Linz, U., and Alonso, J. What will it take for laser driven proton accelerators to be applied to tumor therapy? *Physical Review Special Topics - Accelerators and Beams 10* (2007), 094801.

[30] Lomax, A. J. Intensity modulated proton therapy and its sensitivity to treatment uncertainties 1: the potential effects of calculational uncertainties. *Physics in Medicine and Biology 53*, 4 (2008), 1027–42.

[31] Ma, C. M., Veltchev, I., Fourkal, E., Li, J. S., Luo, W., Fan, J., Lin, T., and Pollack, A. Development of a laser-driven proton accelerator for cancer therapy. *Laser Physics 16*, 4 (2006), 639–46.

[32] Malka, V., Faure, J., Gauduel, Y. A., Lefebvre, E., Rousse, A., and Phuoc, K. T. Principles and applications of compact laser-plasma accelerators. *Nature Physics 4*, 6 (2008), 447–53.

[33] Malka, V., Fritzler, S., Lefebvre, E., d'Humières, E., Ferrand, R., Grillon, G., Albaret, C., Meyroneinc, S., Chambaret, J. P., Antonetti, A., and Hulin, D. Practicability of protontherapy using compact laser systems. *Medical Physics 31*, 6 (2004), 1587–92.

[34] Martin, M. Laser accelerated radiotherapy: is it on its way to the clinic? *Journal of the National Cancer Institute 101*, 7 (2009), 450–1.

[35] Newhauser, W. D., Giebeler, A., Langen, K. M., Mirkovic, D., and Mohan, R. Can megavoltage computed tomography reduce proton range uncertainties in treatment plans for patients with large metal implants? *Physics in Medicine and Biology 53* (2008), 2327–44.

[36] Nill, S. *Development and application of a multi-modality inverse treatment planning system*. PhD thesis, University of Heidelberg, 2001.

[37] Nill, S., Bortfeld, T., and Oelfke, U. Inverse planning of intensity modulated proton therapy. *Zeitschrift für Medizinische Physik 14*, 1 (2004), 35–40.

[38] Nishiuchi, M., Daito, I., Ikegami, M., Daido, H., Mori, M., Orimo, S., Ogura, K., Sagisaka, A., Yogo, A., Pirozhkov, A. S., Sugiyama, H., Kiriyama, H., Okada, H., Kanazawa, S., Kondo, S., Shimomura, T., Tanoue, M., Nakai, Y., Sasao, H., Wakai, D., Sakaki, H., Bolton, P., Choi, I. W., Sung, J. H., Lee, J., Oishi, Y., Fujii, T., Nemoto, K., Souda, H., Noda, A., Iseki, Y., and Yoshiyuki, T. Focusing and spectral enhancement of a repetition-rated, laser-driven, divergent multi-MeV proton beam using permanent quadrupole magnets. *Applied Physics Letters 94*, 6 (2009), 061107.

[39] Pflugfelder, D., Wilkens, J. J., and Oelfke, U. Worst case optimization: a method to account for uncertainties in the optimization of intensity modulated proton therapy. *Physics in Medicine and Biology 53* (2008), 1689–700.

[40] Robson, L., Simpson, P. T., Clarke, R. J., Ledingham, K. W. D., Lindau, F., Lundh, O., McCanny, T., Mora, P., Neely, D., Wahlström, C. G., and McKenna, P. Scaling of proton acceleration driven by petawatt-laser–plasma interactions. *Nature Physics 3*, 1 (2007), 58–62.

[41] Russell, K. J., Caplan, R. J., Laramore, G. E., Burnison, C. M., Maor, M. H., Taylor, M. E., Zink, S., Davis, L. W., and Griffin, T. W. Photon versus fast neutron external beam radiotherapy in the treatment of locally advanced prostate cancer: results of a randomized prospective trial. *International Journal of Radiation Oncology, Biology, Physics 28*, 1 (1994), 47–54.

[42] Safai, S., Bortfeld, T., and Engelsman, M. Comparison between the lateral penumbra of a collimated double-scattered beam and uncollimated scanning beam in proton radiotherapy. *Physics in Medicine and Biology 53* (2008), 1729–50.

[43] Sakaki, H., Nishiuchi, M., Hori, T., Bolton, P. R., Tampo, M., Yogo, A., Kondo, K., Kawanishi, S., Iwase, H., and Niita, K. Simulation of laser-accelerated proton focusing and diagnosis with a permanent magnet quadrupole triplet. *Plasma and Fusion Research 5* (2010), 9.

[44] Schell, S., and Wilkens, J. J. Modifying proton fluence spectra to generate spread-out Bragg peaks with laser accelerated proton beams. *Physics in Medicine and Biology 54*, 19 (2009), N459–66.

[45] Schell, S., and Wilkens, J. J. Advanced treatment planning methods for efficient radiation therapy with laser accelerated proton and ion beams. *Medical Physics 37*, 10 (2010), 5330–40.

[46] Schmid, T. E., Dollinger, G., Hable, V., Greubel, C., Zlobinskaya, O., Michalski, D., Molls, M., and Röper, B. Relative biological effectiveness of pulsed and continuous 20 MeV protons for micronucleus induction in 3D human reconstructed skin tissue. *Radiotherapy and Oncology 95*, 1 (2010), 66–72.

[47] Schollmeier, M., Becker, S., Geissel, M., Flippo, K. A., Blažević, A., Gaillard, S. A., Gautier, D. C., Grüner, F., Harres, K., Kimmel, M., Nürnberg, F., Rambo, P., Schramm, U., Schreiber, J., Schütrumpf, J., Schwarz, J., Tahir, N. A., Atherton, B., Habs, D., Hegelich, B. M., and Roth, M. Controlled transport and focusing of laser-accelerated protons with miniature magnetic devices. *Physical Review Letters 101*, 5 (2008), 55004.

[48] Schulz-Ertner, D., and Tsujii, H. Particle radiation therapy using proton and heavier ion beams. *Journal of Clinical Oncology 25*, 8 (2007), 953–64.

[49] Shepard, D. M., Earl, M. A., Yu, C. X., and Xiao, Y. *Intensity-modulated radiation therapy: the state of the art*. Medical Physics Publishing, Madison, 2003, ch. Aperture-based inverse planning, pp. 115–37.

[50] Snavely, R. A., Key, M. H., Hatchett, S. P., Cowan, T. E., Roth, M., Phillips, T. W., Stoyer, M. A., Henry, E. A., Sangster, T. C., Singh, M. S., et al. Intense high-energy proton beams from petawatt-laser irradiation of solids. *Physical Review Letters 85*, 14 (2000), 2945–8.

[51] Steel, G. G. *Basic Clinical Radiobiology*, 3 ed. Hodder Arnold, 2002.

[52] Strickland, D., and Mourou, G. Compression of amplified chirped optical pulses. *Optics Communications 56*, 3 (1985), 219–21.

[53] Sutherland, K., Miyajima, S., Date, H., Shirato, H., Ishikawa, M., Murakami, M., Yamagiwa, M., Bolton, P., and Tajima, T. A parameter study of pencil beam proton dose distributions for the treatment of ocular melanoma utilizing spot scanning. *Radiological Physics and Technology 3* (2010), 16–22.

[54] Szymanowski, H., and Oelfke, U. Two-dimensional pencil beam scaling: an improved proton dose algorithm for heterogeneous media. *Physics in Medicine and Biology 47*, 18 (2002), 3313–30.

[55] Tajima, T., Habs, D., and Yan, X. Laser acceleration of ions for radiation therapy. *Reviews of Accelerator Science and Technology 2*, 1 (2009), 201–28.

[56] Unkelbach, J., Chan, T. C. Y., and Bortfeld, T. Accounting for range uncertainties in the optimization of intensity modulated proton therapy. *Physics in Medicine and Biology 52*, 10 (2007), 2755.

[57] Weber, U., Becher, W., and Kraft, G. Depth scanning for a conformal ion beam treatment of deep seated tumours. *Physics in Medicine and Biology 45*, 12 (2000), 3627–41.

[58] Weichsel, J., Fuchs, T., Lefebvre, E., d'Humières, E., and Oelfke, U. Spectral features of laser-accelerated protons for radiotherapy applications. *Physics in Medicine and Biology 53* (2008), 4383–97.

[59] Wilkens, J. J., Alaly, J. R., Zakarian, K., Thorstad, W. L., and Deasy, J. O. IMRT treatment planning based on prioritizing prescription goals. *Physics in Medicine and Biology 52*, 6 (2007), 1675–92.

[60] Wilkens, J. J., and Oelfke, U. Direct comparison of biologically optimized spread-out bragg peaks for protons and carbon ions. *International Journal of Radiation Oncology, Biology, Physics 70*, 1 (2008), 262–6.

[61] Zeil, K., Kraft, S. D., Bock, S., Bussmann, M., Cowan, T. E., Kluge, T., Metzkes, J., Richter, T., Sauerbrey, R., and Schramm, U. The scaling of proton energies in ultrashort pulse laser plasma acceleration. *New Journal of Physics 12* (2010), 045015.

[62] Zenklusen, S. M., Pedroni, E., and Meer, D. A study on repainting strategies for treating moderately moving targets with proton pencil beam scanning at the new Gantry 2 at PSI. *Physics in Medicine and Biology 55* (2010), 5103–21.

Acknowledgments

I would like to take the chance to express my gratitude to all people that made this work possible. First of all, my special thanks are directed towards Prof. Dr. Jan J. Wilkens for being my supervisor and first referee. He was available for me whenever necessary and shaped this work more than anybody else. I had the great opportunity to carry out my research in his newly founded working group (called *Advanced Technologies in Radiation Therapy*, ATRT) that is part of the *Department of Radiation Oncology* of the *Klinikum rechts der Isar der Technischen Universität München*. It was a pleasure to work with you! I am also very grateful to Prof. Dr. Franz Pfeiffer for being the second referee.

Furthermore, I appreciate the support of the *Cluster of Excellence* called *Munich-Centre for Advanced Photonics* (MAP) run by the *German Research Foundation* (DFG). This grant provided the money for my employment and all further financial expenses. Furthermore, it offered the opportunity to collaborate with many other researchers in order to solve a few little but important problems necessary to achieve a great common goal.

I am also grateful for the collaboration with the people from the biology group of Dr. Thomas E. Schmid in the *Department of Radiation Oncology* which allowed me to participate in pre-clinical studies. Additionally, I would like to thank the clinical staff from the *Department of Radiation Oncology*, especially its head Prof. Dr. Michael Molls and the people of the medical physics group lead by Prof. Dr. Peter Kneschaurek. Being part of this department allowed me an uncomplicated but deep insight into the clinical workflow which helped to put my academic research into a realistic context. Furthermore, I appreciate the permission of Daniel Pflugfelder, that I know from my time at the German Cancer Research Center (DKFZ), to use his Matlab routine to calculate depth dose curves for protons.

Next, the group members of ATRT have to be mentioned for providing a cooperative, helpful and friendly environment that contributed to the fact that going to work was something to look forward to. Discussing problems and their possible solutions with colleagues was always the most exciting part of my work time. Especially, many thanks to Florian Kamp for supplying the Monte Carlo data for the dose calculation based on the tabulated particle dose data. And last but not least, I would like to thank my parents Karin and Hans-Otto, my grandparents, my girlfriend Nikki and all other close friends for their continuous support and inspiration.